IDŐJÁRÁS

QUARTERLY JOURNAL
OF THE HUNGARIAN METEOROLOGICAL SERVICE

Special Issue: Atmospheric Physics and chemistry in modern meteorology
Guest Editors: **István Geresdi**

CONTENTS

****

http://www.met.hu/Journal-Idojaras.php

VOL. 117* NO. 4 * OCTOBER – DECEMBER 2013

IDŐJÁRÁS

Quarterly Journal of the Hungarian Meteorological Service

Editorial Office: Kitaibel P.u. 1, H-1024 Budapest, Hungary
P.O. Box 38, H-1525 Budapest, Hungary
E-mail: journal.idojaras@met.hu
Fax: (36-1) 346-4669

Indexed and abstracted in Science Citation Index Expanded™ and Journal Citation Reports/Science Edition
Covered in the abstract and citation database SCOPUS®

Subscription by mail:
IDŐJÁRÁS, P.O. Box 38, H-1525 Budapest, Hungary
E-mail: journal.idojaras@met.hu

Editorial

Special Issue: Physics and chemistry in modern meteorology

The theme of the 38th Meteorological Scientific Days was the atmospheric physics and atmospheric chemistry. They are relatively new research fields of the meteorology. The first research about the cloud physics was initiated by weather modification programs in the late fifties and early sixties. The era of modern atmospheric chemistry began also in the fifties of last century, and research activity in this field became important as air pollution turned into an inevitable problem in the seventies. The importance of atmospheric physics and chemistry and their direct and indirect effects on both the short and long term atmospheric processes became obvious at about the middle of the last century. Due to the small size scale of physical and chemical processes, the laboratory observations gave a good opportunity to get the first results in the early sixties. The fast improvement of computer technology has allowed us both to apply the numerical simulation as a new research tool and to take into consideration the wide scale of physical and chemical processes in the weather forecast models and in the climate research as well. Since the interaction between the small scale physical and chemical processes and the large scale dynamics are rather strong, taking observation out of the laboratories became rather urgent by the eighties. Direct observations by aircrafts and application of satellites and radars have got essential role in the research and in the day-to-day operational works, as well.

The intention of the organizing committee was to get a comprehensive presentation of research activities and applications accomplished and developed by different research groups in Hungary. Eighteen oral presentations showed our knowledge in the fields of aerosol chemistry, transport of pollution in the atmosphere, radiation, and furthermore atmospheric electricity and cloud physics. The oral presentations were delivered by researchers and PhD students from Eötvös Loránd Univeristy, Hungarian Meteorological Service, University of Pannonia, and University of Pécs.

Four papers are presented in this special issue about different topics of the conference. In two papers the authors publish their result about the application of numerical models for investigation of the long-range transport of air pollution. In one paper the results about the state-of-the-art numerical simulation of the effect of clouds on the long-wave radiation are presented. One paper gives a detailed analysis about the solar radiation measurement carried out at the Hungarian Meteorological Service.

István Geresdi
Guest Editor

IDŐJÁRÁS

Quarterly Journal of the Hungarian Meteorological Service
Vol. 117, No. 4, October–December, 2013, pp. 359–375

Predictability analysis of the $PM_{2.5}$ and PM_{10} concentration in Budapest

Zita Ferenczi

Division for Analysis of Atmospheric Environment,
Hungarian Meteorological Service,
H-1675 Budapest, P.O.Box 39.
ferenczi.z@met.hu

(Manuscript received in final form July 29, 2013)

Abstract—The harmful effect of air pollution on human health have raised a series of concerns in recent years and imposed needs for accurate descriptions of air pollution levels in urban areas. This implies that tools supporting national pollution control and planning need to be developed including public web sites or other media, where citizens exposed to the air pollutants can catch urban background concentration data, predicted concentrations, or alerts. In recent years, PM_{10} episodes caused the most critical air quality problems in Budapest. Before the development of air quality forecasting systems, which help to predict the high PM_{10} concentration episodes, the main determinants have to be identified. In this work, the effect of long-range transport and meteorological conditions on PM_{10} concentration in Budapest was analyzed in detail, as well as the results of an existing air quality forecasting systems were evaluated in case of PM_{10}.

Key-words: air quality forecast, monitoring network, urban environment, emissions, meteorological parameters

1. Introduction

Climate, weather, and air quality have harmful effects on human health and environment. For centuries, people have selected their home where they could experience the most favorable environmental conditions. The Industrial Revolution brought great changes in energy usage and technological development. People moved in the cities in the hope of a better life, where the air was contaminated with different pollutants, depending on the current level of development of technology. The first big problem was the sulphur dioxide pollution, which was caused by the burning of coal. A few hundred years later, the widespread use of cars resulted in the increase of nitrogen oxides and tropospheric ozone concentrations in the

atmosphere. Nowadays, the high level of airborne particles concentration is considered seriously *(WHO,* 2011), especially in the winter season in Hungary.

Over the past few hundred years, we had to face also the changes in climate in parallel with the changes in air quality. The observed changes in climate, weather, and air quality continuously interact with each other: the pollutants are changing the climate, thus changing the weather, but also the climate impacts on air quality (*Bernard et al.,* 2001). The increasing number of extreme weather situations can occur as a result of climate change, which could create favorable conditions for rising of PM pollutant concentrations. In recent years, the PM_{10} episodes, which in many cases are associated with extreme weather situations, caused the most critical air quality problems in Budapest. The first step before developing a successful air quality forecast system is a detailed analysis of the meteorological background of the PM_{10} high-level situations (*Demuzere et al.,* 2009). Our investigation will focus on those episodes, which are caused by this pollutant, and on the long-range transport of the aerosol particles, which have also essential role in the formation of PM situation in Budapest.

The sum of all particles suspended in the atmosphere is referred to as PM (particulate matter). The particulates are classified according to their size and their capacity of penetrating the respiratory tract, causing harmful effects on people. The source of the particulate matter can be anthropogenic or natural. In urban environment, the most important causes of high PM_{10} concentration are traffic emissions, and in particular the use of diesel engines and motorcycles (*Sillanpää et al.,* 2006). Notable proportion is due to old tires and car brakes. During winter, emissions from domestic heating are added to the PM_{10} in larger amounts due to materials such as coal and wood.

Before developing an air quality forecasting system, which helps to predict the high PM_{10} concentration episodes, the main determinants (emission, meteorological conditions, and long-range transport) have to be identified. In this work, the effect of long-range transport and meteorological conditions on particulate matter in Budapest and Hungary was analyzed in detail.

Finally, the first results of the validation of the air quality prediction system of the Hungarian Meteorological Service are presented. In the evaluation work, the PM_{10} data detected by the air quality monitoring network of Budapest, as well as the forecasted air pollutant concentration values of the air quality prediction model system are used.

2. Analysis of the most important effects on PM concentration

Air quality of Budapest is determined by domestic and traffic emissions combined with the meteorological conditions. The effect of the long-range transport could also be essential. In this paragraph, the effect of emission, long-range transport, and meteorological conditions will be analyzed in detail.

2.1. Emission

The emission of PM_{10}, which has essential effect on the air quality of Budapest is determined by the industrial, traffic, and domestic heating activity in the area of Budapest. While the yearly variability of the industrial and traffic emissions are not significant, the domestic emissions increase in the winter season. All the mentioned emissions have weekly, daily and, especially for the traffic hourly variabilities. The different time variabilities of these emission sectors are reflected in the daily and yearly variability of concentration values of the PM_{10}.

2.2. Effect of the long-range transport on PM concentration

Effect of the long-range transport on the PM_{10} concentration was determined by the EMEP chemical transport model (*Simpson et al.,* 2012). With this examination only the yearly average of this effect could be analyzed. Sometimes the impact of the long-range transport can be negligible and sometimes it can be responsible for the episode situation. In this paragraph the effect of long-range transport on the PM_{10} and $PM_{2.5}$ in Budapest and Hungary will be analyzed in detail. The results will show how important this effect is and how we will able to put this information into an air quality forecasting system.

2.2.1. Short description of the EMEP model

Many types of air pollutants have been observed to travel far from their sources causing air quality problems (*EMEP Status Report,* 2012). Therefore, it is very important to begin the development of chemical transport models with investigating the long-range transport of the air pollutants. A representative of these types of models is the EMEP Eulerian long-range transport model (*Simpson et al.,* 2012). The model is an important tool to analyze both acidification and photo-oxidant activities in the air. The current version of the model working on a polar-stereographic projection, true at 60 N, has commonly been used, with grid-size of 50 km×50 km at 60 N. The standard domain has changed somewhat over the years, and was enlarged towards Eurasia in 2007. The model currently uses 20 vertical levels from the surface to the top of the model domain (currently: 100 hPa, 15 km). The 15 km high air column is divided into 20 levels in a form that the lower layer (3 km), which is relevant in the mixture of air pollutants, includes 10 levels, allowing the detailed examination of this air layer. The EMEP model uses a chemical pre-processor to convert lists of input chemical species and reactions to differential equations in Fortran code. The default chemical scheme, which is used in the open source version of the EMEP model, is the

EmChem09. This chemical scheme describes 137 reactions and 26 photochemical reactions between 72 chemical species. The model calculates the dry and wet deposition of the chemistry substances. The dry deposition flux is determined by using the deposition velocity, while the wet deposition processes include both in-cloud and sub-cloud scavenging of gases and particles.

The standard emissions input required by EMEP model consists of gridded annual national emissions of sulphur dioxide (SO_2), nitrogen oxides (NO_x =NO+NO_2), ammonia (NH_3), non-methane volatile organic compounds (NMVOC), carbon monoxide (CO), and particulates ($PM_{2.5}$, and PM_c, the latter being the coarse aerosol fraction, PM_{10}-$PM_{2.5}$). The particulate matter categories can be further divided into elemental carbon, organic matter, and other compounds as required. Emissions can be from anthropogenic sources (burning of fossil and biomass based fuels, solvent release, etc.), or from natural sources such as foliar VOC emissions or volcanoes.

The EMEP model has been adapted to run with meteorological fields calculated by a number of numerical weather prediction models, like the ECMWF IFS. In 2013, the data of the ECMWF IFS are available for forecasts with $0.125° \times 0.125°$ horizontal grid length and 137 vertical levels, and this model became the default meteorological driver.

2.2.2. Calculation of the long-range transport of PM_{10} concentration

For determining the long-range transport of the PM (particulate matter), the effect of the national emission from all countries in the EMEP model calculation area and the natural resources in the region were taken into account (*Gauss et al.,* 2012). The most important natural sources are the sea and the volcano, which have effect on the PM air quality conditions.

Our study was carried out for five years (2006–2010) in order to filter the variability of the weather as much as possible. Since the emission values show considerable variability from year to year (not only in case of Hungary), it is difficult to separate the effects of the weather from the effect of the emissions in the results.

First the proportion of the effect of the long-range transport was determined on the PM_{10} concentration in Hungary for five years (2006–2010). The results are summarized in *Table 1*.

On the basis of model calculations it was found that in annual average the transboundary sources are responsible for the 80% of the PM_{10} pollution formation in Hungary. According to *Table 1*, it can be said that in the last 5 years in Hungary, the PM_{10} emissions are significantly changed, and it could cause the variability in the quantity of the long-range transport.

Table 1. Fraction of transboundary contributions to PM_{10} concentrations in Hungary (unit: %) and the PM_{10} emission from Hungary (unit: Gg)

Years	Fraction of transboundary contributions (%)	Emission from Hungary (Gg)
2006	79	48
2007	83	36
2008	80	38
2009	79	48
2010	79	46

During the studied five years, trend in the change of the impact of the long-range transport could not be observed, the difference between the years can be mainly explained by changes in the PM_{10} emission of Hungary. In the years when the emission of Hungary was decreased significantly, the proportion of the long-range transport increased slightly. *Fig. 1* shows the spatial variability of the impact of long-range transport in Hungary between the years 2006 and 2010.

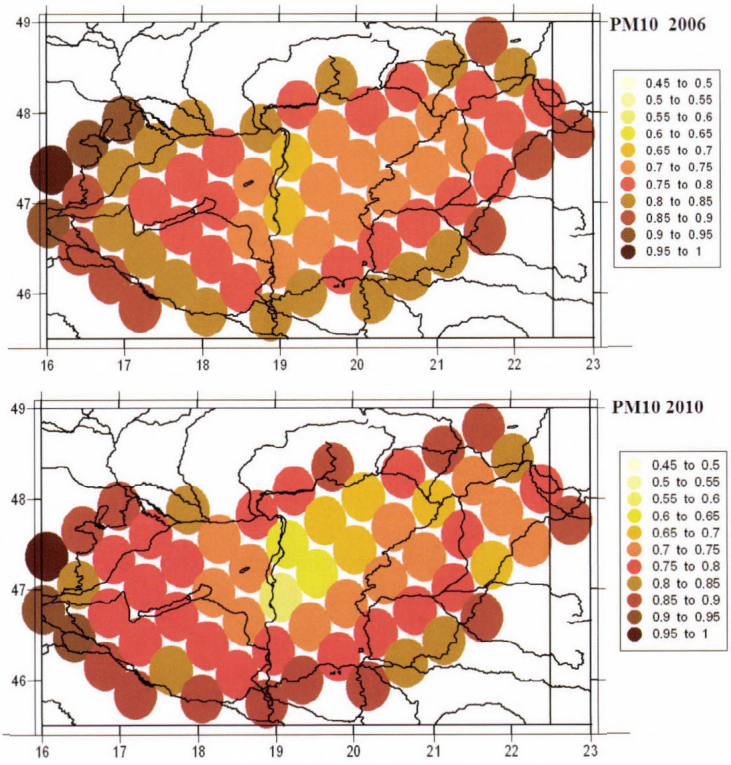

Fig. 1. Fraction of transboundary contributions to PM_{10} concentrations in Hungary in the years of 2006 and 2010 (unit: %).

In the second part of this study, the proportion of the long-range transport was determined on the PM_{10} pollution formation in the air quality zones of Hungary (*Table 2*). The definitions of the zones are:

1. Budapest and its surroundings
2. Győr - Mosonmagyaróvár
3. Komárom – Tatabánya - Esztergom
4. Székesfehérvár - Veszprém
5. Dunaújváros and its surroundings
6. Environs of Pécs
7. Sajó Valley
8. Debrecen and its surroundings

Table 2. Fraction of transboundary contributions to PM_{10} concentrations in the zones of Hungary in different years (unit:%)

Years	Zone 1	Zone 2	Zone 3	Zone 4	Zone 5	Zone 6	Zone 7	Zone 8
2006	69%	80%	78%	76%	68%	79%	72%	75%
2007	71%	86%	82%	80%	68%	84%	75%	77%
2008	68%	80%	76%	75%	65%	80%	71%	76%
2009	63%	76%	74%	73%	62%	80%	69%	77%
2010	65%	77%	74%	75%	58%	80%	67%	73%

According to *Table 2*, it can be said that the effect of the long-range transport on the PM_{10} concentration is the lowest in zone 1 (Budapest and its surroundings) and 5 (Dunaújváros and its surroundings), and the highest in zone 2 (Győr - Mosonmagyaróvár) and 6 (Environs of Pécs). Considering the country's size, this difference is mainly due to the significant spatial variability of the PM_{10} emission in Hungary. The largest industrial areas of Hungary located in zone 1 and zone 5 includes the area of our capital, where the combined effect of traffic and industries can cause high level PM_{10} emission.

2.2.3. Calculation of the long-range transport of $PM_{2.5}$ concentration

Further we determined the main contributor countries, which have significant effect on the $PM_{2.5}$ pollution formation in Hungary. *Table 3* summarizes the time variation of the national $PM_{2.5}$ emission of Hungary between 2006 and 2010.

Table 3. $PM_{2.5}$ emission from Hungary (unit: Gg).

Years	$PM_{2.5}$ emission from Hungary (Gg)
2006	29
2007	21
2008	23
2009	28
2010	32

Before preparing pie diagrams, the examined countries were placed into an order of magnitude based on how large the proportion of their contribution is to the $PM_{2.5}$ pollution of Hungary. The pie diagrams (*Fig. 2.*) show the proportion of the effect of Hungary and the 8 main contributor countries on the $PM_{2.5}$ concentration in the years of 2006 and 2010.

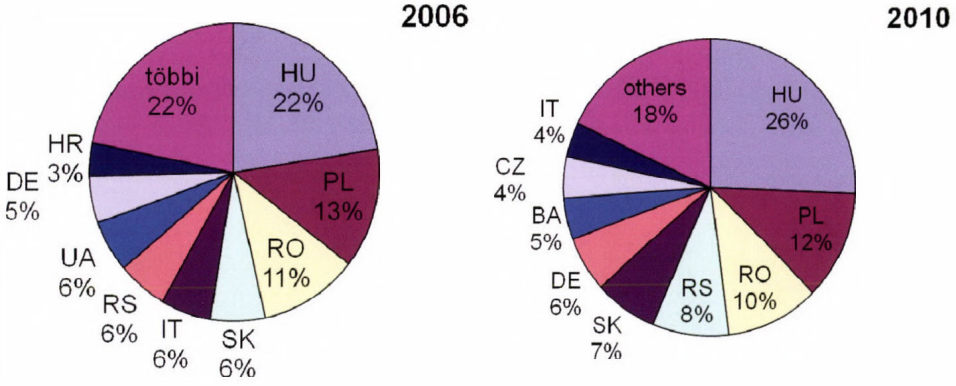

Fig. 2. Main contributors to concentrations of $PM_{2.5}$ in Hungary in the years of 2006 and 2010 (unit:%).

According to the pie charts, our homeland contributes to the $PM_{2.5}$ contamination in Hungary with 20–25%. It can be declared in general, that among the neighboring countries, the effect of Poland and Romania is considerable to the $PM_{2.5}$ contamination in Hungary, the combined effect of these two countries is comparable to the effect of Hungary. It can be said that the effect of Italy, Slovakia, Germany, and Serbia could also be considerable,

but the contribution of these countries to the Hungarian $PM_{2.5}$ contamination are essentially affected by the atmospheric conditions.

Finally, the contribution of Hungary to the $PM_{2.5}$ contamination of the neighboring countries was examined. *Fig. 3* shows the results of this investigation.

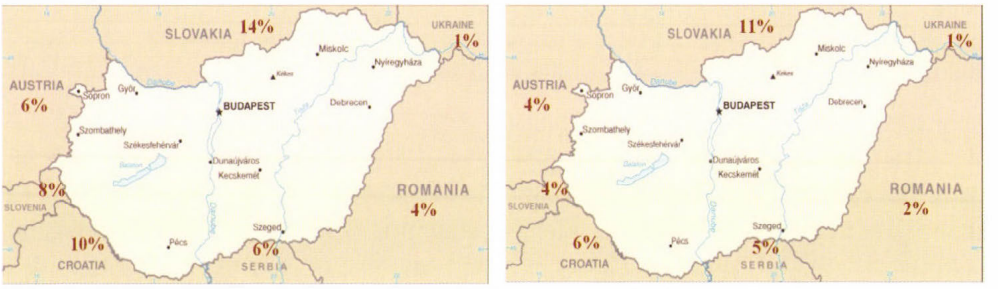

Fig. 3. Contribution of Hungary to the $PM_{2.5}$ contamination of the neighboring countries in the years of 2006 (left) and 2010 (right)(unit:%).

Comparing *Fig. 3* with the pie charts (*Fig. 2*), the amount of the contribution of the Hungarian $PM_{2.5}$ emission to the air pollution conditions in the neighboring countries is similar to their contribution to the Hungarian air pollution. The balance is positive only in the case of Romania, which means that Hungary receives much more particles from Romania than the amount was sent by Hungary to Romania. Hungary significantly pollutes the air of Slovakia, Croatia, and Serbia. Hungary contributes to the air pollution of these countries with 5–20%. The value of this rate depends on the meteorological conditions and the changes in the emission of these countries from year to year.

After specifying Hungary's contribution to the $PM_{2.5}$ air pollution in the surrounding states, it was possible to determine which countries are the net polluters of Hungary and, on the other hand, which countries are polluted by Hungary. The results of this investigation are summarized in *Table 4*.

According to *Table 4* it can be related, that Poland and Romania pollute Hungary much more, than Hungary pollutes these countries. In case of Slovakia the situation is inverse, because Hungary pollutes this country much more than Slovakia pollutes Hungary.

Finally, it was determined that from the particles emitted by Hungary 37 percent remain in the country and 63 percent cross the border of Hungary and increase the $PM_{2.5}$ contaminations of other countries. Considering the total emission of the modeling domain in case of Hungary the amount of aerosols particles arrive to the area of Hungary from outside sources are 30% more than those emitted by Hungary in all.

Table 4. The proportion of the received and sent polluted particles from the point of view of Hungary.

Year	Poland		Romania		Serbia		Slovakia	
	received	sent	received	sent	received	sent	received	sent
2006	13%	4%	11%	4%	6%	6%	6%	14%
2007	12%	2%	7%	4%	8%	5%	7%	9%
2008	7%	2%	10%	3%	8%	5%	6%	12%
2009	10%	3%	10%	3%	8%	5%	7%	11%
2010	12%	2%	11%	2%	8%	5%	7%	11%

The results of this investigation can be summarized as follows: the long-range transport is very determinant in Central Europe, and could not be neglected in the transport model calculations.

2.3. Effect of the weather conditions

PM_{10} concentrations exceed the threshold value mainly in winter and fall. In summer, high PM_{10} concentrations can be observed very rarely. We think, that the effect of special meteorological situations are determinant in the high level PM_{10} concentration formations (*Barmpadimos et al.,* 2011; *Mok* and *Hoi.,* 2005). In this paragraph we examine the effect of some meteorological parameters on the PM_{10} concentration. In Budapest, an air quality network of 10 stations detects the hourly concentration values of PM_{10}, we used this database.

2.3.1. Seasonal effects

Examining the past few years, it shows that high PM_{10} air quality conditions were observed especially in the winter semester. In order this statement could be supported by measurements we examined the PM_{10} data of the Gilice tér air quality monitoring station in Budapest. Those days were selected, when the daily average of the PM_{10} concentration values exceeded the limit value for the protection of human health (50 $\mu g/m^3$). The results of the study are shown in *Fig 4.*

Fig. 4 shows, that the exceedance of the limit values can be observed especially in fall and winter, in spring and summer this situation is very rare. The picture also shows a threshold value (red line) which means that the PM_{10} daily mean value may not exceed 50 $\mu g/m^3$ more than 35 times in a year. In the last years it was usual that the PM_{10} daily values exceeded the limit values for the protection of human health more than 35 times, except in 2009. *Fig 4* shows the result of the investigation only for the monitoring station „Gilice tér", but the situation is the same not only in Budapest, but in case of all of the Hungarian air

quality monitoring stations. How can we explain that high PM_{10} concentration levels can be observed in Hungary especially in fall and winter in Hungary? Due to the fact that the emission and the weather situation determine the PM_{10} concentration together, the seasonal variability of these two effects has to be analyzed. In the case of PM_{10}, the most significant emissions originate from the traffic and residential wood and cool combustion. From the two factors, only the residential combustion has essential seasonal variability.

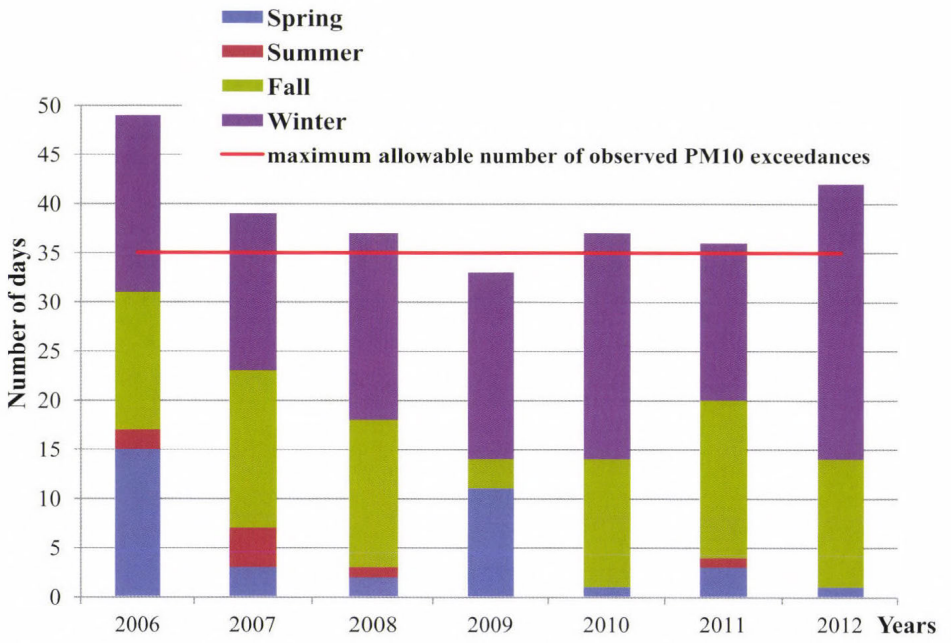

Fig. 4. Exceedance days of air quality threshold (health protection) values of PM_{10} (Budapest, Gilice tér, 2006–2010)

Beside the emission, weather situations also change from season to season in the Carpathian Basin. The typical weather situation, which favors the development of high PM_{10} concentration occurs primarily in the winter season. Furthermore, these weather situations, and meteorological parameters, which can be linked to these meteorological situations, will be examined in more detail.

Not the conventional meteorological measurements, but the grid point data of the numerical weather prediction models are used in the experiments, because we had to produce that type of parameters, which are not measurable or not possible to be calculated from the classical measurements. In this study we used the results of two different numerical weather prediction models to eliminate the

differences in the parameterization methods of the two NWP models (finally, in the results, there was no significant difference).

The features of the two numerical weather prediction models used in the examination are as follows:

AROME (Applications of Research to Operations at MEsoscale) is an atmospheric non-hydrostatic modeling system, which includes a state-of-the-art numerical weather prediction model and a data assimilation system. The horizontal resolution of the model domain is 2.5 km with 60 vertical model levels. The model is used primarily for ultra-short-term forecasting and runs at the Hungarian Meteorological Service's supercomputer four times a day.

WRF (Weather Research and Forecasting) is a versatile numerical weather prediction model, which was developed at the National Center for Atmospheric Research (NCAR) and U.S. National Oceanic and Meteorological Service (NOAA) in cooperation with many research institutes and universities. Operational WRF model used by the Hungarian Meteorological Service with high resolution (2.6 km) and non-hydrostatic configuration. The service runs four times a day on a supercomputer.

2.3.2. Effect of the planetary boundary layer (PBL)

One of the most important parameter of the diffusion processes is the planetary boundary layer (PBL) height. The planetary boundary layer is defined as the part of the atmosphere that is strongly influenced directly by the presence of the surface of the earth, and responds to surface forcings with a timescale of about an hour or less (*Holton,* 1992). In the boundary layer the horizontal transport is dominated by the mean wind and the vertical by the turbulence. When pollutants are emitted into this layer, they dispersed horizontally and vertically because of the action of convection and mechanical turbulences until it becomes completely mixed.

The height of this layer cannot be measured directly, but many methods are known to determine it. In this work, two different numerical weather prediction models, AROME and WRF were applied to determine the PBL height values using different PBL parameterization schemes. In the Hungarian version of the WRF model, the BouLac PBL scheme (*Bougeault et al.,* 1989) was used to calculate the PBL height. The BouLac PBL scheme is classified as a one-and-a-half order turbulent kinetic energy (TKE) closure scheme, which determines the diffusion coefficients from the prognostically calculated TKE. In the Hungarian version of the AROME model, the top of the PBL height is determined by the momentum flux profile method (*Szintai* and *Kaufmann,* 2008). The top of the PBL is the height where the momentum flux value becomes less than 5 percent of the surface level momentum flux value.

Because the numerical weather prediction models determine the PBL height using different parameterization schemes, we determined the connection between the two differently determined PBL height, and the PM_{10} concentration values.

In our examination the hourly average PM_{10} concentration values were used, that are measured between October 27 and November 26, 2011 at the air quality monitoring station Gilice tér, and the hourly PBL height determined by the two mentioned numerical weather prediction models. The examined time period is the longest PM_{10} episode situation which has been detected since the PM_{10} measurements started in Budapest. *Fig 5* shows the relationship between the two parameters.

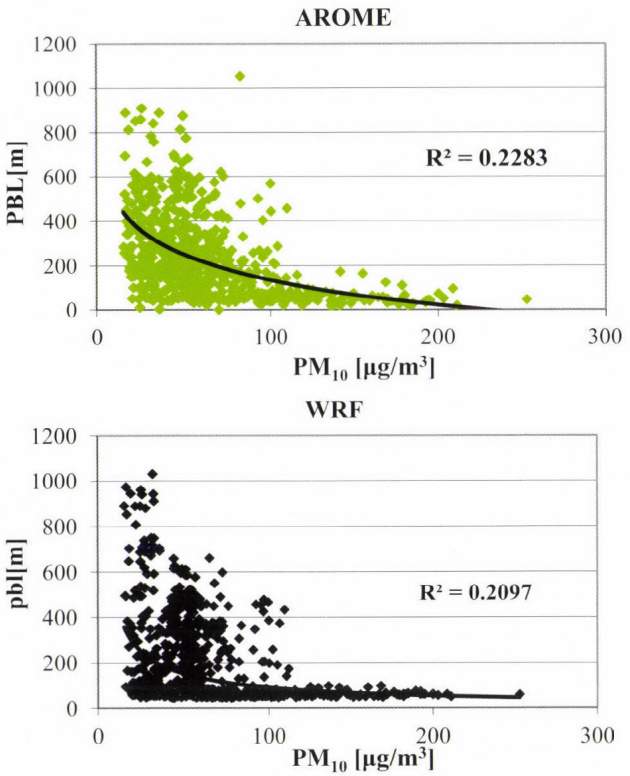

Fig. 5. The relationship between the height of the planetary boundary layer (PBL) and the PM_{10} concentrations (Budapest, Gilice tér).

According to *Fig. 5,* in case of high (>100 µg/m^3) PM_{10} concentration values the PBL heights were lower than 200m. Nevertheless, this statement is not true in another direction, because in case of low PBL height the PM_{10} concentration is not so high in every cases. Regression analysis was also performed to determine the connection between the PM_{10} concentration and PBL height hourly values. There is not big difference between the results of AROME and WRF models. The value of the regression is a little bit higher in case of AROME.

2.3.3. Effect of the stagnation index (SI)

Because the results of the analysis with the PBL height was not convincing to find the weather conditions resulting high PM_{10} concentration level, we took into the analysis other meteorological parameters. While the PBL height characterizes the intensity of the vertical diffusion in the atmosphere, the magnitude of wind speed and wind shear could be the index of the intensity of the horizontal diffusion. The SI index is the parameter (*Holst et al.* 2008), which characterizes the intensity of the horizontal and vertical diffusion in the lower layer of the atmosphere as it takes into account the height of the PBL and the wind speed in the surface layer. The SI index can be determined by this simple equation:

$$SI = \sqrt{\frac{10^6}{PBL \times v}}$$

Fig. 6 shows the relationship between the SI index and the PM_{10} concentration. According to *Fig. 6*, the relationship between the SI index and the PM_{10} concentration is slightly stronger, than the relationship between the PBL height and the PM_{10} concentration. Based on this study we can conclude that the weak mixing processes in the planetary boundary layer (low PBL heights and low wind speed) are responsible for the formation of high PM_{10} concentrations with 25%, and there is no big difference between the results, which was based on the WRF or AROME numerical weather prediction models.

2.3.4. Effect of the wind speed

The analysis so far basically studied the effect of the intensity of the atmospheric diffusion processes on the PM_{10} concentration. However, the atmospheric processes may be relevant in terms of the region from where the polluted air arrived to the area of the measuring point. In this respect, the effect of wind direction is essential. Using this analysis, clean and dirty sectors could be separated in the area of the monitoring station, and changes in the emission intensity and compositions could be inferred.

In this analysis, PM_{10} data detected by the air quality monitoring station Gilice tér, as well as the measured meteorological data between January 9, 2006 and February 14, 2012 are used. In case of this examination we halved the day to daytime and nighttime. *Fig. 7* shows the dependence of the PM_{10} concentrations on the wind direction in daytime and nighttime. The results are significantly different in the different parrt of the day. For daytime episode situation, the effect of traffic emission from the direction of M5 highway can be observed, while nighttime the effect of domestic heating from the direction of the residential district can be observed.

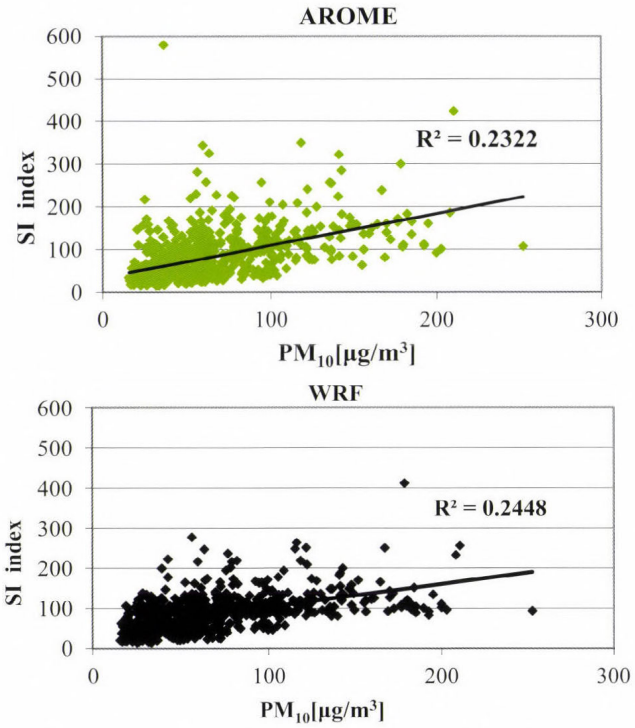

Fig. 6. The relationship between the SI index and the PM_{10} concentrations. (Budapest, Gilice tér).

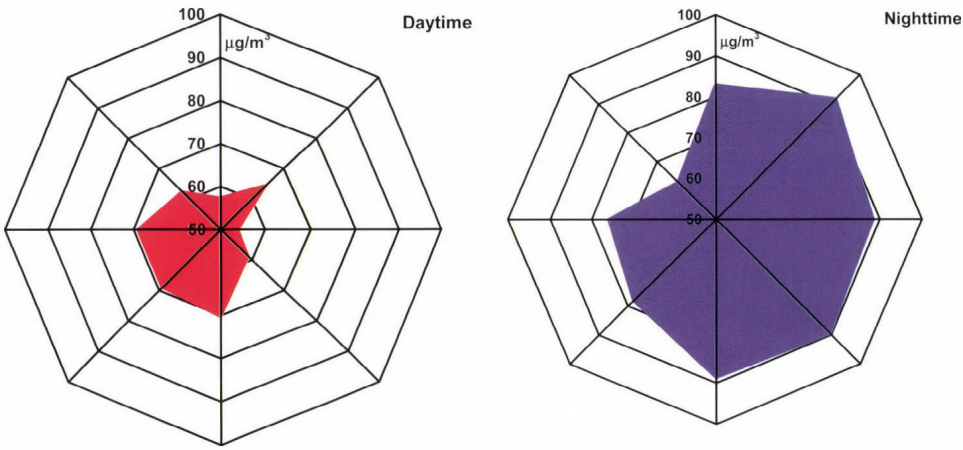

Fig. 7. Wind direction dependency of the PM_{10} concentrations in episode situations for daytime and nighttime. (Budapest, Gilice tér).

Based on *Fig. 7*, it is likely that during the day the traffic emission and during the night the domestic heating is the primary source of PM_{10} pollution in the area of Gilice tér station. It is worth to compare the highest average concentration values, which was detected in daytime and nighttime. During the day, the average hourly maximum concentration was 70 $\mu g/m^3$, while at night it was 90 $\mu g/m^3$, which could be explained with the low boundary layer at night, but it is possible that the level of emissions from residential combustion is greater than the traffic emission.

3. Validation of the PM_{10} forecast for Budapest

The Hungarian Meteorological Service adopted a chemical transport model to forecast the concentration values of the main pollutants. The forecasting tool is an integrated system of the WRF meteorological and CHIMERE chemical transport models. The air quality prediction system has been operating since June 1, 2010, which means, that there are longer than 2-year data sets to evaluate how it is working. In the validation work the PM_{10} data detected by the air quality monitoring network of Budapest, as well as the forecasted air pollutant concentration values of the air quality prediction model system are used. The values of NMSE (normalized mean square error) and correlation were determined for the PM_{10} pollutants and for the grid points, where the air quality monitoring stations are located. NMSE is a typical statistical indicator of the overall deviations between predicted and measured values. Low values mean, that the model is well performing both in space and time. The correlation coefficient is a measure of how well the predicted values from a forecast model "fit" the real-life data. The values indicate that the best forecast can be expected in the area of Honvéd utca monitoring station (the correlation value is 0.53) and the worst in the area of Pesthidegkút monitoring station (the correlation value is about 0.15) for PM_{10}. *Table 5* shows all the results of this examination.

The results of this evaluation work shows, that the PM_{10} concentration prediction is not so good. There is big lack in the emission input data base calculated for PM_{10}, mainly in the domestic heating, which is reflected in the case of Pesthidegkút monitoring station, for which the values of NMSE and correlation are very bad. Presumably there are some problems with our traffic emission data base, and sometimes the NWP model is not able to predict well the essential meteorological parameters, which have effect on the PM_{10} concentration (*Saide et al.,* 2011).

In the future we plan to develop our emission database, determine new boundary conditions. We hope, that this investigation will result in an improvement in the PM_{10} forecast.

Table 5. NMSE and correlation values of the PM_{10} prediction

Station	NMSE	Correlation
Csepel	0.97	0.39
Erzsébet tér	0.35	0.49
Gergely utca	0.40	0.45
Gilice tár	0.57	0.31
Honvéd	0.31	0.53
Kőrakás park	0.14	0.36
Kosztolányi tér	0.36	0.33
Pesthidegkút	0.88	0.15
Széna tér	0.50	0.35
Teleki tér	0.45	0.49
Tétényi út	0.64	0.19

4. Conclusion

In this study, we tried to determine the contribution of the effect of the long-range transport and meteorological conditions to the Hungarian PM_{10} and $PM_{2.5}$ air pollution. In case of the long-range transport, the study tool was the EMEP chemical transport model, and the results of this model calculations were the bases of examination.

The conclusions drawn from the calculations are:

- In Hungary, the contribution of the long-range transport to the PM air pollution is 70–80%.
- The effect of the long-range transport shows significant spatial variability, the most important part is the western frontier of Hungary, and the smallest is the central part of the country.
- Among the European states, Romania and Poland are the greatest polluters of Hungary's atmosphere.
- Particles emitted by Hungary contribute significantly to the PM pollution of Slovakia, Serbia, and Croatia.
- 37% of the particulate matters emitted by Hungary remain in the country, and 63% cross the border of Hungary and increase the PM contaminations of other countries.
- In case of Hungary, the aerosol particles arrive to the area of Hungary from outside sources are 30% more than the particles emitted by the country in all.
- The reasons of the formation of PM_{10} related to high air pollution situations are: unfavorable weather conditions and increasing emission of the domestic heating. Among the meteorological parameters, the effect of the SI index is the most significant.

A dispersion modeling system was developed by the Hungarian Meteorological Service to predict the air quality in Budapest for 48 hours. The core of this system is the CHIMERE chemical transport model. Beside the CHIMERE's built-in emission database, also own emission data (point sources, traffic count) for Budapest are used during modeling. It was shown that the quality of the results depends on the quality of the weather forecast, the long-range transport, and the emission database. It was also demonstrated that there is a lack in the emission input database calculated for PM_{10}. Long-term transport of the pollutants seems to play an important role during concentration calculations. Validation of the system also confirms these statements.

References

Barmpadimos, I., Hueglin, C., Keller, J., Henne, S., and. *Prévôt, A.S.H.,* 2011: Influence of meteorology on PM_{10} trends and variability in Switzerland from 1991 to 2008, *Atmos. Chem. Phys. 11*, 1813–1835.

Bernard, S.M., Samet, J.M., Grambsch, A., Ebi K.L., and *Romieu, I.,* 2001: The Potential Impacts of Climate Variability and Change on Air Pollution-Related Health Effects in the United States. *Environ.Health Perspect. 109*, 199–209.

Bougeault, P. and *Lacarrére, P.*, 1989: Parameterization of orography-induced turbulence in amesobeta-scale model. *Mon. Weather Rev. 117*, 1872–1890.

Demuzere, M., Trigo, R.M., de Arellano, J.V., and van *Lipzig, N.P.M.*, 2009: The impact of weather and atmospheric circulation on O_3 and PM_{10} levels at a rural mid-latitude site, *Atmos. Chem. Phys. 9*, 2695–2714.

EMEP Status Report 1, 2012: "Transboundary acidification, eutrophication and ground level ozone in Europe in 2010" Joint MSC-W & CCC & CEIP Report

Gauss, M., Nyíri, Á., Steensen, B.M., and *Klein, H.*, 2012: MSC-W Data Note 1: Transboundary data by main pollutants (S, N, O_3) and PM: Hungary. Oslo: Norwegian Meteorological Institute.

Holst, J., Mayer, H., and *Holst, T.,* 2008: Effect of meteorological exchange conditions on PM_{10} concentration. *Meteorol. Zeit. 17*, 273–282.

Holton, J.R., 1992: An Introduction to Dynamic Meteorology. *Academic Press*, New York.

Mok K.M. and *Hoi, K.I.,* 2005: Effects of meteorological conditions on PM10 concentrations - A study in Macau, *Environ. Monit. Assess. 102*, 201–223.

Saide, P.E; Carmichael, G.R; Spak, S.N; Gallardo, L., Osses, A.E., Mena-Carrasco, M.A., and *Pagowski, M.,* 2011: Forecasting urban PM_{10} and $PM_{2.5}$ pollution episodes in very stable nocturnal conditions and complex terrain using WRF–Chem CO tracer model. *Atmos. Environ. 45*, 2769–2780.

Sillanpää, M., Hillamo, R., Saarikoski, S., Frey, A., Pennanen, A., Makkonen, U., and *Salonen, R.O.,* 2006: Chemical composition and mass closure of particulate matter at six urban sites in Europe. *Atmos. Environ. 40*, 212–223.

Simpson, D., Benedictow, A., Berge, H., Bergström, R., Emberson, L.D., Fagerli, H., Flechard, C.R., Hayman, G.D., Gauss, M., Jonson, J.E., Jenkin, M.E., Nyíri, A., Richter, C., Semeena, V.S., Tsyro, S., Tuovinen, J.-P., Valdebenito, Á., and *Wind, P.*, 2012: The EMEP MSC-W chemical transport model – technical description. *Atmos. Chem. Phys., 12*, 7825–7865,

Szintai, B., and *Kaufmann, P.,* 2008: TKE as a measure of turbulence. *COSMO Newsletter 8*, 2–9.

WHO, 2011: Explosure to air pollution (Particulate Matter) in outdoor air (available at web site: http://www.euro.who.int/__data/assets/pdf_file/0018/97002/ENHIS_Factsheet_3.3_ July_2011.pdf

IDŐJÁRÁS

Quarterly Journal of the Hungarian Meteorological Service
Vol. 117, No. 4, October–December, 2013, pp. 377–402

Application of a detailed bin scheme in longwave radiation transfer modeling

Eszter Lábó*[1] and **István Geresdi**[2]

[1]*Hungarian Meteorological Service,*
P.O. Box 38, H-1525 Budapest, Hungary

[2]*Szentagothai Research Center, University of Pécs,*
Ifjúság útja 20, H-7624 Pécs, Hungary

Corresponding author E-mail: labo.e@met.hu

(Manuscript received in final form October 15, 2013)

Abstract—Absorption and transfer of radiation in clouds are sensitive to size distribution of water drops. A new numerical scheme has been developed for calculating the extinction coefficients of water clouds in the longwave region. While the generally applied bulk schemes in numerical models characterize the whole size distribution of the water droplets with one parameter (effective radius), detailed models allow us to calculate the optical properties without any assumption about the size distribution of water drops. Our model uses a bin microphysical scheme which uses the number concentration and mixing ratios of water in 36 size intervals.

This paper describes the developed bin radiation scheme. The wavelength-dependence of extinction coefficients calculated by bin and bulk schemes is compared at different effective radius. It was also investigated how the number concentration of droplets and liquid water content affect the difference between the two schemes. The relative difference depends both on the effective radius and on the wavelength. If the effective radius is larger than 10 μm, the relative difference remains below 20%. It is higher in the case of smaller effective radius.

The bin scheme has also been implemented in the RRTM LW radiation transfer model code. Upward, downward, and net radiation profiles for four different cases were studied with the RRTM model. It was found that the outgoing longwave radiation is sensitive on the applied scheme when the cloud layer is thin. Significant differences were found between the gradients of the net longwave radiation profiles in all cases. These differences have significant impact on the evolution of the vertical temperature profiles, which affects both cloud dynamics and microphysics.

Key-words: longwave radiation, bin scheme, numerical modeling, cloud-radiation interaction, water clouds, cooling rate

1. Introduction

The large impact of clouds on the temperature profiles and radiation budget stirs the need for a more accurate modeling of cloud-radiation interactions (*Ramanathan* and *Inamdar,* 2006; *Corti* and *Peter,* 2009). Recent research focuses on the development of more precise calculation methods of radiative cloud forcing (*Liu et al.,* 2009). Besides models, measurement campaigns have been launched to determine the effect of cloud radiative forcing on the Earth's atmosphere (*Arking,* 1991, *Chen et al,.* 2000). It is widely accepted that the clouds decrease the shortwave radiative flux at the surface by 40–50 Wm–2 , and they also decrease the outgoing longwave radiative flux by around 30 Wm–2 (*Ramanathan et al.,* 1989; *Wielicki et al.,* 1996; *Rossow* and *Duenas,* 2004). These effects result in a net diminution of 10–20 Wm–2 (*Chen* and *Rossow,* 2002; *Oreopoulos* and *Rossow,* 2011). However, the determination of the radiative forcing for each cloud and cloud type requires exact numerical models including accurate parameterization of cloud physical processes.

The necessity of a more detailed cloud radiation schemes in the modeling of cloud-radiation interactions has been permanently suggested during the last 30 years. It has been asserted by *Kunkel* (1984) and later by *Fouquart et al.* (1990) that a more accurate parameterization of cloud-radiation interactions is essential. *Buriez et al.* (1988) stated that until the '90s, optical characteristics had been tuned in the atmospheric models by arbitrary diagnostic cloud schemes to fit the results to the observations. *Harrington* (1997) showed that the applied parameterization technique in models strongly affects the optical properties of the simulated clouds. *Stephens* (2004) proved that the cloud properties such as optical depth, liquid and ice water contents, and particle size distribution significantly affect the radiation budget of Earth. Lack of correct data about optical properties of clouds is one of the major obstacles in determining the radiation budgets both of atmosphere and surface. According to *Stephens* (2004), the effect of clouds on heating and cooling of the atmosphere is a substantial feedback mechanism that had not been adequately investigated. Improvement in the numerical forecasting capacities of a weather forecasting model has been demonstrated in *Liu et al.* (2009). They have included detailed radiation scheme with microphysical size dependence in the U.S. Navy's Coupled Ocean-Atmosphere Mesoscale Prediction System (COAMPS) model. It has ultimately reduced the model's systematic warm bias, and overestimation of humidity in the upper troposphere. Comparing with measurements, the root mean square error of LW downward flux has changed from 17.67 Wm–2 to 9.44 Wm–2 in the case of standard model, and that of improved radiation model, respectively. *Petters et al.* (2012) highlighted that cloud radiative heating, and its feedback on cloud dynamics is largely sensitive to the number concentration of water droplets in stratiform clouds.

In numerical models, optical properties of warm clouds such as single scattering albedo and extinction coefficient are generally calculated by using a characteristic size of cloud droplets (*Lindner* and *Li,* 2000; *Ebert* and *Curry,* 1992). In these bulk schemes the size distribution of the droplets is generally given by an idealized gamma function with one or two independent parameters (*Ritter* and *Geleyn,* 1992; *Walko et al.*, 1995; *Straka et al.,* 2007; *Tompkins* and *Di Giuseppe,* 2009). The bulk models use the effective radius of cloud droplets and liquid water content to determine the optical properties (*Fu et al.,* 1998; *Hong et al.,* 2009, *Gettelman et al.,* 2008). Contrary to bulk schemes, bin microphysical schemes are capable to describe arbitrary size distribution of cloud droplets. In the case of bin schemes no assumption is needed on the droplet size distribution. While the bin schemes for the numerical simulation of cloud microphysical processes has been widely used since the early nineties, the application of this technique to calculate the optical properties of the clouds has become in the focus of researches in the last ten years. The advantage of the application of bin schemes for the calculation of cloud optical properties was proved by *Harrington* and *Olsson* (2001). They showed that the longwave radiation budget at the surface can be altered by 40 Wm^{-2} depending on how the effective radius of cloud droplets was calculated. The impact of using bin models on the cloud microphysical structure has been examined in *Harrington et al.* (2000). He has evaluated the effect of radiative cooling on the growth of water droplets. He showed that larger drops were growing faster than smaller drops. Drizzle-sized drops could be produced from 20 to 50 min earlier through the inclusion of the radiative term, which leads to a higher potential for enhancing drop collection and precipitation formation.

In this paper results about a new bin radiation scheme are presented. This technique was developed to calculate the extinction coefficients of water droplets in the infrared region. The impact of application of this new scheme on the longwave radiation budget is presented. The next section contains the description of the scheme. The results about the comparison with a bulk scheme are presented in Section 3. In Section 3.1, the changes in the extinction coefficients are presented. In Section 3.2, the change in the intensity of longwave radiation due to the application of bin scheme compared to the bulk scheme is studied. Section 3.3 examines the changes in the radiation profile with the help of the RRTM radiative transfer model, caused by the difference in the extinction coefficients. The conclusions are given in Section 4.

2. *Description of the model*

2.1. Description of the bin scheme

The optical parameters describing scattering, extinction, and absorption of radiation in clouds are: the extinction and scattering coefficients (β_{ext} and β_{sca});

the single scatter albedo (ω), which is the ratio of scattering in total extinction; and the asymmetry parameter (g), which characterizes the angle-dependence of the scattering (*Roach* and *Slingo,* 1979; *Stephens,* 1984; *Hu* and *Stamnes,* 1993). The definitions of these parameters for a given wavelength, in the case of water droplets assumed to be spherical are given in Eq. (1)–(4).

$$\beta_{ext}=\int_0^\infty A(D)Q_{ext}(D,m,\lambda)n(M)\,dM \quad , \tag{1}$$

$$\beta_{sca}=\int_0^\infty A(D)Q_{sca}(D,m,\lambda)n(M)\,dM \quad , \tag{2}$$

$$\omega=\frac{\beta_{sca}}{\beta_{ext}} \quad , \tag{3}$$

$$g=\frac{1}{2}\int_{-1}^{1} p(\mu)\mu\,d\mu \quad , \tag{4}$$

where D is the droplet diameter, M is the mass of the droplet, λ is the wavelength, $n(M)$ is the droplet size distribution as a function of M, Q_{ext} is the extinction efficiency, Q_{sca} is the scattering efficiency, μ is the cosine of the scattering angle, and $p(\mu)$ is the phase function. m is the refraction index, $A(D)$ is the cross section.

The radiation transfer models and numerical models calculate the radiative transfer over radiation bands instead of calculating it at single wavelengths. For this purpose, a so-called broadband extinction coefficient is defined for an arbitrary wavelength interval of $\Delta\lambda$ (*Slingo* and *Schrecker* (1982)):

$$\beta_{ext}=\left(\int_{\Delta\lambda} E_\lambda \int_0^\infty A(D)Q_{ext}(D,m,\lambda)n(M)dM\,d\lambda\right)/\int_{\Delta\lambda} E_\lambda\,d\lambda \quad , \tag{5}$$

where E_λ is the Planck-function at a reference temperature (usually at 273 K). Bin scheme presented in details in *Rasmussen et al.,* (2002) is used to calculate the above integrals. The size range from 1.5625 μm to 5.07968 mm is divided into 36 bins with doubling the mass at the bin edges. The applied moment conserving technique allows us to describe the size distribution of water drops in every bin:

$$n_k(M)=A_k+M\cdot B_k\,. \tag{6}$$

The coefficients A_k and B_k are calculated from the number concentrations and mixing ratios in the kth bin (see more details in *Tzivion et al.*, 1987). Using the bin scheme the Eq. (5) can be approximated by the following equation:

$$\beta_{ext} = \sum_{k=2}^{N_{bins}} [\int_{\Delta\lambda} (E_\lambda \int_{M_{k-1}}^{M_k} A(D) Q_{ext}(D, m, \lambda) n_k(M) dM d\lambda) / \int_{\Delta\lambda} E_\lambda d\lambda] \quad , \quad (7)$$

where N is the number of the bins, furthermore, M_{k-1} and M_k are the mass of the water drops at the edges of the kth bin.

The extinction coefficients can be calculated in every bin over any arbitrary wavelengths interval of $\Delta\lambda$. E_λ was calculated at T=273 K in this research. Sensitivity of the extinction coefficients on the temperature was investigated by calculating the above integral at T_1=303 K and T_2=243 K. Differences were found to be insignificant for the extinction coefficients for the whole infrared spectra. Comparing to the case of T=273 K, in the case of T_1 a little bit smaller value was calculated (the maximum difference was 0.17%), and in the case of T_2 a slightly larger value was calculated (maximum difference was 0.29%). Thus, the temperature dependence of extinction coefficients is neglected in this study.

The Q_{ext} extinction efficiency can be evaluated on the base of the Lorentz-Mie theory; however, it cannot be analytically calculated even in the case of spherical water drops. Instead of using time consuming numerical methods, the modified anomalous diffraction theory (MADT) was applied to describe the optical properties of water drops. *Mitchell* (2000) proved that application of this theory results in small errors comparing to the Lorentz-Mie theory. According to MADT, the extinction efficiency can be defined as a sum of two different components: the corrected Q_{ext}, and Q_{edge}:

$$Q_{ext,m}(D, \lambda, m) = (1 + \frac{C_{res}}{2}) Q_{ext} + Q_{edge} \quad . \quad (8)$$

The details about calculation of C_{res}, Q_{ext}, and Q_{edge} variables can be found in Appendix A.

As the $Q_{ext}(D,\lambda,m)$ function has been given in explicit form, the integrals in Eq. (7) can be calculated by taking into consideration the $n_k(M)$ size distribution given by Eq. (6). The evaluation of the integrals in Eq. (7) can be made to be very fast, if two two-dimensional kernels were precalculated over the two-dimensional grid defined by both mass intervals and wavelength intervals of the radiative transfer model described in Section 2.3.

The details about the calculation of $K_{Akj}(M_{k-1}, M_k, \Delta\lambda_j)$ and $K_{Bkj}(M_{k-1}, M_k, \Delta\lambda_j)$ are given in Appendix B. These coefficients can be implemented in the radiative transfer model afterwards, to yield extinction coefficients for the new bin method.

2.2. *Description of the bulk scheme*

Because the computational cost of the bin scheme is high, it is important to investigate whether the optical parameters defined by the Eqs. (1) – (4) are sensitive on the method they are calculated. In this study, extinction coefficients (Eq. (1)) obtained by bin scheme are compared to the extinction coefficients obtained by a bulk scheme method (*Hu* and *Stamnes,* 1993). This parameterization is currently used to calculate extinction coefficients in the RRTM LW radiation transfer model. More details about this model are given in Section 2.3.

The method developed by *Hu* and *Stamnes* (1993) is a frequently applied bulk parameterization scheme, which uses the effective radius and the liquid water content (*LWC*) as input parameters:

$$\beta_{ext} / LWC = a r_e^b + c \quad . \tag{9}$$

The *a, b, c* coefficients are defined for the following three intervals of the effective radius: 2.5–12 μm; 12–30 μm; and 30–60 μm, and for 50 wavelength bands in the infrared spectrum. This scheme is based on Mie-scattering calculations, which is appropriate method to determine the Q_{ext} (D,m,λ) extinction efficiency, at any wavelengths and droplet diameters. The $n(M)$ droplet size distribution was assumed to be a gamma-size distribution:

$$n^*(r) = \frac{N_0}{\Gamma(\gamma) r_m} \left(\frac{r}{r_m}\right)^{\gamma - 1} \exp^{-r/r_m} \quad , \tag{10}$$

where N_0 is the total (volume) number concentration, Γ is the gamma function, r_m is the characteristic radius of the size distribution, and γ is a constant, that defines the shape of the distribution (*Stephens et al.*, 1990).

The *a, b, c* coefficients were calculated by least-square fitting of Eq. (9) on the set of extinction coefficients related to data pairs of effective radius and liquid water content. The effective radii and liquid water content were calculated by using different shape parameters (γ), characteristic sizes (r_m), and total number concentrations (N_0) in Eq. (10). This group of data was set up for 50 predefined wavelengths, ranging from 3.9 μm to 150 μm (*Hu* and *Stamnes,* 1993).

2.3. *Description of the radiative transfer model*

The RRTMG LW (rapid radiative transfer model for the longwave radiation) (*Clough et al.*, 2005) radiation model is used in our studies to calculate the longwave fluxes in the case of different clouds. It has been developed for the

calculation of longwave atmospheric fluxes and cooling rates in atmospheric radiative transfer studies, as well as for implementation in numerical weather prediction and climate models.

The longwave spectrum is divided into 16 bands in the RRTM, from 3.33 μm to 1000 μm, according to the main absorption bands of the atmospheric gases at different wavelengths (*Table 1*). These bands have been determined to have maximum two main absorbing compounds in each band; to limit the variation of the Planck function within the bands; and to keep the number of bands minimized as possible while keeping the previous two conditions. The model is capable to take into account the radiative effects of water vapor, carbon dioxide, ozone, nitrous oxide, methane, oxygen, nitrogen, and halocarbons. The two main compounds (water vapor, carbon dioxide) were taken into consideration in present calculations.

Table 1. Wavelengths intervals of the RRTM model

Band	Wavelength (μm)	1050–96 (hPa)	96–0.01 (hPa)
16	40.00 – 1000.00	H_2O	H_2O
15	20.00 – 40.00	H_2O	H_2O
14	15.90 – 20.00	H_2O, CO_2	H_2O, CO_2
13	14.30 – 15.90	H_2O, CO_2	CO_2, O_3
12	12.20 – 14.30	H_2O, CO_2	CO_2, O_3
11	10.20 – 12.20	H_2O	–
10	9.26 – 10.20	H_2O, O_3	O_3
9	8.47 – 9.26	H_2O	O_3
8	7.19 – 8.47	H_2O, CH_4	CH_4
7	6.76 – 7.19	H_2O	H_2O
6	5.55 – 6.76	H_2O	H_2O
5	4.81 – 5.55	H_2O, CO_2	–
4	4.44 – 4.81	H_2O, N_2O	–
3	4.20 – 4.44	CO_2	CO_2
2	3.85 – 4.20	N_2O, CO_2	–
1	3.33 – 3.85	H_2O, CH_4	–

The development of RRTM has been based on the calculations made by the line-by-line radiative transfer model (LBLRTM) (*Mlawer et al.*, 1997). The absorption coefficients for different temperatures, pressures, and relative amount of the absorption gases have been determined by this model. These constants are imported as look-up-tables into the RRTM model, and linear interpolation is used to calculate the absorption coefficients at the actual temperature, pressure, and gas concentration.

The radiative transfer is calculated in the RRTM model for all of the 16 spectral bands, as if it was a single spectral wavelength. In the case of vertically inhomogeneous layers, it uses the Pade's approximation to calculate effective Planck function for each layer, by using the temperatures at boundaries of layers, and mean layer temperatures (*Clough et al.,* 1992; *Mlawer et al.,* 1995). The variation of the Planck function in a band according to the wavelength is taken into account by weighting according to the abundance of main gas compounds related to the band. (*Mlawer et al.*, 1995).

In RRTM the correlated-k method is used to describe the wavelength-dependency of the absorption coefficients in the radiative transfer equations. The correlated k-technique is an approximation method with high accuracy. It is frequently applied for the calculation of radiative transfer radiances by transforming the integral over wavelength into integral over a cumulative probabilistic function. This function is determined by rearranging the absorption coefficient values in ascending order according to the fraction of the given value in the actual wavelength band (*Mlawer et al.,* 1997). This generates a new order of the absorption coefficients according to their probability. A characteristic average value of the absorption coefficient in a given probability-interval is then defined, and used in the radiative transfer equations to calculate the radiances.

The values of the probability function at given pressure and temperature are calculated beforehand by a line-by-line radiative transfer model. In the RRTM, they are interpolated linearly between the logarithm of temperature and pressure values. Also, linear weighting of the absorption coefficients is done according to their integrated line strengths and column amount, when two different species are dominant in the same spectral band. These simplifications make this method computationally fast, meanwhile keeping the needed accuracy.

Validation of the RRTM model shows that RRTM results agree with those computed by the line-by-line model within 1.0 Wm^{-2} at all levels, and the computed cooling rates agree to within 0.1 K/day in the troposphere and 0.3 K/day in the stratosphere (*Clough et al.,* 2005). The RRTM model has been implemented as the operational code for longwave radiation at the European Center for Medium-Range Weather Forecasts (ECMWF) and in the Global Forecast System (GFS) of the National Centers for Environmental Prediction (NCEP). It is also implemented as one option in the National Center for Atmospheric Research (NCAR) Weather Research and Forecasting (WRF) model.

3. Results

3.1. Comparison of the extinction coefficients calculated by bin and bulk schemes

Extinction coefficients calculated by bin and bulk schemes are compared in this section. The investigated cases are described in *Table 2.* The first column gives

the number concentration, the second, third, and fourth ones show the effective radii if $LWC_1 = 10^{-3}\,\mathrm{kg\,m^{-3}}$, $LWC_2 = 10^{-4}\,\mathrm{kg\,m^{-3}}$, and $LWC_3 = 10^{-5}\,\mathrm{kg\,m^{-3}}$, respectively. The size distributions of the water drops were given by Eq. (10), and the value of γ parameter was chosen to be equal to 3.

Table 2. Effective radius for gamma-distributions for different number of concentration and LWC values

	$LWC_1 = 10^{-3}\,\mathrm{kg\,m^{-3}}$	$LWC_2 = 10^{-4}\,\mathrm{kg\,m^{-3}}$	$LWC_3 = 10^{-5}\,\mathrm{kg\,m^{-3}}$
N_i (*10^6) 1/m^3	r_{eff} (*10^{-6}) m	r_{eff} (*10^{-6}) m	r_{eff} (*10^{-6}) m
1000	7.92	3.68	–
250	12.57	5.84	2.71
100	17.07	7.92	3.67
50	21.50	9.98	4.63
20	29.18	13.55	6.29

It has been found that the changes in the difference between the extinction coefficients calculated by the bin and by the bulk scheme depends mostly on the value of the effective radius of the size distribution, regardless of the values of the LWC and the number concentration of water droplet. E.g., the differences between the bin scheme and the bulk scheme were very similar in the following two cases: $LWC_2 = 10^{-4}\,\mathrm{kg\,m^{-3}}$, $N = 1000 \cdot 10^6\,\mathrm{m^{-3}}$ and $LWC_3 = 10^{-5}\,\mathrm{kg\,m^{-3}}$, $N = 100 \cdot 10^6\,\mathrm{m^{-3}}$.

Fig. 1 summarizes the results obtained at $LWC_1 = 10^{-3}\,\mathrm{kg\,m^{-3}}$ at two different concentrations of the droplets, and *Fig. 2* summarizes the results obtained at $LWC_2 = 10^{-4}\,\mathrm{kg\,m^{-3}}$, at two different number concentrations.

Fig. 1 and *Fig. 2* show that the difference between the extinction coefficients depends both on the wavelength and on the effective radius. Because the surface and the atmosphere emit most of the energy in the wavelength interval of 5–20 μm, the difference between the results of the schemes will be analyzed in this interval. The relative difference can be higher than 20% if the effective radius is lower than 10 μm. There is no significant (maximum 4%) difference between the calculated extinction coefficients if the effective radius is higher than about 10 μm, and the wavelength is less than about 8.0 μm. Although the local minimum values at near to the wavelength of 10 μm given by the different schemes are very similar, the application of the bulk scheme results in much sharper decrease and increase of the extinction coefficients in the wavelength interval of 10–15 μm.

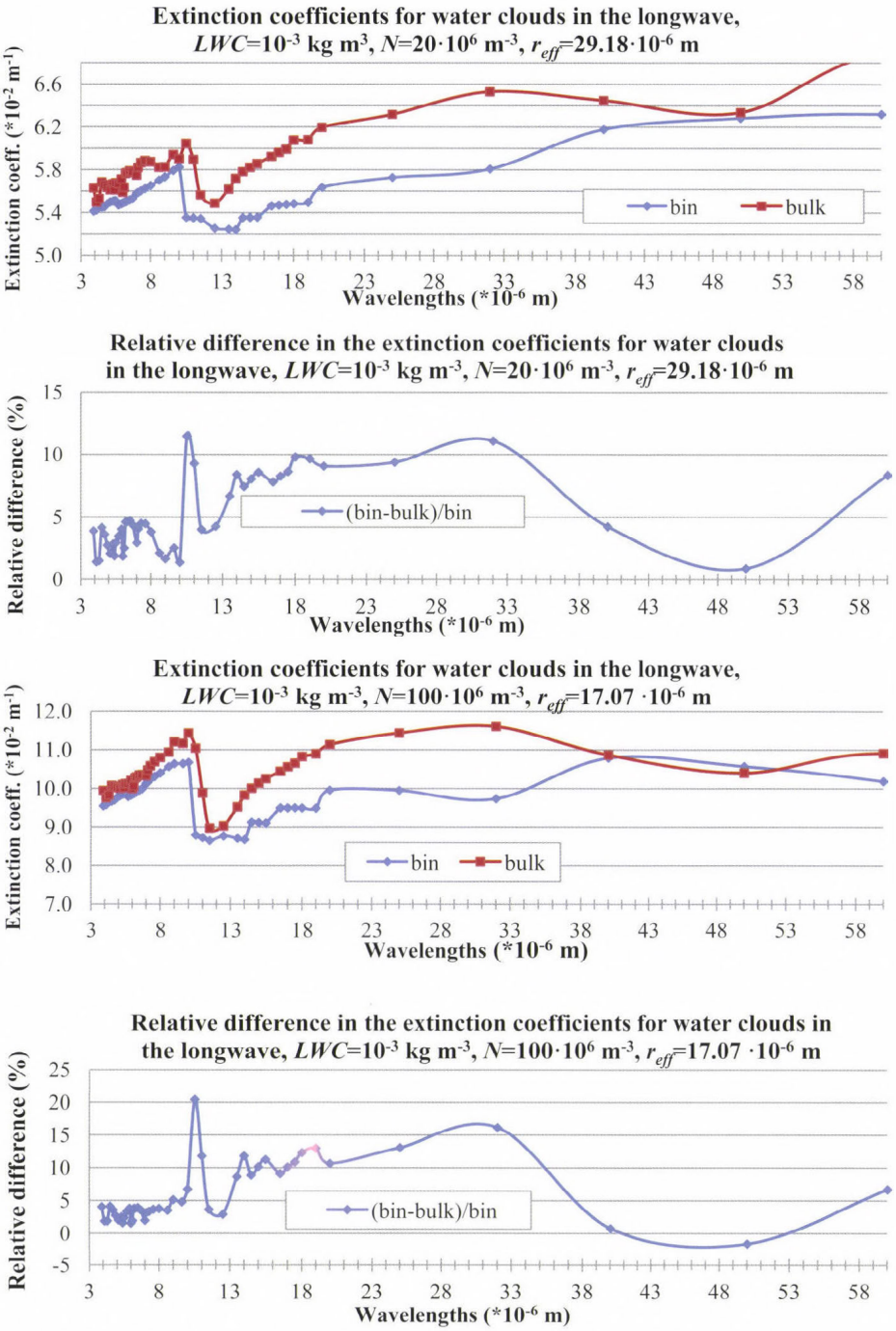

Fig. 1. Extinction coefficients and relative differences calculated for two different gamma-size distributions (N=20, and $100 \cdot 10^6$ m^{-3}, LWC=10^{-4} kg m^{-3}).

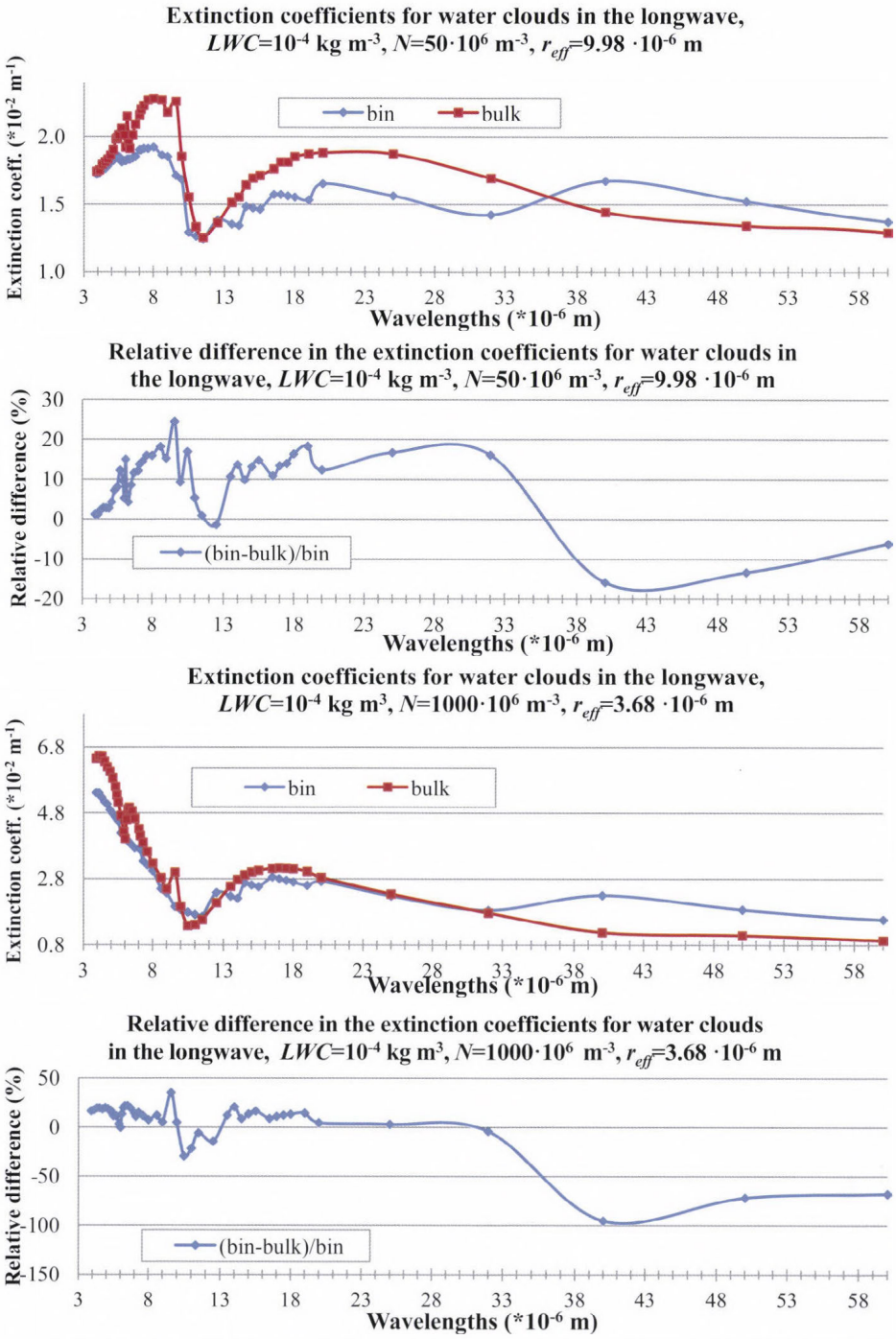

Fig. 2. Extinction coefficients and relative differences calculated for two different gamma-size distributions (N=50, and 1000 10^6 m^{-3}, LWC=10^{-4} kg m^{-3}).

In the critical wavelength interval near to the wavelength of 10 μm – where the absorption of both vapor and CO_2 is relatively small and the absorption of the water drops can be dominant –, significant difference can be found between the results of bulk and that of bin scheme if the effective radius is between 3–15 μm. In this size range, significant positive difference (larger than 10%) can be observed in the whole spectra, except at a narrow wavelength interval of 10–13 μm, where at 9.6 μm wavelength, the difference is much higher for all effective radius values. In case of larger effective radius (>10 μm), the difference is getting smaller, and is getting more emphasized above the wavelength of 10 μm.

It has to be noted that the comparison was made by using idealized gamma size distribution in the case of bin scheme as well. In the real clouds the size distribution of the water drops can significantly differ from the gamma size distribution. The difference between the two schemes shows that the application of effective radius and the liquid water for evaluating the optical properties may results in overestimation of the extinction coefficient mostly in the case of relatively high concentration of the larger water droplets..

It can be established that the bin scheme gives generally smaller value than the bulk scheme does, except at large wavelengths (λ>33 μm), and except at wavelength interval of 10–13 μm in the cases of smaller effective radii. If r_{eff}>20μm, the bulk scheme gives always higher value than the bin scheme does.

From *Figs. 1* and *2*, it can be concluded that the curves related to the extinction coefficients calculated by the bin scheme are smoother; they do not fluctuate by the wavelength as sharply as it can be observed in case of a bulk scheme. The reason for this is that bulk scheme uses only the r_{eff} drop size, and radius much different from this characteristic size are not represented in calculation; whereas the bin scheme allows us to take into account the extinction caused by any drop sizes.

3.2. Comparison of the longwave outgoing radiations at top of cloud layer

In this section results about the longwave outgoing radiation at the top of a cloud layer are presented. The calculations were made for 100 m deep cloud layers with different liquid water contents and drop concentrations. To focus on the effect of water drops, the absorption of the vapor and that of CO_2 was not taken into consideration in the radiative transfer model in this section. It was assumed that the cloud base temperature is 293 K and the vertical temperature gradient is wet adiabatic. The emitted thermal radiation goes through the 100 m thick cloud characterized by different microphysical parameters. The number concentration and *LWC* values of these clouds are given in *Table 1*. The cases presented in *Figs. 3* and *4* are the same cases as in *Figs. 1* and *2*.

The RRTM model described in Section 2.3 was used for calculating the radiation transfer. The new bin scheme has been implemented into the RRTM

model. The two dimensional arrays of K_{Akj} $(M_{k-1}, M_k, \Delta\lambda_j)$ and K_{Bkj} $(M_{k-1}, M_k, \Delta\lambda_j)$ were precalculated, and were used during the simulations.

This development is a novel one, as the RRTM model has been capable to use only the bulk scheme described in Section 2.2. In the case of bulk scheme, the input parameters for the cloud profiles are the effective radius and the cloud water path (which is the LWC multiplied by cloud thickness). Now RRTM can be coupled to a detailed microphysical model, which gives the thickness of the cloud layer, and A_k and B_k coefficients (defined in Section 2.1) for each bin as input data.

The results are summarized in *Table 3*. The first column gives the number concentrations, the second, third, and fourth ones give the difference between the intensities calculated by bin and bulk schemes at different liquid water contents.

Table 3. Difference of the radiation intensity (bin-bulk) at different number of concentration and *LWC* in the case of 100-m-thick cloudy layer, water vapor and CO_2 is not included

	$LWC_1=10^{-3}$ kg m^{-3}	$LWC_2=10^{-4}$ kg m^{-3}	$LWC_3=10^{-5}$ kg m^{-3}
N_i (*E+06) 1/m^3	r_{eff} (*10^{-6}) m	r_{eff} (*10^{-6}) m	r_{eff} (*10^{-6}) m
1000	10.70	10.28	–
250	11.35	10.83	–
100	11.77	11.18	4.37
50	12.07	11.35	4.17

The data in *Table 3* show that the application of bin scheme results in about 11 Wm–2 larger outgoing energy in a second at the top of a 100-m-thick cloud when the amount of liquid water content is about 10^{-4} kg m^{-3}, and no significant increase between the differences can be observed if the liquid water content was increased by one order. In the case of $LWC_3 = 10^{-5}$ kg m^{-3}, the difference is about a factor of 2. This decrease of difference between the outgoing radiations corresponds with results of pervious Section. This shows that although the relative difference between the extinction coefficients calculated by different schemes depends mostly on the effective radius, the difference between the calculated intensities of radiation depends on the absolute value of the extinction coefficient, which is higher in the case of higher LWC values. It also stems from data in *Table 3* that the extinction becomes saturated in the clouds with increasing *LWC*. This is the reason why there is no further significant change in the difference of the calculated intensities as the liquid water content increases from 10^{-4} kg m^{-3} to 10^{-3} kg m^{-3}.

The differences between the two schemes at the cloud top in each band have been plotted in *Figs. 3* and *4* for the four cases presented in *Figs. 1* and *2*. It can be seen that the majority of the differences appears in the bands of 1–12, which corresponds with the wavelengths interval of 3.3–14.3 μm. It means that the main difference comes from this wavelengths band, as already stated in Section 3.1. The highest difference for all cases is in band 6. The peak of the Planck function at T=293 K is at 9.88 μm (band 10 of RRTM), so the wavelengths band with the maximum change between the two schemes is not correlated with the maximum of the Planck function. It can be due to the different methods that the bulk scheme and the bin scheme uses for calculating averaged extinction coefficients for the wavelengths bands.

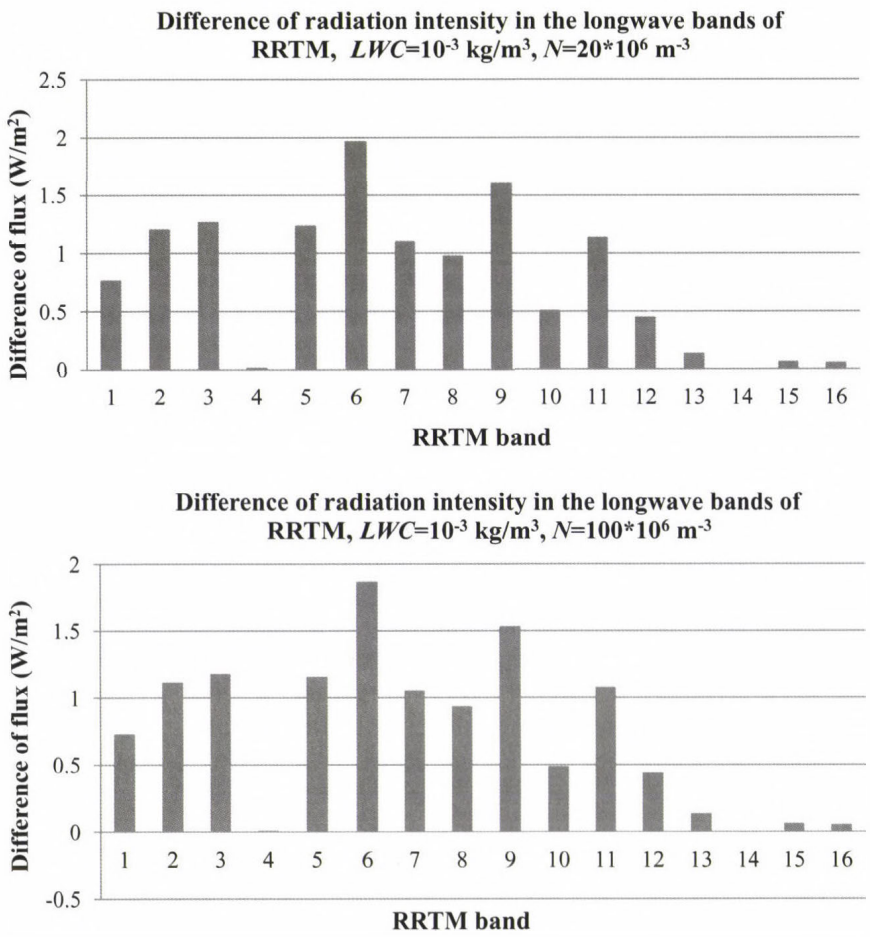

Fig. 3. Differences between the two schemes (bin-bulk) at different bands. $LWC=10^{-3}$ kgm^{-3}, the values of N are given at the top of the figures.

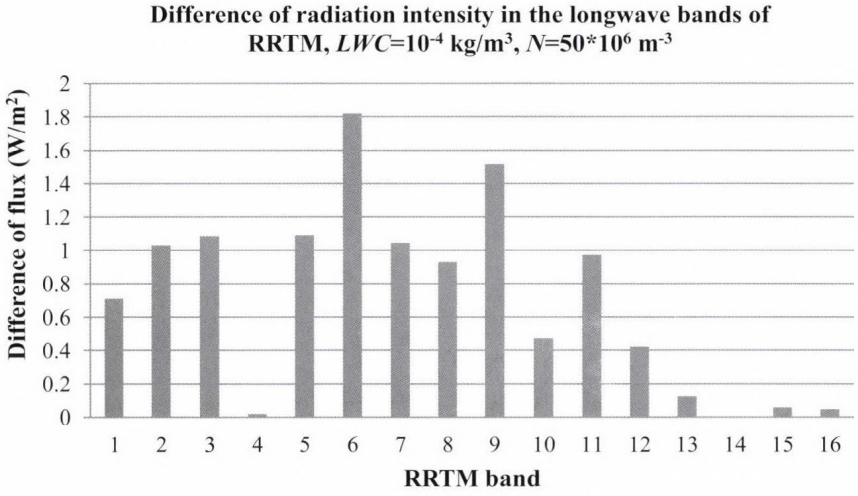

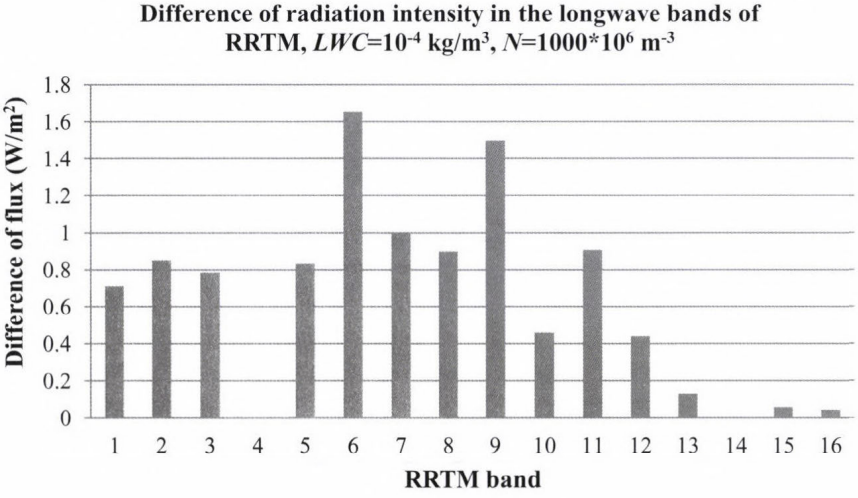

Fig. 4. Differences between the two schemes (bin-bulk) at different bands. $LWC=10^{-4}$ kg/m^3, the values of N are given at the top of the figures.

Control calculations show that presence of vapor and CO_2 reduces the difference between the schemes by a factor of two. The largest difference was found to be 6.11 W m^{-2} at $N = 20 \cdot m^{-3}$ and $LWC = 10^{-3}$ kg m^{-3}. In the presence of vapor and CO_2, no significant difference is shown in channels 1–4, difference is significant in channels 5–9 where the Planck energy is relatively high.

3.3. Results of the application of bin scheme in RRTM model

In this section the results about the upward and downward radiation profiles are presented. The atmospheric radiation profiles with the RRTM model for four different clouds were calculated. The thickness of the clouds, the number concentration of cloud droplets, and the liquid water content in the clouds are summarized in *Table 4*. In the case of fog the base was at the surface, and *LWC* was constant. In the case of the cloud the cloud base was at 400 m, and the *LWC* linearly increased until 625 m (where $LWC = 5 \cdot 10^{-4}$ kg m^{-3}), and above this height it linearly decreased. The size distribution of the water drops was given by Eq. (10) in both schemes.

Table 4. The summary of the investigated cases. * indicates mean value in the cloud layer.

Abbr.	Thickness (m)	N (*10^6 1/m^3)	LWC (10^{-3} kg m^{-3})
fog50	100	50	1
fog100	100	100	1
cloud100	300	100	2.5
cloud500	300	500	2.5

The water vapor and temperature profiles used for the calculation are plotted in *Figs. 5 and 6*. The temperature gradient was 0.976 K/m below the cloud, and it was 0.7 K/m above the fog and the cloud, and the temperature was constant above 12 km. In the cloud wet adiabatic temperature profile was supposed. The water vapor mixing ratio was equal to the saturation values within the clouds, and it decreased linearly above the cloud (and the fog) top until the height of 9 km, where it became equal to zero.

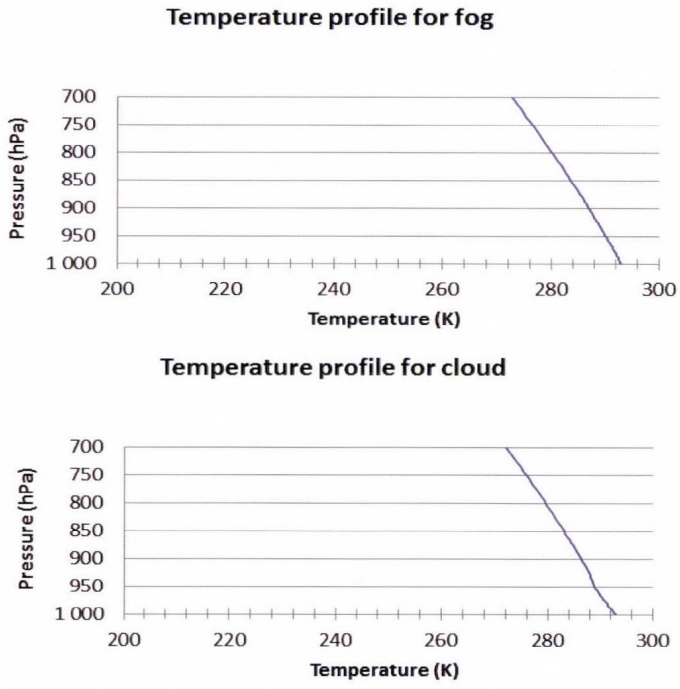

Fig. 5. Temperature profiles for the cloud and fog cases.

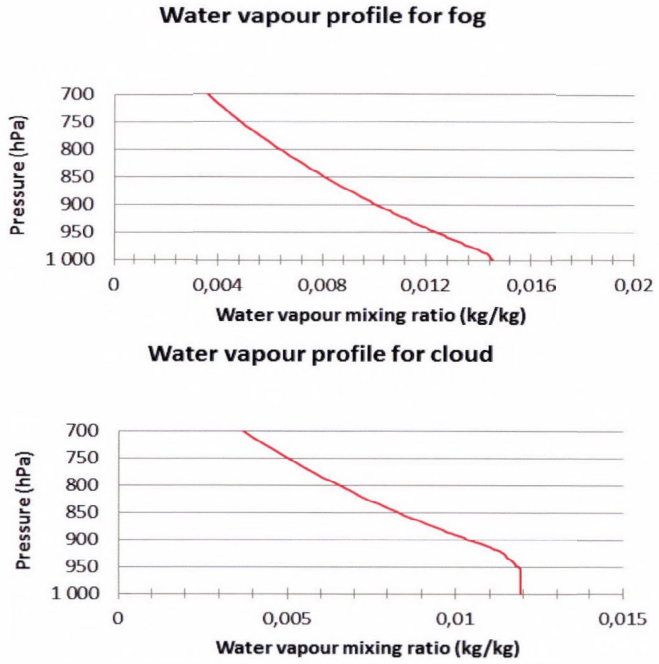

Fig. 6. Water vapor profiles for the cloud and fog cases.

The results of the RRTM calculations are shown in *Figs. 7–10.* While the upward radiation profiles were hardly affected by modification of scheme, the downward profiles were more significantly sensitive on the applied scheme. In the case of the fog, the difference between the intensity of the downward radiations at the surface is about 20 Wm^{-2}. In the case of the cloud, similar difference can be observed at about 100 m below of the cloud top. More absorption is observed in the case of the bin scheme (when absorption is closer to 1, the net flux is closer to 0). Comparison of fog50 and fog100 cases shows that the difference between the two schemes is hardly affected by the number concentration of the water droplets.

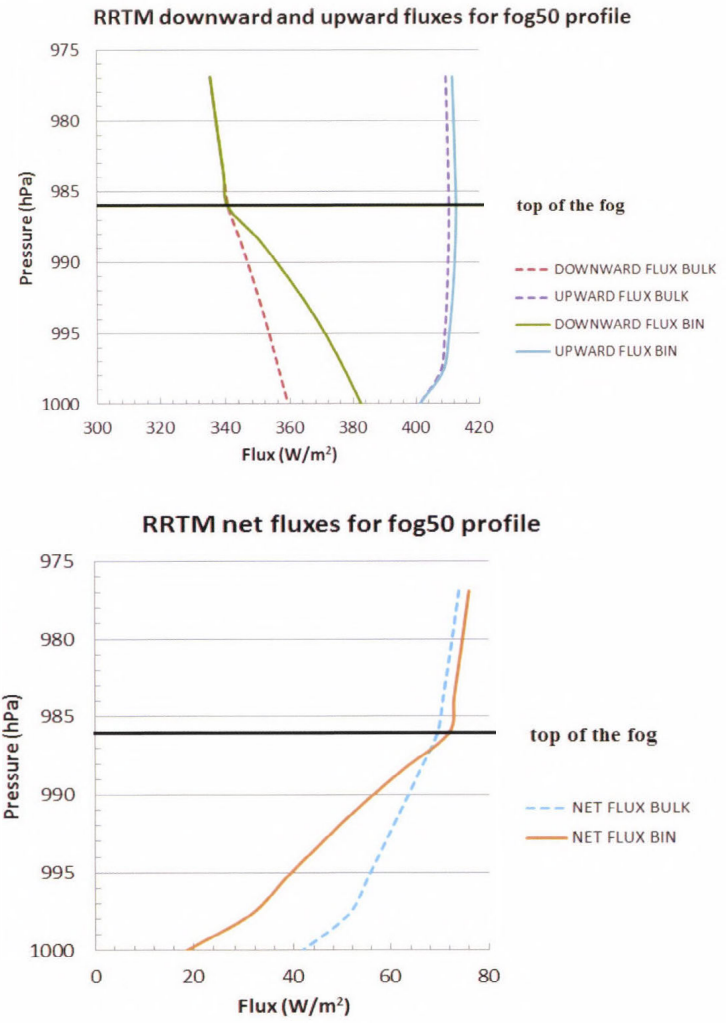

Fig. 7. Upward, downward, and net radiation flux profiles in fog50.

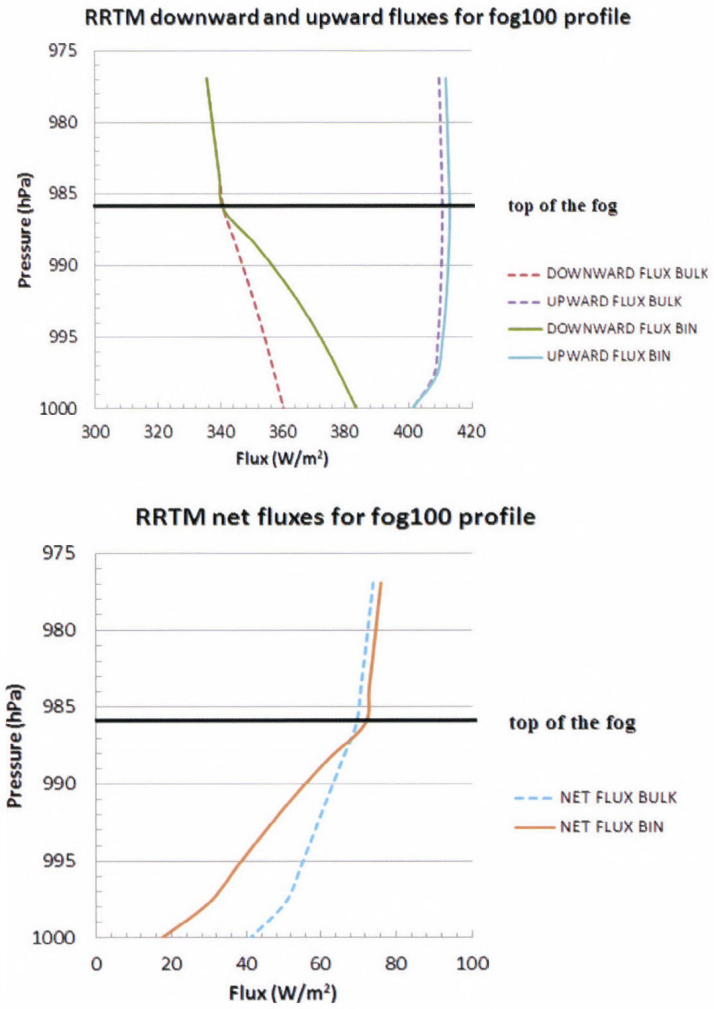

Fig. 8. Upward, downward, and net radiation flux profiles in fog100.

It can be also noted in *Figs. 9* and *10* that the absorption of the downward radiation is more intense in case of the bin scheme than in the bulk scheme. In the cloud layer the net radiation (the difference between the downward and upward radiation) is close to zero in the case of the bin scheme and slightly larger than zero in the case of bulk scheme. This means that the absorption within the cloud is almost 1. Considering the net fluxes, the maximum difference between the two profiles is around 30 Wm^{-2} in case of clouds and 20 Wm^{-2} in the case of the fog. As the gradient of the net flux is different within the cloud layer, the heating/cooling rate is larger in case of the bin scheme, because the flux is changing more sharply. Thus, difference between the schemes can impact both the cloud dynamics and cloud microphysics.

The different schemes give significantly different gradients of the net radiation in both cloud100 and cloud500 cases. The difference between the schemes is more significant in the case of cloud500, both at the cloud base and at the cloud top. So it can be concluded that the number of concentration of the droplets affect the gradient of the net fluxes, and subsequently the cooling rate at the cloud edges. The maximum cooling rate at the top of the layer in case of fog50 was 34.5 K/day in the bin scheme; whereas in the bulk scheme, it was only 12.9 K/day.

It can be seen from *Figs. 9* and *10* that if the cloud layer is thinner (100 m in case of the fog), the difference in the net outgoing radiation between the two schemes is much higher than in case of the 300-m-thick cloud.

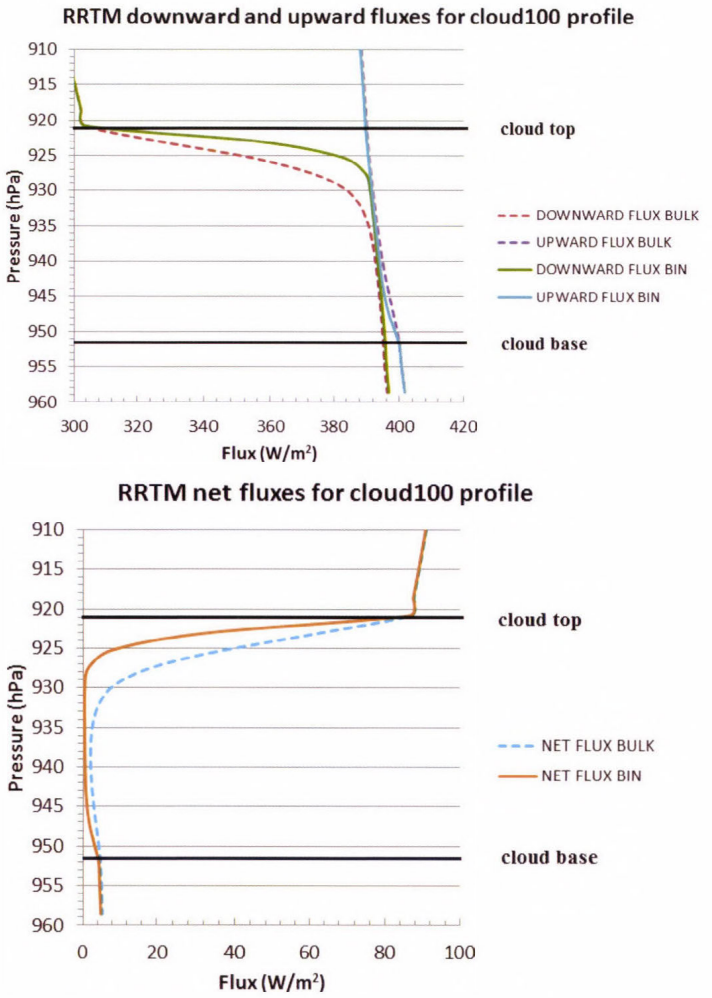

Fig. 9. Upward, downward, and net radiation flux profiles in cloud100.

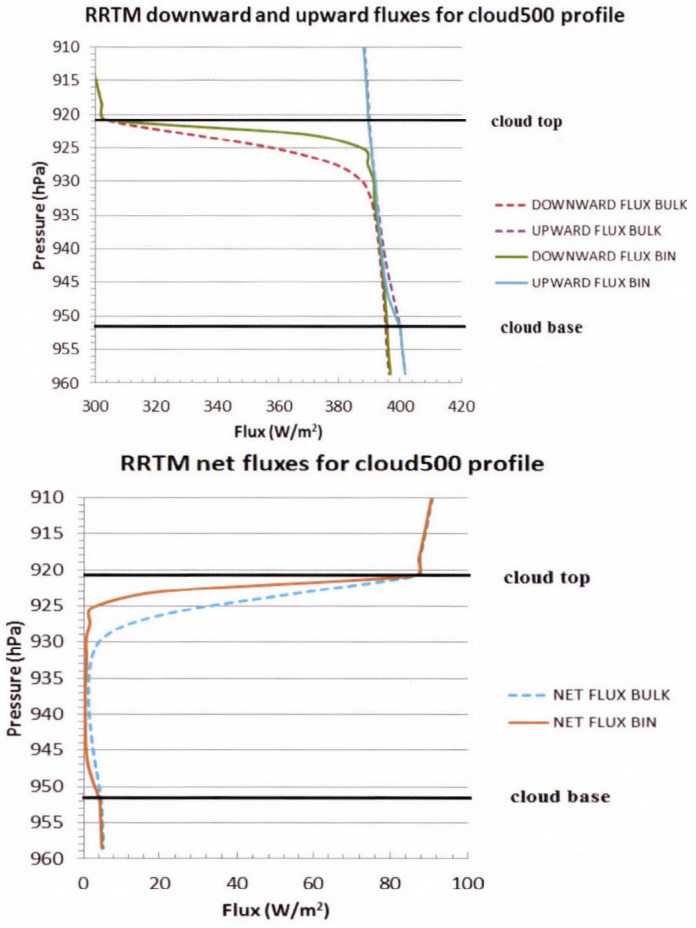

Fig. 10. Upward, downward, and net radiation flux profiles in cloud500.

4. Conclusion

Cloud-radiation interactions are essential to be understood and modeled correctly. The evolving radiation profile affects temperature and microphysical processes in micro-scale, and atmospheric motions in larger scales. Weather events and climatic patterns strongly depend on the radiation budget. More accurate description of cloud optical properties can significantly improve numerical weather forecasts.

In this study it was investigated how evaluation of the extinction coefficients affects longwave radiation budget, and longwave heating/cooling rates in the atmosphere. A new bin radiation scheme was developed, and the results of bin scheme were compared to that of a currently applied bulk scheme, which is widely used in operational numerical weather prediction models.

The results are summarized in the following points:

(1) The extinction coefficient calculated by the bin scheme was generally smaller than that calculated by the bulk scheme. The difference between the extinction coefficients calculated by the two different ways depends on the effective radius and the wavelength. The two curves fit well in the whole spectrum if the effective radius is higher than 10 μm, and the wavelength is less than about 8.0 μm. In the case of the smaller effective radius, or higher wavelengths, significant difference was found in the wavelength interval of 5–20 μm (around 10%), and even higher at the wavelengths of 9.6 μm for all effective radii.

(2) The variations of the extinction coefficients in the bin scheme are smoother than in the bulk scheme, due to the fact that the bin scheme represents a broad size of droplet spectra, compared to the bulk scheme which is represented by a single effective radius.

(3) The two different methods for the calculation of the extinction coefficients result in an increase of about 10 Wm^{-2} in the outgoing longwave radiation in case of a 100-m-thick cloud layer when the effect of the water vapor and CO_2 is not taken into account. The change in the intensity was two times smaller if the *LWC* was reduced to 10^{-5} $kg\,m^{-3}$within the cloud. The main difference comes from the wavelengths bands below 14 μm, where the majority of the Planck energy is. The presence of the vapor reduces the difference between the two schemes.

(4) The number of concentration in the cloudy layer does not affect considerably the resulting difference between the outgoing radiations calculated by the two schemes. However, the value of *LWC* and the cloud thickness have larger impact: the lower the *LWC*, and the higher the cloud thickness is, the smaller the difference between the two schemes.

(5) Large uncertainty of net radiation at surface can result in significant error in the forecast of the surface temperature. Supposing steady state conditions, the difference of 20 Wm^{-2} can results in about 3 C differences in surface temperature after 6 hours.

(6) Large difference (30 Wm^{-2}) between the two schemes was found within the simulated cloud layer near to the cloud tops. 20 Wm^{-2} difference between the net longwave radiations was found at the surface in case of fog.

(7) The bin scheme produced profiles with higher gradient at the edges of the cloud layer, which results in higher cooling rate as well both at the cloud top and cloud base. In the case of the bulk scheme, temperature hardly changes at the cloud base, which results in negligible warming. The consequence of different temperature profiles given by the two schemes can be significantly different cloud microphysics and cloud dynamics.

At the next phase of the research, the RRTM model will be coupled with a two-dimensional cloud model. The model uses bin microphysics, which allows us to give an appropriate input for the recently developed bin radiation scheme.

References

Arking, A., 1991: The Radiative Effects of Clouds and their Impact on Climate. *B. Am. Meteorol. Soc. 72*, 795–953.

Buriez, J.C., Bonnel, B., Fouquart, Y., Geleyn, J.F., and *Morcrette, J.J.,* 1988: Comparison of model-generated and satellite- derived cloud cover and radiation budget. *J. Geophys. Res. 93*, 3705–3719.

Chen, T., Rossow, and *W.B., Zhang, Y.*, 2000: Radiative Effects of Cloud-Type Variations. *J. Climate, 13*, 264–286.

Chen, T., and *Rossow, W.B.*, 2002: Determination of top-of-atmosphere longwave radiative fluxes: A comparison between two approaches using ScaRaB data. *J. Geophys. Res., 107(D8)*. ACL 6-1–ACL 6-13.

Cough, S.A., Iacono, M.J., and *Moncet, J.L.,* 1992: .Line-by-line calculations of atmospheric fluxes and cooling rates: Application to water vapor. *J. Geophys. Res. 97*, 15761–15785.

Clough, S.A., Shephard, M.W., Mlawer, E.J., Delamere, J.S., Iacono, M.J., Cady-Pereira, K., Boukabara, S., and Brown, P.D., 2005: Atmospheric radiative transfer modeling: a summary of the AER codes, Short Communication. *J. Quant. Spectrosc. RA 91*, 233–244.

Corti, T. and *Peter, T.*, 2009: A simple model for cloud radiative forcing. *Atmos. Chem. Phys. Discuss. 9*, 8541–8560.

Ebert, E.E. and *Curry, J.A.*, 1992: A parameterization of ice cloud optical properties for climate models. *J. Geophys. Res. 97(D4),* 3831–3836.

Fouquart, Y., Buriez, J.C., Herman, M., and *Kandel, R.S.*, 1990: The Influence of Clouds on Radiation: A Climate-Modeling Perspective. *Rev. Geophys. 28*, 145–166.

Fu, Q., Ping, Y., and *Sun, W.B.*, 1998: An Accurate Parameterization of the Infrared Radiative Properties of Cirrus Clouds for Climate Models. *J. Climate 11*, 2223–2237.

Geresdi, I., 1998: Idealized simulation of the Colorado hailstorm case: comparison of bulk and detailed microphysics. *Atmos. Res. 45,* 237–252.

Gettelman, A., Morrison, H., and *Ghan, S.J.,* 2008: A New Two-Moment Bulk Stratiform Cloud Microphysics Scheme in the Community Atmosphere Model, Version 3 (CAM3). Part II: Single-Column and Global Results. *J. Climate 21*, 3660–3679.

Harrington, J.Y., 1997: The Effects of Radiative and Microphysical Processes on Simulated Warm and Transition Season Arctic Stratus. Ph.D. Thesis, Colorado State University, Ft. Collins, CO. 298.

Harrington, J.Y., Feingold, G., and *Cotton, W.R.*, 2000: Radiative Impacts on the Growth of a Population of Drops within Simulated Summertime Arctic Stratus. *J. Atmos. Sci. 57*, 766–785.

Harrington, J. and *Olsson, P.Q.*, 2001: A method for the parameterization of cloud optical properties in bulk and bin microphysical models. Implications for arctic cloudy boundary layers. *Atmos. Res. 57,* 51–80.

Hong, G., Yang, P., Baum, B.A., Heymsfield, A.J., and *Xu, K-M.,* 2009: Parameterization of Shortwave and Longwave Radiative Properties of Ice Clouds for Use in Climate Models. *J. Climate 22*, 6287–6312.

Hongqi W. and *Gaoxiang, Z.,* 2002: Parameterization of longwave optical properties for water clouds. *Adv. Atmos. Sci. 19*, 25–34.

Hu, Y. X. and *Stamnes, K.*, 1993: An accurate parameterization of the radiative properties of water clouds suitable for use in climate models. *J. Climate 6*, 728–742.

Kunkel, B.A., 1984: Parameterization of Droplet Terminal Velocity and Extinction Coefficient in Fog Models. *J. Climate Appl. Meteorol. 23*, 34–41.

Lindner, T.H. and *Li, J.*, 2000: Parameterization of the Optical Properties for Water Clouds in the *Infrared J. Climate 13*, 1797–1805.

Liu, M., Nachamkin, J.E., and *Westphal, D.L.*, 2009: On the Improvement of COAMPS Weather Forecasts Using an Advanced Radiative Transfer Model. *Wea. Forecast 24*, 286–306.

Lynn, B.H., Khain, A.P., Dudhia, Rosenfeld, D.J., Pokrovsky, A., and *Seifert, A.*, 2005: Spectral (Bin) Microphysics Coupled with a Mesoscale Model (MM5). Part I: Model Description and First Results. *Mon. Weather Rev. 133*, 44–58.

Lynn, B. and *Khain, A.*, 2007: Utilization of spectral bin microphysics and bulk parameterization schemes to simulate the cloud structure and precipitation in a mesoscale rain event. *J. Geophys. Res. 112*, D22205.

Mitchell, D.L., 2000. Parameterization of the Mie extinction and absorption coefficients for water clouds. *J. Atmos. Sci. 57*, 1311–1326.

Mlawer, E.J., Taubman, S.J., and *Clough, S.A.*, 1995: RRTM: A Rapid Radiative Transfer Model, Fifth Atmospheric Radiation Measurement (ARM) Science Team Meeting http://www.arm.gov/publications/proceedings/conf05/extended_abs/mlawer_ej.pdf

Mlawer, E.J., Taubman, S.J., Brown, P.D., Iacono, M.J., and *Clough, S.A.*, 1997: Radiative transfer for inhomogeneous atmospheres: RRTM, a validated correlated-k model for the longwave, *J. Geophys. Res. 102(D14)*, 16663–16682.

Oreopoulos, and *L., Rossow, W.*, 2011: The cloud radiative effects of International Satellite Cloud Climatology Project weather states. *J. Geophys. Res. 116(D12202).*

Petters, J.L., Harrington, J.Y., and *Clothiaux, E.E.*, 2012: Radiative–Dynamical Feedbacks in Low Liquid Water Path Stratiform Clouds. *J. Atmos. Sci. 69*, 1498–1512.

Ramaswamy, V., Boucher, O., Haigh, J., Hauglustine, D., Haywood, J., Myhre, G., and *Solomon, S.*, 2001: Radiative forcing of climate. In *Climate Change 2001: The Scientific Basis. Contribution of Working Group I to the Third Assessment Report of the Intergovernmental Panel on Climate Change*. Cambridge, U.K.: Cambridge University Press, 349–416.

*Ramanathan, V., Cess, R.D., Harrison, E.F., Minnis, P., Barkstrom, B.R., Ahmad, E.,*and *Hartmann, D.*, 1989: Cloud-Radiative Forcing and Climate: Results from the Earth Radiation Budget Experiment. *Science, New Series 243*, 4887, 57–63.

Ramanathan, V., Inamdar, A., 2006: The radiative forcing due to clouds and water vapor. Cambridge University Press.

Rasmussen, R.M., Geresdi, I., Thompson, G., Manning, K., Karplus, E., 2002: Freezing Drizzle Formation in Stably Stratified Layer Clouds: The Role of Radiative Cooling of Cloud Droplets, Cloud Condensation Nuclei, and Ice Initiation. *J. Atmos. Sci. 59*, 837–860.

Ritter, B., Geleyn, J.F., 1992: A Comprehensive Radiation Scheme for Numerical Weather Prediction Models with Potential Applications in Climate Simulations, *Mon. Wea. Rev. 120*, 303–325.

Roach, W.T., Slingo, A., 1979: A high resolution infrared radiative transfer scheme to study the interaction of radiation with cloud, *Q..J.Roy.Meteor.Soc. 105*, 603–614.

Rossow, W. B., Duenas, E.N., 2004: The international satellite cloud climatology project (ISCCP) web site: An online resource for research. *Bull. Amer. Meteor. Soc. 85*, 167–172.

Slingo, A., Schrecker, H.M., 1982. On the shortwave properties of stratiform water clouds. *Q. J. Roy. Meteorol. Soc. 108*, 407–426.

Stephens, G.L. 1984: The parameterization of radiation for numerical weather prediction and climate models, *Mon. Wea. Rev. 112*, 826-867.

Stephens, G.L., Tsay, S-C., Stackhouse, P.W., Flatau, P.J., 1990: The Relevance of the Microphysical and Radiative Properties of Cirrus Clouds to Climate and Climatic Feedback. *J. Atmos. Sci. 47*, 1742–1754.

Stephens, G.L., 2004: Cloud Feedbacks in the Climate System: A Critical Review. *Climate 18*, 237–273.

Straka, J.M., Kanak, K.M., and *Gilmore, M.S.*, 2007: The behavior o f number concentration tendencies for the continuous collection growth equation using one- and two-moment bulk parameterization schemes. *J. Appl. Meteorol. Climatol. 46*, 1264–1274.

Tompkins, A.M. and *Di Giuseppe, F.*, 2009: Cloud radiative interactions and their uncertainty in climate models, in P. Williams and T. Palmer, eds., Stochastic Physics and Climate Models, *Cambridge University Press, UK*

Tzivion, S., Feingold, G. Levin, Z., 1987: An efficient numerical solution to stochastic collection eqation, *J. Atmos. Sci. 44*, 3139–3149.

Walko, R.L., Cotton, W.R., Meyers, M.P., Harrington, J.Y., 1995: New RAMS cloud microphysics parameterization: Part I. The single moment scheme. *Atmos. Res.* 38, 29–62.

Wielicki, B.A., Barkstrom, B.R., Harrison, E.F., Lee, R.B., Smith, G.L., and *Cooper, J.E.,* 1996: Clouds and the earth's radiant energy system (CERES): An earth observing system experiment. *B. Am. Meteorol. Soc. 77*, 853–868.

Appendix A

Q_{ext} depends on the droplet diameter (D), wavelength (λ), and index of refraction (m), with the imaginary component n_i and real component n_r:

$$Q_{ext}(D,\lambda,m)=2K(tD), \tag{A1}$$

where $t=\frac{2\pi}{\lambda}[n_i+i(n_r-1)]$, $m=n_r-i\times n_i$, and $K(x)=1+2\mathrm{Re}[\frac{e^{-x}}{x}+\frac{e^{-x}-1}{x^2}]$.

The correction parameter C_{res} is a rather complicated function of the drop size and the refraction index:

$$C_{res}=r_a\frac{k^m e^{-\varepsilon k}}{k_{max}^m e^{-m}}, \tag{A2}$$

where

$$r_a=0.7393n_r-0.6069, \tag{A3}$$

and

$$m=\frac{1}{2},\quad k=\frac{D}{\lambda},\quad k_{max}=\frac{m}{\varepsilon},\text{ and }\quad \varepsilon=\frac{1}{4}+0.6\{1-\exp[-\frac{8\pi n_i}{3}]\}^2. \tag{A4}$$

The Q_{edge} term in Eq.(1) is given by:

$$Q_{edge}=2(\pi k)^{-2/3}[1-\exp(-0.06\pi k)]. \tag{A5}$$

After substituting Eqs. (A1)–(A5) into Eq. (1) or Eq. (7), we can evaluate the extinction efficiency as a function of droplet diameter, wavelength, and refraction index (which is the $Q_{ext}(D,\lambda,m)$ function in explicit form).

Appendix B

Using the MADT method Eq. (8), the integral in Eq. (7) can be divided in three parts:

$$\beta_{ext,i}=\sum_{j=1}^{16}\sum_{k=2}^{N_{bins}}\left[\int_{\Delta\lambda_j}\left(E_\lambda\int_{M_{k-1}}^{M_k}A(D)Q_{ext,i}(D,m,\lambda)n_k(M)dM\,d\lambda\right)/\int_{\Delta\lambda_j}E_\lambda d\lambda\right], \quad \text{(B1)}$$

where

$$Q_{ext,1}(D,\lambda,m)=Q_{ext}, \quad Q_{ext,2}(D,\lambda,m)=\frac{C_{res}}{2}\times Q_{ext}, \text{ and } Q_{ext,3}(D,\lambda,m)=Q_{edge},$$

and j is the number of band in *Table 1*. Using the appropriate equations from the Appendix A, the above integral can be written as the sum of the next three equations. After substitution of Eq. (6) in (B1), the integrals can be evaluated analytically.

$$\beta_{ext,1}=\sum_{j=1}^{16}\sum_{k=2}^{N_{bins}}\left[\int_{\Delta\lambda_j}\left(E_\lambda\int_{M_{k-1}}^{M_k}\left(\frac{\Pi}{4}\times D^2\left(1+2\mathrm{Re}\left[\frac{e^{-tD}}{tD}+\frac{e^{-tD}-1}{t^2D^2}\right]\right)(A_k+M\times B_k)dM\,d\lambda\right)/\int_{\Delta\lambda_j}E_\lambda d\lambda\right]=$$

$$=\sum_{k=2}^{N_{bins}}A_k\times\sum_{j=1}^{16}K_{A1kj}(M_{k-1},M_k,\Delta\lambda_j)+\sum_{k=2}^{N_{bins}}B_k\times\sum_{j=1}^{16}K_{B1kj}(M_{k-1},M_k,\Delta\lambda_j)$$

$$\beta_{ext,2}=\sum_{j=1}^{16}\sum_{k=2}^{N_{bins}}\left[\int_{\Delta\lambda_j}\left(E_\lambda\int_{M_{k-1}}^{M_k}\left(\frac{\Pi}{4}\times D^2\left(1+2\mathrm{Re}\left[\frac{e^{-tD}}{tD}+\frac{e^{-tD}-1}{t^2D^2}\right]\right)\times\frac{C_{res}}{2}\times(A_k+M\times B_k)dM\,d\lambda\right)/\int_{\Delta\lambda_j}E_\lambda d\lambda\right]=$$

$$=\sum_{k=2}^{N_{bins}}A_k\times\sum_{j=1}^{16}K_{A2kj}(M_{k-1},M_k,\Delta\lambda_j)+\sum_{k=2}^{N_{bins}}B_k\times\sum_{j=1}^{16}K_{B2kj}(M_{k-1},M_k,\Delta\lambda_j)$$

$$\beta_{ext,3}=\sum_{j=1}^{16}\sum_{k=2}^{N_{bins}}\left[\int_{\Delta\lambda_j}\left(E_\lambda\int_{M_{k-1}}^{M_k}\left(\frac{\Pi}{4}\times D^2\times 2\left(\pi\frac{D}{\lambda}\right)^{-\frac{2}{3}}\left[1-e^{-0.06\pi\frac{D}{\lambda}}\right](A_k+M\times B_k)dM\,d\lambda\right)/\int_{\Delta\lambda_j}E_\lambda d\lambda\right]=$$

$$=\sum_{k=2}^{N_{bins}}A_k\times\sum_{j=1}^{16}K_{A3kj}(M_{k-1},M_k,\Delta\lambda_j)+\sum_{k=2}^{N_{bins}}B_k\times\sum_{j=1}^{16}K_{B3kj}(M_{k-1},M_k,\Delta\lambda_j)$$

The final K_{Akj} and K_{Bkj} kernels are the sum of the K_{ikj} constants in the three parts (i=1,2,3).

IDŐJÁRÁS

Quarterly Journal of the Hungarian Meteorological Service
Vol. 117, No. 4, October–December, 2013, pp. 403–433

High resolution solar spectrophotometry and narrow spectral range solar radiation measurements at the Hungarian Meteorological Service

Zoltán Tóth

Atmospheric Physics and Measurement Technics Division
Hungarian Meteorological Service
P.O.Box 39, H-1675 Budapest, Hungary

(Manuscript received in final form June 17, 2013)

Abstract— Aims of the spectral radiation measurements can be devided to two wider areas: one is to get information about the radiation source, and the other is to get information about the properties of the space between the radiation source and the detector if output signal from the radiation source is known. In the latter case either the optical properties of the certain space or some optical parameter of an object placed in there is to be studied. The sun can be the object of the study or it can be used as natural radiation source to investigate some important properties of the atmosphere. The term 'solar spectrophotometry' refers to this.

Although detection of spectral distribution of the solar radiation is considered a special area that is relatively rarely used even today in atmospheric physical measurements, it still has big significance. In addition to the 'mere' knowledge of spectal solar irradiance, the measured data can be used in a considerably wide range. In special cases, the narrow spectral range informations about the radiation can be very useful. Typical example is the erythemally weighted UV radiation. Though it does not give spectral information, the spectral range that is characterized by it, is considerably narrower than that of the classical radiation components. So this type of measurements is also discussed here.

Main applied physical and technical principles of solar spectrophotometry, as well as spectrophotometers working in the UV, visible, and near infrared spectral range used at the Hungarian Meteorological Service (HMS), are shown in this paper. Measurement results and results from studies and researches using these data are also shown and analyzed. Also some special studies performed occasionally are shown.

Today the primary base for operation of high accuracy measurement systems is the calibration. Since we have reference instruments, QA/QC procedures are of crucial importance in our measuring practice. Our activitiy as we operate WMO Regional Center for Solar Radiation in Region VI gives even bigger emphasis to that.

Key-words: solar radiation, measurement technics, spectrophotometry, optical depth, total ozone, UV radiation, calibration

1. Introduction

Solar radiation measurements in a station mean, in most cases of solar radiation practice of meterorological observations, the measurement of components of classical radiation budget of the atmosphere. Use of narrow spectral range or high resolution spectral solar radiation measurements can be considered relatively rare even today, despite the fact that it is not a brand new technique. The main reason is that it requires suitable special expertancy and special, rather expensive equipments that cannot be provided easily by institutions.

Narrow range and high resolution measurements of solar radiation have started at the Hungarian Meteorological Service (HMS) in the early nineties of the previous century by installation of ultraviolet detectors measuring erythemally weighted UV radiation and continued with installation of two high resolution spectrophotometers, then later by sunphotometers. It is important to note that primary acitvity of the HMS is to operate monitoring networks and establishing quality controlled databases. Consequently, the studies or researches concern different processing of data and analysis of processed data mostly and, only in a few case, some other 'more scientific' job in area of solar radiation measurements also.

The operation, and physical and technical background of the aforementioned systems, as well as some results from studies and researches based on their data are also shown in this paper. To detailedly describe the operation and technical background cannot be object of this paper, so they are concerned very briefly only.

2. Background physics

The background physics is not discussed in details because it can be found in numerous books and articles concerning theoretical and applied physics. The basic physics is the theoretical and experimental approaches of radiative transfer that can be performed in many ways depending on the type of the problem to be solved. It is, by all means, to be noted that the basic terms and definitions concern monochromatic radiation. It is, however, to be stressed that when monochromatic flux is mentioned in measurement technics, it means a flux belonging to very narrow, but finite range, because finite quantity cannot belong to a zero interval in reality. So the monochromatic quantities are only quasi-monochromatic ones, actually. Consequently, if the wavelength of a spectral irradiance is given, the irradiance refers to a spectral band whose center is at the wavelength in question. Mathematically it can be expressed as follows:

$$I_{\lambda}^{q} = \int_{\lambda-d\lambda}^{\lambda+d\lambda} I_{\lambda} d\lambda \ , \tag{1}$$

where

I_{λ}^{q} is the quasi-monochromatic flux,

I_{λ} is the theoretical monochromatic flux,

λ is the wavelength of the center of the spectral band,

$\Delta\lambda$ is the half-width of the spectral band.

The narrower the band, the more accurate the flux referring to the given wavelength.

If the aim of the measurement is to get information about the space or, in atmospheric physics practically, a medium, or any component in the atmosphere, also the spectral flux at the top of the atmosphere (the so-called extraterrestrial flux) should be known. Considering the extraterrestrial flux and the flux measured at the surface, the total amount of a given component can be determined, obviously in the case when values of other physical quantities are known from measurement or calculation.

2.1. Determination of total columnar amount of atmospheric gaseous components

The calculation methods are well and fully described in several books and guide-books, so they are mentioned here very briefly, and also some special physical quantities or methods are explained in more details. Determination of gaseous components using solar spectrophotometry is performed by the method of relative intensities (*Dobson,* 1957). The main principle is described here very briefly only, without quantification. This main principle is that the irradiance is measured at several wavelength pairs so that one of the pairs is at a wavelength where the absorption coefficient of the gas is considerably high and the other one is at a wavelength where the absorption coefficient is as low as it can be taken as zero. An important criterium is that the two wavelengths have to be very close to each other, so a spectral interval is needed where the absorption coefficient varies by high rate. The reason is that the properties of the aerosol being present in the atmospheric column between the solar disc and the detector at the time of the observation is not known. It is well-known, however, that the variation of the aerosol optical depth with wavelength can be described in each case by a smooth and non-rapidly changing function. Consequently, its effect on the calculated value of optical depth of the gaseous component, whose total columnar amount is to be determined, can be neglected (it means mathematically that the aerosol optical depth, as variable, is eliminated from the equation).

2.2. Determination of aerosol optical depth

Calculation of aerosol optical depth (AOD) is also a well-known standard method and described in several publications (*Alföldy et al.,* 2007), so the reduction of the formula by which it is calculated is not shown here. The AOD is calculated by the equation as follows:

$$\delta_{A\lambda} = \frac{1}{M} ln \frac{I_{0\lambda}}{I_\lambda S} \left(\frac{P}{P_0} \delta_{R\lambda} + \delta_{O\lambda} \right), \tag{2}$$

where:

$\delta_{A\lambda}$ is the aerosol optical depth at wavelength λ;

$I_{0\lambda}$ is the extraterrestrial irradiance;

I_λ is the irradiance at the observational point;

S is the correction factor for the Earth-Sun distance (ratio of Earth-Sun distance at the time of the measurement to the mean value);

M is the relative optical airmass;

$\delta_{R\lambda}$ is the optical depth of Rayleigh scattering from atmospheric molecules;

$\delta_{O\lambda}$ is the optical depth of ozone absorption: $\delta_{O\lambda} = \alpha_{O\lambda} \eta$;
where $\alpha_{O\lambda}$ is the ozone absorption coefficient and η is the total ozone content of the air column between the solar disc and the detector;

P, P_0 are the surface pressure and at the time of the observation and standard sea level pressures.

To obtain $\delta_{A\lambda}$, value of I_λ is measured by solar spectrophotometer and P is known by measurement also. Total ozone content η either can be observed at the given site or known from satellite observations. Values of both $I_{0\lambda}$ and S are known.

Since high accuracy spectrophotometric total ozone content data are available at the Marczell György Main Observatory, accurate estimation of AOD is possible to perform. The standard wavelengths are used to estimate AOD are 368, 380, 412, 450, 500, 610, 675, 778, 862, and 1024 nm, and since the autocorrelation of AOD values estimated for these 10 wavelengths is very high, AOD for 500 nm is used generally for studies and in models.

2.3. Determination of graybody (broad band) optical depth

Graybody (broad band) optical depth (GBOD) can be determined if definition of monochromatic optical depth is extended to a wider spectral range if irradiances measured at the surface are available (*Németh et al.*, 1996). Consequently, the GBOD will then be determined in the following way. If $I_{\lambda 0}$ is the irradiance coming onto the top of the atmosphere at wavelength λ and I_λ is the irradiance measured at the surface by a pyrheliometer in case of relative optical air mass m, then:

$$\int_{S_{PYR}} I_\lambda d\lambda = \left(\int_{S_{PYR}} I_{\lambda 0} d\lambda \right) e^{-m\delta_{GB}}, \tag{3}$$

where δ_{GB} is the GBOD and S_{PYR} is the sensitivity range of the pyrheliometer.

Thus GBOD is given by the following equation if direct irradiance (denominator of the fractional) is measured:

$$\delta_{GB} = \frac{1}{m} ln \frac{\int_{S_{PYR}} I_{\lambda 0} d\lambda}{\int_{S_{PYR}} I_{\lambda} d\lambda}. \tag{4}$$

Though graybody optical depth is not a spectral quantity, as it is evident from its definition, results from studies concerning it are important to include here due to, on the one hand, its very close connection with spectral aerosol optical properties and on the other, its good usability to characterize short-wave radiation transmission of the atmosphere.

2.4. Ångström exponent

The Ångström exponent α characterizes the particle size distribution in the aerosol being present in the air column over the measuting site at the time of the observation. Value of α is approximetaly 1.3 for average normal size distribution. Values higher than 1.3 are resulted in by the relatively higher frequency of smaller particles as compared with the large particles having a radius greater than 0.5 μm. Values lower than 1.3 mean the relatively higher frequency of large particles (*Ångström*, 1929). α exceeds 2 considerably, or it does not reach 0.4 or 0.5 only in extreme situations.

α is determined by the following equation (*Alföldy et al.*, 2007):

$$ln \delta_{A\lambda} = ln \beta - \alpha ln \lambda, \tag{5}$$

where:

$\delta_{A\lambda}$ is the aerosol optical depth at the wavelength λ,

β is the Ångström turbidity coefficient,

α is the Ångström exponent.

This practically means that considering ln $\delta_{A\lambda}$ as a function of ln λ, α is the steepness of the curve. α can then be determined by a reasonable linear fitting in that regression.

3. *Narrow spectral range measurements*

3.1. Biologically effective UV radiaton

Due to the global ozone depletion, accurate monitoring of biologically effective UV radiation has become stressedly important in the last decades, and after the atmospheric ozone has started to recover, it has remained important due to the fact that UV irradiation is not decreasing despite the ozone increase.

If one wants to know the exact biological effect of an irradiation on a biological system, the response of the biological system in question to the irradation is needed to know. It means, practically, the spectral sensitivity of the biological system. The function describing the wavelength dependence of the sensitivity is called action spectrum and it is consequently a weighting function. The biological irradiance for a given wavelength can be obtained if the measured spectral irradiance is multiplied by the value of the action spectrum for the wavelength in question. The biological effective dose, I_{eff}, can be obtained by the following equation:

$$I_{eff} = \int_{\lambda_L}^{\lambda_U} I_\lambda A_\lambda d\lambda \ , \tag{6}$$

where

λ_L and λ_U are the lower and upper limit of the spectral range where values of the action spectrum are used,

I_λ is the irradiance at the wavelength λ,

A_λ is the value of the action spectrum for the wavelength λ.

If a high resolution spectrophotometer is available for the observations, the biologically effective radiation is determined by Eq. (6). However, there are broad band UV detectors, the so-called UV Biometers, whose output is the biologically effective dose. Spectral response of the human skin to the UV radiation is called Erythema, so the biologically effective radiation in case of human skin is called generally erythemally weighted radiation. The biophysical background of these processes is not object of this paper, so it is not discussed in details. *Fig. 1* shows the meaning of the aforementioned facts in reality. A physical spectrum (red line) and the corresponding erythemally weighted spectrum (blue line) can be seen in the figure. The spectrum is from our database of high-resolution UV spectra recorded by Brewer spectrophotometer at the Marczell György Main Observatory of HMS in Budapest. The importance of use of the response function in case when biological effect of a radiation is studied is clear based on the figure. Due to the very rapid variation of the Erythema function, the biological spectrum considerably differs from the physical one.

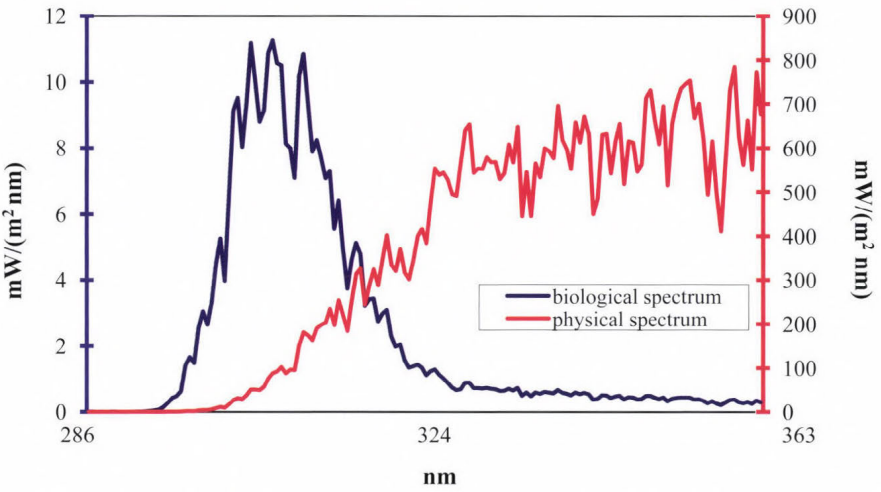

Fig. 1. Physical UV spectrum measured by Brewer MKIII spectrophotometer and the calculated corresponding erythemally weighted (biological) spectrum.

3.2. Photosynthetically Active Radiation (PAR)

PAR is a special quantity that means the biological effectiveness of visible radiation on photosynthesis of plants. Consequently, nature of PAR is the same like any other action spectrum weighted radiations, but it is expressed in a special unit.

4. Measuring equipments at the HMS

The equipments that are used for high resolution spectral measurements and special narrow range measurements at the Hungarian Meteorological Service are shown very briefly in this section. To describe their technical details and specifications, as well as principles of their operation cannot be object of this paper. Their instrument manuals include detailed informations about them (see references).

4.1. Brewer MKIII double monochrometer spectrophotometer

This instrument is a high accuracy spectrophotometer that is the most accurate and most reliable spectral equipment in the UV region today. Its sensitivity range is from 286.5 nm to 363 nm with a spectral resolution of 0.5 nm. It is equipped with a double monochrometer to increase the effectiveness of filtering of stray light that is very important due to the low irradiances to detect. A photomultiplier is used as detector to produce suitably high signal-to-noise ratio.

The equipment measures the total air columnar ozone and sulphur-dioxide content and records global UV spectrum in the range and with the parameters mentioned above (for any other details, see *Brewer MKIII Spectrophotometer Operator's Manual,* 1998).

In our operational measurement practice, it observes total ozone and sulphur-dioxide, as well as records UV spectra by approximately 15–20 minutes (the reason why the mesurement frequency varies a bit is that the observations are carried out at fixed solar zenith angles, and it, in addition to the observations in question, performs several tests concerning its optics, electronics, and mechanics to provide the possible highest quality data).

The Brewer spectrophotometer was installed in 1998, but the high accuracy total ozone observations have been started at the HMS in 1969 with the manually controlled Dobson spectrophotometer, that has been the highest quality instrument to observe total ozone then.

The two spectrophotometers worked simultaneously for one and a half year until terminating observations with Dobson spectrophotometer due to lack of manpower. These observations are carried out the Marczell György Main Obervatory in Budapest.

4.2. LI-1800 spectroradiometer / spectrophotometer

This high accuracy instrument is constructed to record electromagnetic spectra in the spectral range from 300 nm to 1100 nm with a spectral resolution of 1 nm. The diffraction spectra are produced by a monochrometer. The instrument is basically designed as spectroradiometer, namely to measure global (full-sky) irradiance, but, by using a suitably designed pipe with diaphragms, it has been made to be suitable to measure direct irradiance. It can thus work as both spectroradiometer and spectrophotometer.

In our operational measurement practice, LI-1800 records spectra by 15 minutes or 30 minutes normally according to the schedule set by us. Measurements are carried out only in cases when solar disc is not covered by cloud because the aim of the measurements with LI-1800 is to calculate aerosol optical depth and Ångström exponent characterizing size distribution of the aerosol. AOD values are archieved for all standard wavelenghts, though generally AOD at 500 nm is used for studies due to the very high autocorrelation of AOD values in a certain spectrum.

LI-1800 has options to measure PAR and illuminance, and very special quantities like leave transmissivity, leave reflectivity, etc. These quantities are not measured operationally but occasionally in special campaigns or for orders. LI-1800 is installed at the Budapest observatory also (for more technical details see: *LI-1800 Portable Spectroradiometer Instruction Manual,* 1989).

4.3. Sunphotometer SP02

Sunphotometers are special devices that are designed to measure one of the physical quantities characterizing the radiation transmissivity of the atmosphere.

The early sunphotometers measured turbidity, but the recent models masures rather aerosol optical depth. Filters are used in sunphotometers to select the required wavelengths, so their accuracy is considerably lower than that of the insturments having monochrometers. Their considerably less complicated construction and, as a consequence, their far lower prices makes them, however, practical to use in monitoring networks.

Sunphotometer SP02 is a relatively accuate and reliable device in its category. Two are operated by the HMS, one is at the Marczell György Main Observatory in Budapest and the other is at the Kékestető Observatory that is situated on the highest peak of Hungary called Kékesető.

SP02 has four channels to measure aerosol optical depth that are as follows: 412, 500, 675, and 862 nm. In case of SP02, the aerosol optical depth should not be calculated from measured irradiance, because its output is the aerosol optical depth itself (namely, the voltage output corresponds to aerosol optical depth value).

4.4. UV Biometer

UV Biometers are special broad band detectors and can be considered not so old type of detectors, since the first experimental copies started to work in the seventies, their use started to spread in monitoring networks in the late eighties and mainly in the early and mid-nineties, so most of the national networks are not older than 15 years. The UV Biometers output erythemally weighted irradiance.

Measurement of UV radiaton has not been an important task in meteorological and atmospheric physical observations in the previous decades, because its flux density is neglectably low as compared with that of the visible and infrared ranges, so consequently it has no important role in radiation budget of the atmosphere. Its crucial role in production of vitamin D in human body and its harmful effect on biological systems, however, has motivated some scientists or institutes to establish sporadic campaigns to measure UV spectrally or in broad band way. But no any long term UV monitoring network has been operated until discovering atmspheric ozone depletion. The number of national networks has increased rapidly since then. Due to their simple construction and, consequently, their considerably lower price, use of broad band UV detectors are far more practical in networks than use of higher accuracy spectral equipments.

UV monitoring network of the HMS includes five sites that are as follows: Budapest, Kékestető, Kecskemét, Sármellék, and Siófok. The former four stations have started to operate in 1994, while in Siófok, the measurements have been started in 2009.

5. Quality assurance and quality control

QA/QC procedures are of crucial importance nowadays in operating high accuracy networks. The calibrations, routine checkings and tests are performed in the measuring practice of the HMS in the ways and with the frequencies that are recommended by the manufacturers of the equipments. Each procedure for the different instruments are performed by following the working instructions of the HMS. To descript the details would not be reasonable in this paper, but it is still to be noted that to follow the given instructions is of stressed importance for us, we operate a regional center for solar radiation.

6. Operation of regional center for solar radiation, WMO Region VI, Budapest

The HMS has been operating the regional center for solar radiation since 1980. The solar radiation regional centers of WMO are operated to represent the World Radiation Reference (WRR) of the World Radiation Center, Davos, Switzerland, for the instruments of the countries of the given region. The absolute cavity pyrheliometer that represents the WRR in our regional center is the HF 19746 instrument. It participate in each international pyrheliometer comparisons held in the World Radiation Center in every fifth year. The imortance of our activity as regional center has decreased a bit during the decades since 1980, as more and more countries have started to operate absolute cavity pyrheliometers. The spectrum of our activity has, in the same time, widened by installing high resolution spectral instruments, narrow spectral range detectors, and sunphotometers. Currently we have reference to calibrate instruments as follows: spectrophotometers, spectroradiometers, filterradiometers, sunphotometers, UV Biometers, and special spectral devices including PAR meters, illuminance meters, personal UV dosimeters, filters, or other special radiometers.

As concerns the future of the operation of the regional center, it is to be noted that though its significance as representing world reference pyrheliometric scale had a bit decreased in the previous years, increasing interest appeared from other scientific areas, such as biology, agronomy, daylighting, etc. Particularly, the inclusion of UV radiation-related studies and experiments started to be more frequent in the last decade in the scientific areas mentoned above.

Another task that will probably be more and more important even in the near future is the testing of diode array spectroradiometers. This is a brand new technology and its three main advantages are the very high speed, the high spectral resolution, and the fact that the diode array spectrometers do not include moving parts. Nowadays, however, several problems are still unsolved, so the accuracy and reliability is considerably lower than that of traditional monochrometer spectrometers. Results of calibration of some of these instruments that we have made confirmed the fact mentioned above.

7. Selected results

Selected results from studies and researches based on the data coming from the activities shown in the previous sections are shown here. The results shown are a small part of the entire set of results. Detailed analyzis of the results is not discussed here, because it would be the aim of separate papers. Thus, in addition to very brief analyzes, the references where the details can be found are given instead.

7.1. Total ozone

Total ozone measurements have been carried out at the HMS since 1969. *Fig. 2* shows the long term variation of total ozone for Budapest for the period 1969–2012. The percentage deviations of yearly means from the mean of many years are shown in the figure. The mean of many years have been calculated for the period 1969–1980 to eliminate the effect of the stronger ozone decrease of the later decades on the estimated mean that characterizes a quasi-unperturbated condition.

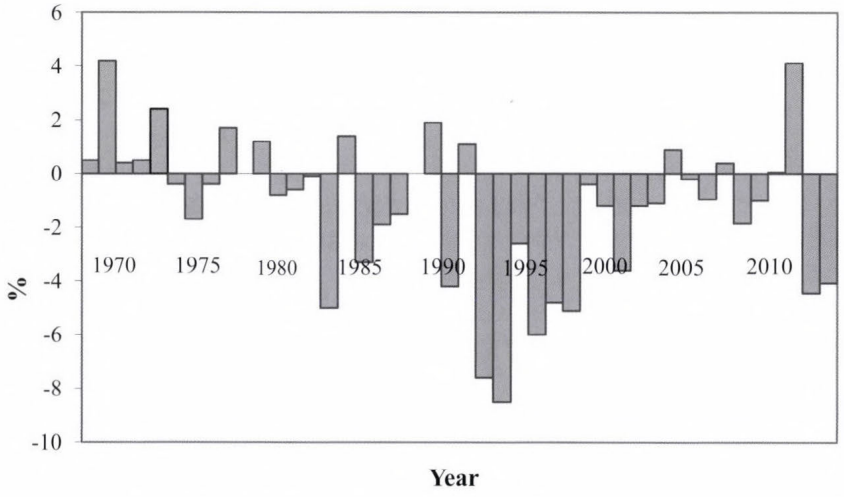

Fig. 2. Percentage deviations of yearly means of total ozone content from the mean of many years for Budapest, 1969–2012.

It is well-known that total ozone has a yearly course in the midlatitudes that is more and more stressed from the equator towards the poles. *Fig. 3* shows the calculated average (smoothed) yearly course for Budapest with the upper and lower limits of natural variability (defined as two times of the standard deviation).

It is to be noted that despite the ozone recovery, considerable ozone losses were found for most of the summers of the last decade. The summer ozone losses in the last decade were significant even considering all 43 summers

despite the increasing trend in the yearly averages. It is difficult to answer the question today whether it is a consequence of some variations in the circumastances influencing ozone concentration that are of climatic scale or they were incident events.

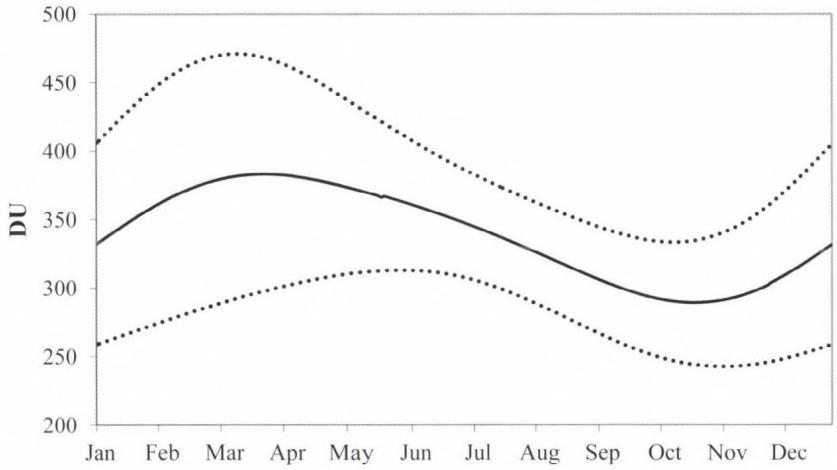

Fig. 3. Average yearly course of total ozone for Budapest.

7.2. Short-wave radiation transmission of the atmosphere

7.2.1. Graybody optical depth and the scattering parameter

Some results concerning the behavior of transparency of the atmosphere are shown in this section.

Fig. 4 shows the long term variation of graybody optical depth for Budapest for the period 1967–2011 that is demonstrated by the yearly means. The values are increasing up to 1994 and decreasing from then (similar behavior was found for each monthly trends), thus a sectioned trend analysis was performed as an experiment for the period 1967–1994 and for 1995–2011. Considering the different months, based on the trend analysis for the period 1967–1994, the only month was December for which significant increase was not found. It is to be noted, that reason for no yearly averages are shown in the figure for 2008 and 2009 is that no sufficient number of measured data were available for the correct calculation for both years due to susbequent failures of the solar tracking system. It has unfortunately taken for a long time while the manufacturer's trouble-shooting trials has become succesful.

Yearly course of GBOD is shown in *Fig. 5*. It is clear, based on the figure, that transparency of the atmosphere is higher in winter than in summer, as it has been expected otherwise.

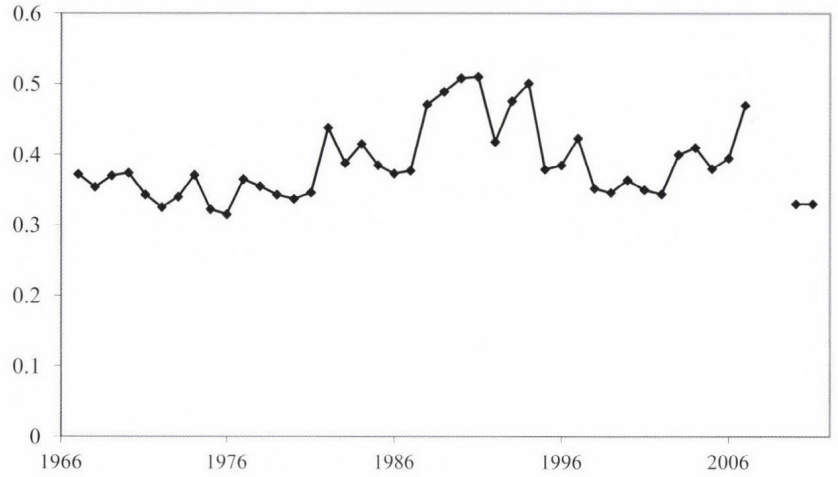

Fig. 4. Yearly means of graybody optical depth for Budapest for the period 1967–2011.

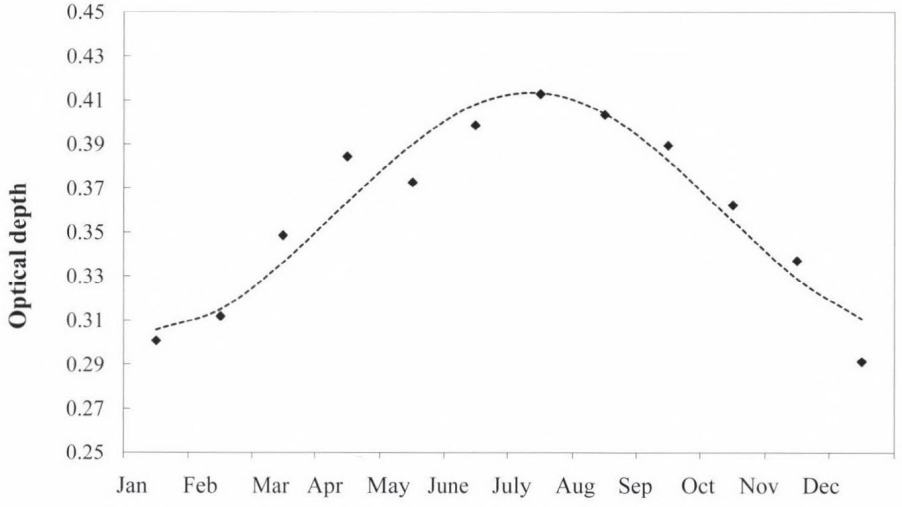

Fig. 5. Average yearly course of graybody optical depth for Budapest.

These studies were performed for another special quantity called scattering parameter (Θ). It is an indicator of ratio of diffuse irradiance to the total global irradiance in the way that measured diffuse-to-global ratio is normalized by the diffuse-to-global ratio theoretically calculated for the Rayleigh-atmosphere, and it is in high correlation with turbidity (*Kaskaoutis et al.,* 2007) Thus it is expressed in the following way:

$$\Theta = \frac{D/G}{D_R/G_R},$$

where D and G are the diffuse and global irradiances, respectively, measured on a horizontal surface, D_R and G_R are the diffuse and global irradiances calculated for Rayleigh-atmosphere for the time of the observation, respectively.

Long term variation (1967–2002) and average yearly course were also determined for scattering parameter, and the results are very similar that those obtained for graybody optical depth.

Scattering parameter is a useful quantity to examine how close, in respect of transparency, the real atmosphere can be to the Rayleigh atmopshere in the clearest cases (least polluted cases, actually). In order to perform this, the lowest D/G values (occurred during the experimental period) were to determine. A reference can be the minimum value of a month (monthly absolute minimum value) from the long-term database. *Fig. 6* shows the yearly course of absolute minimum values of D/G (solid line) and values of D/G calculated for Rayleigh-atmosphere (D_R/G_R) for the middle of the hour intervals used for the study (dashed line). The important message of *Fig. 6* is that in the clearest (least polluted) cases the atmosphere above the observatory almost equalled to the Rayleigh-atmosphere.

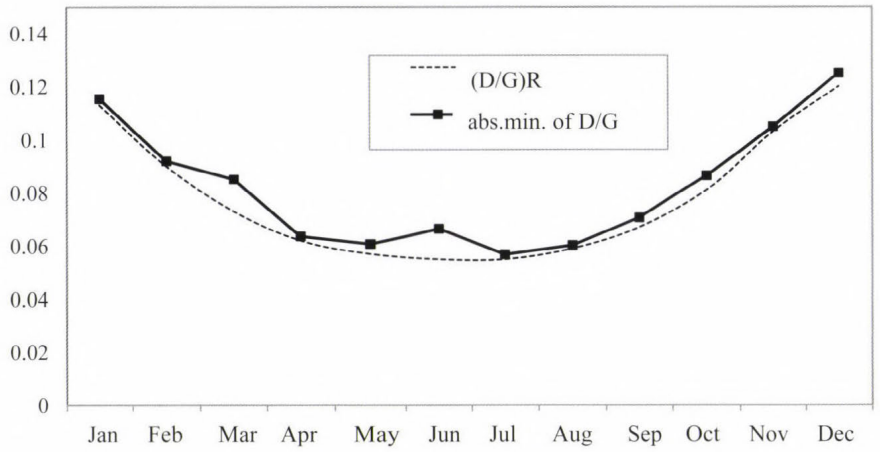

Fig. 6. Yearly course of monthly absolute minimum values of D/G and calculated values of D/G for Rayleigh-atmosphere.

7.2.2. Optical properties of the aerosol

Optical properties of aerosols were studied by using AOD and Ångström exponent. Due to the consequentially very high autocorrelation between the AOD values calculated for the different standard wavelengths from the same spectrum, AOD for 500 nm (AOD_{500}) was used for each study. To determine

long term variation of AOD_{500} was not possible because of the insufficient number of observations (that is a consequence of the fact that AOD, due to its definition, can be estimated when solar disc is not covered by any clouds).

However, a mean value (a quasi-mean of many years, actually) of AOD for Budapest was determined. The value obtained, of course, is not too reliable due to the abovementioned insufficiency. However its estimation, in contrast with the trend analysis, has reasonability due to the fact that for this estimation all data together are needed. The same can be stated for the mean of many years for the Ångström exponent.

Aerosol optical depth values are available for the period 1996–2011, so the mean of many years is valid for a period of 16 years. Since the results obtained for GBOD, that should relatively be in close connection with AOD, show that the transparency of the atmosphere has started to incease from the mid-nineties, the obtained mean for AOD_{500} will then underestimate a mean of many years concerning a longer period. A value of 0.28 was found as mean of many years for AOD_{500}. A general experience for values of AOD at 500 nm is well-known as a result of numerous previous studies. It says that urban and industrial areas are characterized by values higher than 0.3, while rural areas are characterized by values lower than 0.2. Values between 0.2 and 0.3 characterize areas polluted on the average. Though the obtained value seems to be indicative of the suburban situation of the observatory, where there is no considerable industrial pollution, but traffic, it is to be noted that the correct value supposed to be some tenth higher due to the expected underestimation of AOD_{500} due to the aforementioned reasons.

The obtained mean of many years for wavelength exponent is 1.31. Considering the facts about different values of α written in 2.4., this value can be called usual value. It shows that the usual particle size is the dominant in the aerosols being present in the air colum above the observatory.

Dependence of Ångström exponent on AOD_{500} was also studied and the result is shown in *Fig. 7.* It was found that despite the considerably high dispersion of the set of dots, the two quantities are inversely proportional to each other, namely the dominant particle size increases with the increasing aerosol content of the air column. This fact has an important message to us: it means that there is a weak tendency showing bigger aerosol masses tend to be composed by larger particles with higher likelihood, statistically, and conversely: lower aerosol optical depths are, with higher statistical likelihood, produced by aerosols including smaller particles.

A parameterization technique was developed to estimate AOD data from GBOD data (*Tóth,* 2008). In principle, GBOD and AOD values calculated from irradiances that were measured at the same time, differ only due to GBOD, which is influenced by total vapor and ozone absorption (as main absorbers that can considerably vary), while AOD is not. Dependence of AOD at 500 nm on GBOD is shown in *Fig. 8.* If the aforementioned facts are accepted, the dispersion of GBOD values that belong to a given value of AOD_{500} is caused by effect of total water vapor content and total ozone content on GBOD. Consequently, if total water vapor content and total ozone content dependence

of the residuals are determined, a correction can be computed by which the relationship between the two optical depths can be improved. It means that AOD values can be computed from GBOD values by considering total precipitable water and ozone.

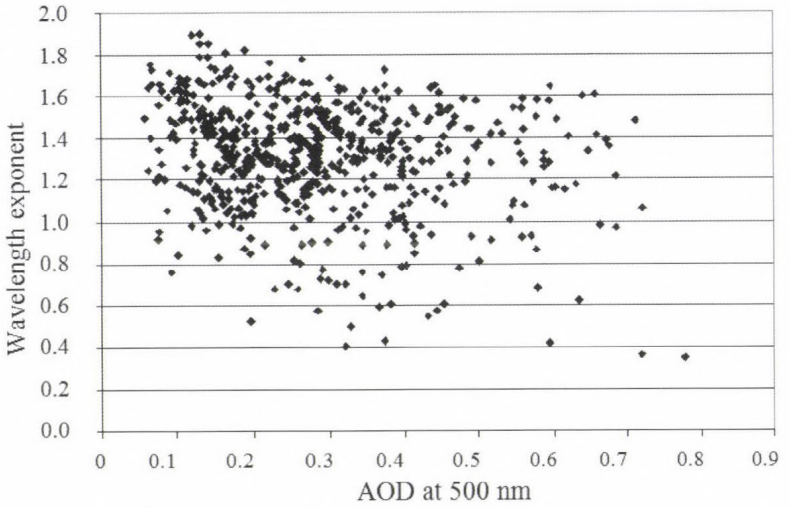

Fig. 7. Relationship between AOD_{500} and Ångström exponent.

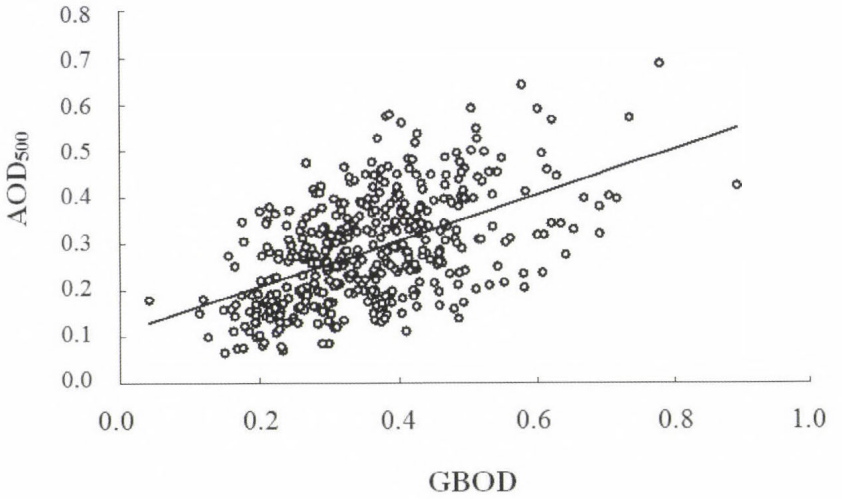

Fig. 8. Relationship between GBOD and AOD_{500}.

Total precipitable water data calculated from rawinsound observations regularly performed in the observatory and total ozone data coming from ozone measurements carried out also operationally at the observatory by the Brewer spectrophotometer were used for the parametrization, so the parametrization equation was as follows:

$$\delta_{A\lambda} = C_{0\lambda}\delta_{GB} - C_{1\lambda}X_{TPW} - C_{2\lambda}X_{O3} + C_{3\lambda}, \qquad (7)$$

where

$\delta A\lambda$ is the aerosol optical depth at wavelength λ,

δGB is the graybody optical depth,

X_{TPW} is the total precipitable water,

X_{O3} is the total air columnar ozone content,

$C_{0\lambda}$, $C_{1\lambda}$, $C_{2\lambda}$, $C_{3\lambda}$ are the conctants to determine.

The wavelength used for the study was 500 nm.This parameterization resulted in an approximately 30% increase in correlation coefficient. It means that a method is available to calculate aerosol optical depth from graybody optical depth if total precipitable water and ozone contents are known.

The discussion of the methods used for the study and detailed analysis of the results has been published in a conference proceedings (*Tóth*, 2008).

7.2.3. Relationship between aerosol size distributions and aerosol optical depth spectra

In a study, the size distribution of aerosol and its relationship with wavelength exponent was investigated. The size distribution was estimated by a mathematical inversion method developed by King et al. (*King et al.,* 1978). The size distribution can be deterined from aerosol optical depth spectrum by using this method.

It was found that the obtained size distributions are in good connection with the wavelength exponent. Though they are not independent from each other due to the fact that the aerosol optical depth spectrum is the base for both, to analyze their relationship is still reasonable, because they are very different quantities. While the wavelength exponent is one number that characterizes the fequency of larger particles, and the dominant particle size can be estimated from it by using an empirical equation determined by Ångström (*Ångström,* 1929), the size distribution determined by King's method is a function estimating a realistic size distribution of the particles being present in the aerosol at the time of the recording of the spectrum. So we had to find a property of the function that could be brought into relationship with a number. The shape of the function was found to be suitable to compare. It was found that the shape of the size distribution changes with the value of α. Results are shown in *Fig 9*. To make details more easily visualizable, size distributions are graphed for 5 different values of α, but the effect found is the same if all size distributions is involved.

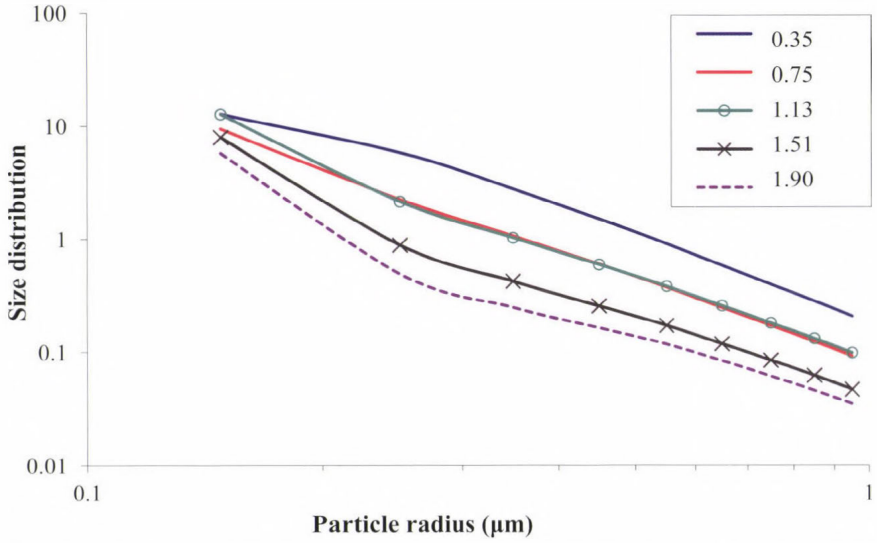

Fig. 9. Shapes of computed aerosol particle size distributions for different values of Ångström exponent.

The size distribution function for the lower values of α has a typical shape that is decreasing slowly for the shortest particle radii (approx. 0.3 μm – 0.4 μm) and from that value it is decreasing by a bit higher rate. This shape tends to be quasi-linear and then tends to be inflectious from about 0.6 μm, but oppositely to the shortest radii: first it is decreasing a bit rapidly, then slowly, and the inflection point is at about 0.25 μm that remains almost unvariable along the studied radius range (a bit shifted to the longest radii, but even the maximum shift is only some hundredth μm). The another inflection point was found somewhere between 0.6 μm and 0.7 μm. *Fig. 10a, b,* and *c* show that differences between the shape of the size distributions are very small for a given value of α.

7.2.4. Dependence of spectral diffuse-to-direct irradiance on the atmospheric turbidity

A special investigation was performed previously concerning dependence of spectral diffuse-to-direct beam irradiance ratio on the atmospheric turbidity and solar zenith angle for the wavelength range from 300 nm to 1100 nm *(Kaskaoutis et al,* 2007). It was performed by modeling based on measured data. Since the detailed analyzes cannot be discussed in this paper, only two of the several results are shown here. *Fig. 11* shows the spectral ratios for AOD_{500} = 0.3, α = 1.3, and solar zenith angle of 20°, for three different values of single cattering ratio.

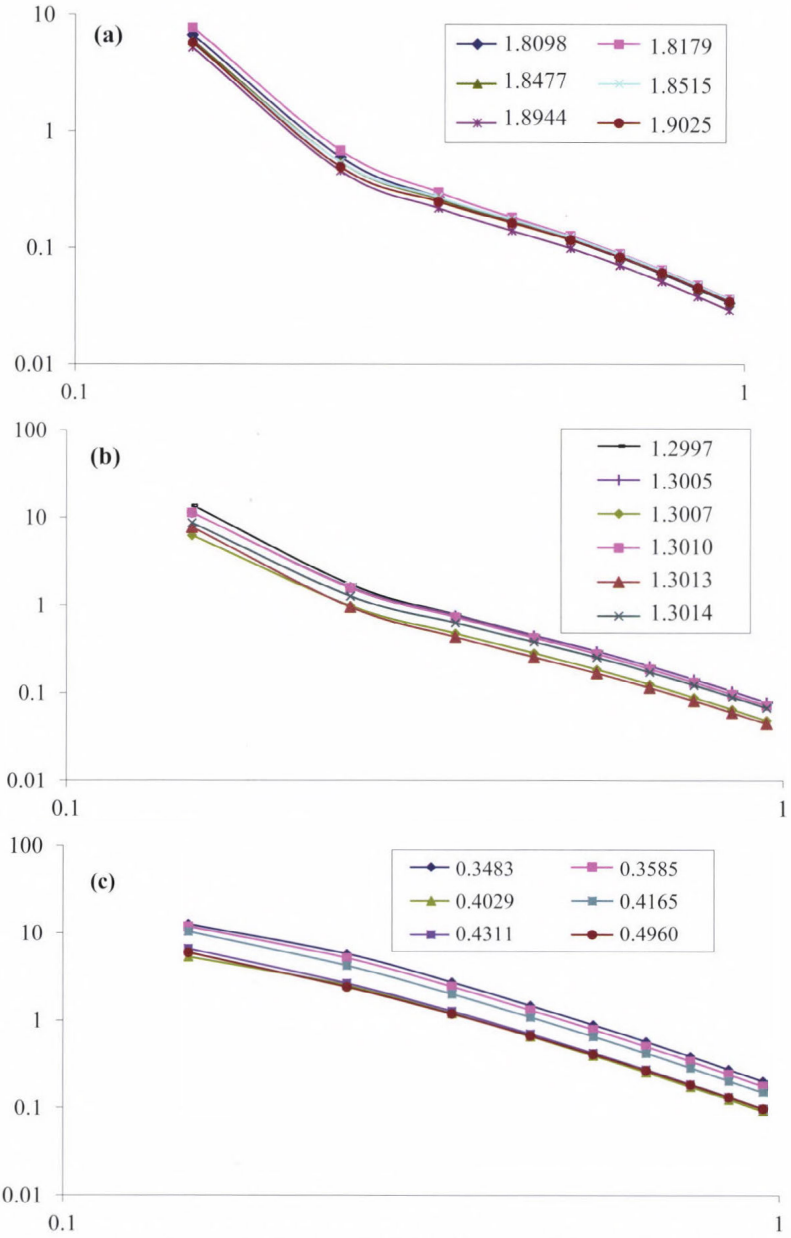

Fig. 10. Computed aerosol size distributions for high (a), normal (b), and low (c) values of Ångström exponent.

Fig. 12 shows the ratios for AOD = 0.3, single scattering ratio = 0.9, and solar zenith anlge = 60°, for three different values of α. It can be seen from both figures that the ratio increases moderately towards the shorter wavelength in most part of the visible range, then this increase becomes very rapid in the shortest part of the visible range, and the rate of increase is considerably sharper

in the ultraviolet range. The increase rate increases with increasing single scattering albeldo, as it has been expected. At the same time, the increase rate increases as wavelength exponent increases (the dominant particle size decreases). Detailed analysis of all results can be found in the paper referred.

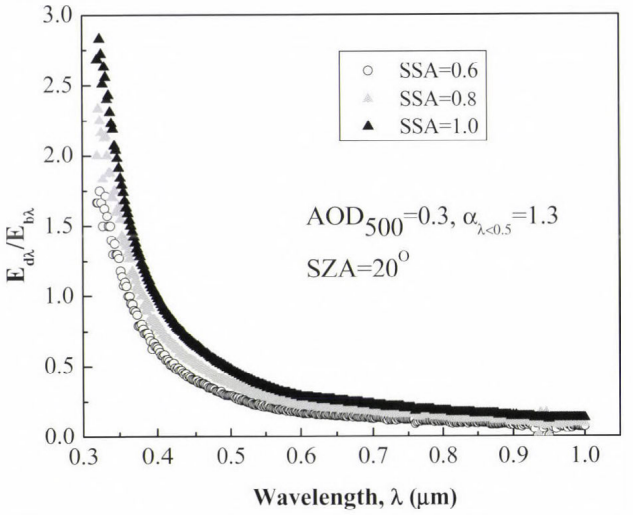

Fig. 11. Spectral diffuse-to-direct beam ratios for $AOD_{500} = 0.3$, $\alpha = 1.3$, and solar zenith angle of 20°.

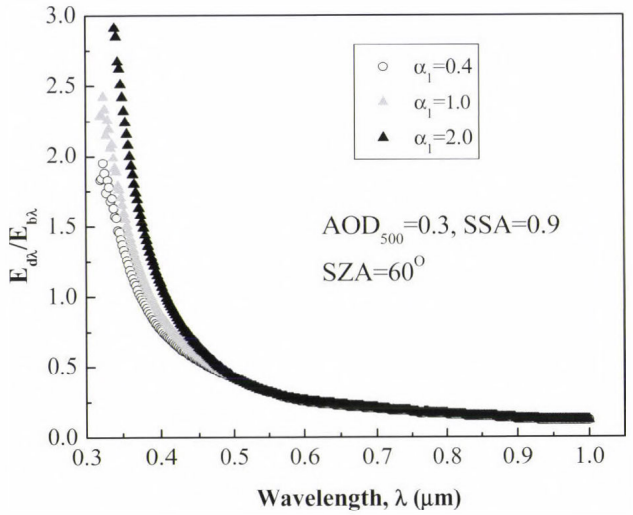

Fig. 12. Spectral diffuse-to-direct beam ratios for AOD = 0.3, single scattering ratio = 0.9, and solar zenith anlge = 60°.

7.3. *UV radiation*

Some results concerning UV radiation are shown in this section.

Fig. 13 shows the characteristic maximum spectra for the different months for Budapest. It is clear from the figure that no considerable UV irradiance is received by the Earth's surface below 296 nm in Budapest even in case of the summer months. Despite this fact, measuring biologically effective UV radiation at the shorter wavelengths is reasonable, because the biophysical effects of the shortest wavelengths that yet reaching the Earth's surface are not known exactly today.

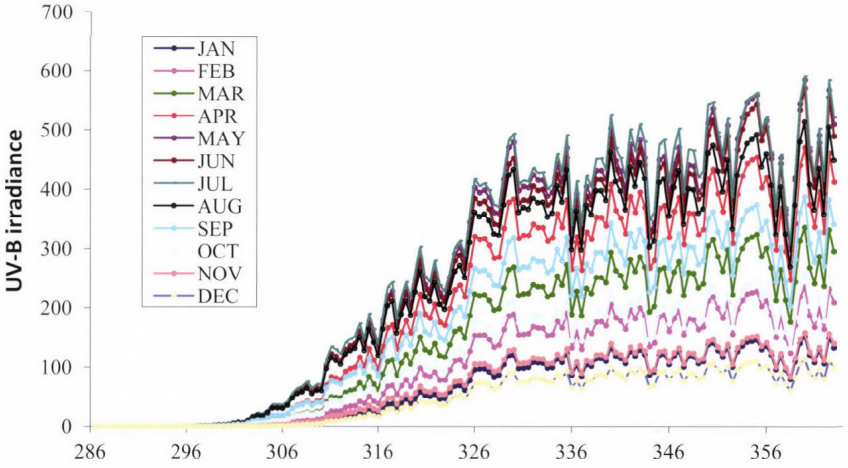

Fig. 13. Characteristic maximum UV spectra for the different months for Budapest coming from observations by Brewer MKIII spectrophotometer

The yearly totals and summer season totals of the biologically effective UV dose are shown in *Fig. 14* and *Fig. 15,* respectively, for the period 1995–2012. It is to be noted that despite the UV monitoring network of HMS includes five stations, only four were used for studying long term variations of UV. The reason is that one of the stations, Siófok, has started to operate in 2009, as it was mentioned in Section 4.4, so its inclusion in this study was not reasonable. An increasing trend of 3–6%/10 years was found for the different stations for both quantities. The obtained value fits the world-wide tendencies and the values computed from models for these areas (*Lytinska et al.,* 2009). The reason for the UV increase is that the increase of atmospheric transparency presumably compensates the UV reducing effect of the total ozone increase.

7.4. *Effects of atmospheric circumstances on UV radiation reaching the Earth's surface*

It is very important to know how atmospheric circumstances affect UV irradiances reaching the Earth's surface. Some results concerning this are shown in this section.

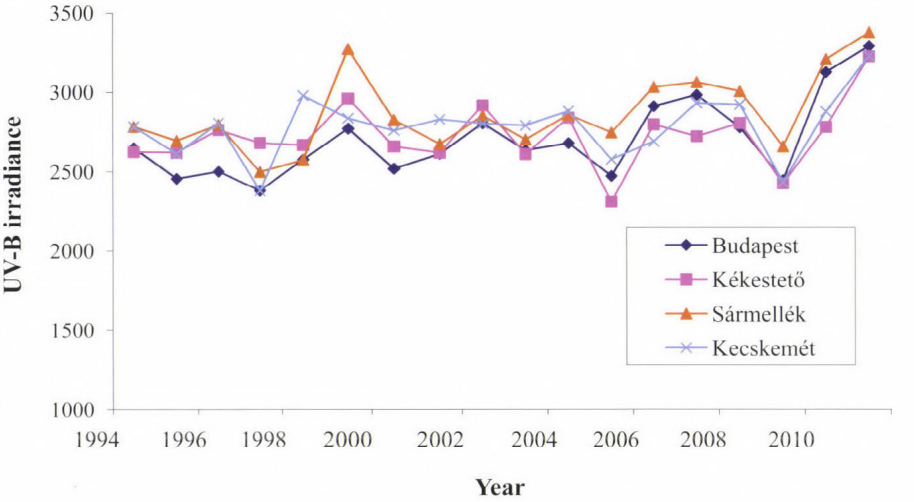

Fig. 14. Yearly totals of erythemally weighted UV irradiances for 4 sites of Hungary.

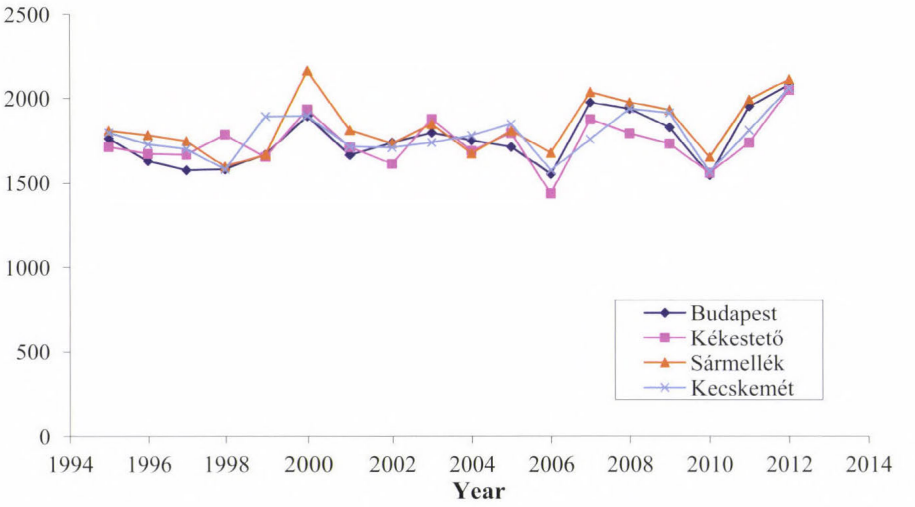

Fig. 15. Summer season totals of erythemally weighted UV irradiances for 4 sites of Hungary.

Fig. 16 shows the relationship between total ozone content and UV radiation reaching the Earth's surface. Theoretically well-known that, as a consequence of strong ozone absorption in the UV-B range, the UV irradiance measured at the surface should be in inverse relationship with total ozone: the higher the total ozone content, the lower the UV irradiance. This fact can be seen well in *Fig. 14,* where the daily course of erythemally weighted UV radiation is shown for two days for which total ozone has considerably differed.

This dependence well-traced exactly for our total ozone and UV radiation dataset.

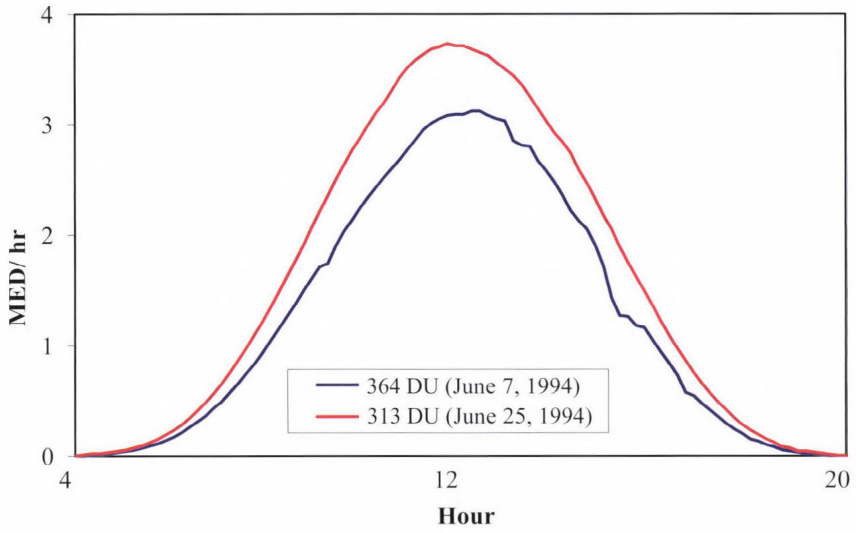

Fig. 16. Daily course of erythemally weighted UV irradiance for two days with different total ozone content.

A relatively frequently used quantity is the RAF (Radiation Amplification Factor) that is a practical indicator of the principle mentioned above. RAF shows the percentage increase in erythemally weighted UV irradiance that is resulted in an effect of 1% decrease in total ozone content. Value of RAF was determined by us by using spectrophotometric total ozone data and measured broad band UV data. The RAF obtained by us was in Section 1.17 (*Németh et al.*, 1996) that is in good agreement with values obtained by other authors. Though not being used generally, to determine a special spectral RAF (SRAF) seemed to be very informative (it can be called the 'monochromatic version' of the aforementioned broad band RAF). SRAF was determined from data coming from Brewer measurements. *Fig. 17* shows the dependence of SRAF on the wavelength. The slope sharply incresases towards the shorter wavelengths. The very important medical conclusion from the figure is that relatively smaller ozone losses can have dangerous effects, mainly for persons having extremely sensitive skin, because the pattern suggests that considerable amount of photons can appear at the very short wavelengths where the human skin is not prepared for their effect. Though it is not clear if it can be more dangerous either on short time scale or on longer time scale, it seems to be sure that the effect is considerably dangerous on longer scale. Furthermore, considering the significant ozone deficits in the last 6–7 summers, this result warns us to be very careful with sunbathing.

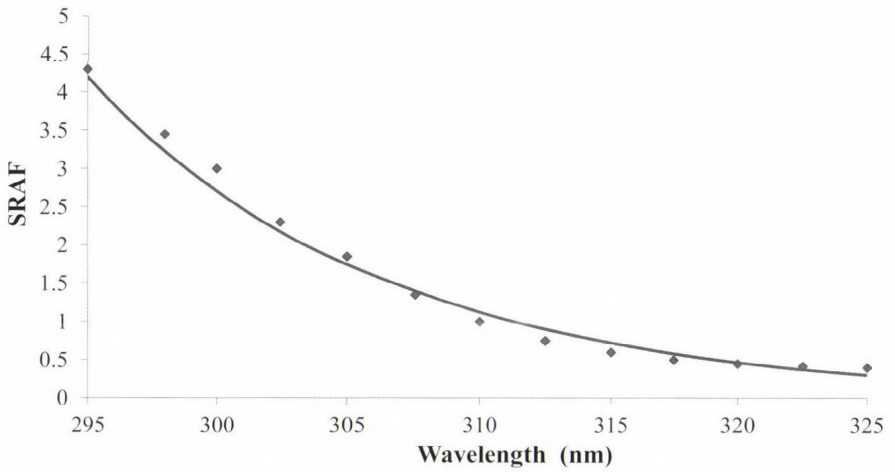

Fig. 17. Dependence of SRAF on the wavelength.

The effect of cloudiness on the UV irradiance received by the Earth's surface is an important parameter. The results have been published by us previously (*Németh et al.,* 1996), so they are discussed here only very briefly. Though radiative transfer is known exactly in theory and can be modeled with relatively good reliability, in very practical tasks, for example in case of UV forecast, a reliable empirical relationship can solely be used due to the fact that numerous parameters of the cloud influencing radiative transfer in the cloud is not known exactly at the time of the given observation. A non-heigth-dependence CMF (Clud Modification Factor) was determined by us, which means that only the percentage cloudiness was considered in the study. All data were used for the study with no any filtering that depends on atmospheric circumstances. The results are shown in *Figs. 18a* and *b* for solar elevations higher than 30° and lower than 30°, respectively. The non-linear dependence is clear from the figures, but a peculiar behaviour is revealed from *Fig. 16b:* UV irradiances can, with high statistical likeliohood, be higher in case of 10–40% cloud coverage than irradiances detected for clear sky conditions. The explanation for this unexpected behavior is the very effective radiation scattering towards the Earth's surface on the edges of the clouds. Cloud coverages between 10 and 40% can be produced by mainly cumuli with relatively high probability and, due to their ragged, fragmented structure, the scattering on the cloud edges can thus be considerable.

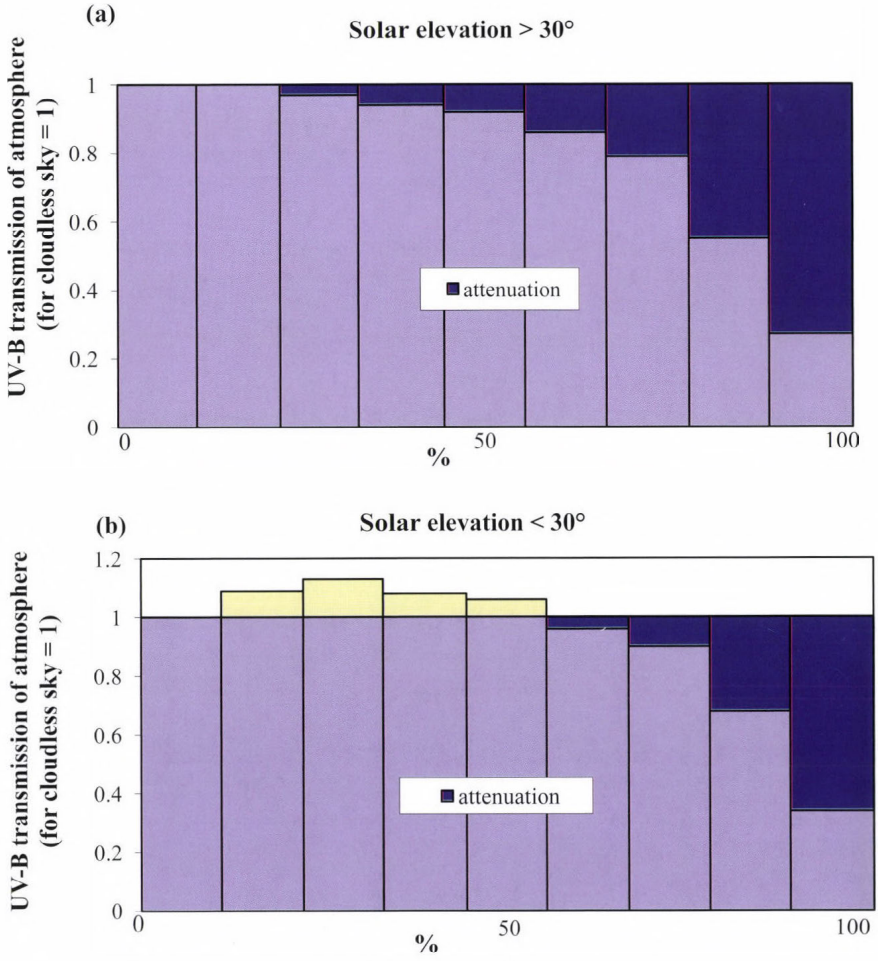

Fig. 18. Dependence of UV transmission on cloudiness in the atmosphere in Budapest of solar elevations higher (a) and lower (b) than 30°.

7.5. Verification of surface solar radiation outputs predicted by ALADIN model

Verification of predicted solar radiation data from ALADIN weather forecast model was carried out in 2001 (*Tóth,* 2002). Not the results of the verification themselves are that are shown here, because on the one hand, it cannot be aim of this paper and on the other, several improvements have been made on the model since the time of the verification in question. The aim is to show how high resolution spectral data can be useful for and can contribute to the verification by pointing out the strongnesses and weaknesses of the concerned module of the model. The verification was performed for total global fluxes for three stations and direct as well as diffuse fluxes for one station, because direct and diffuse

radiation measurements have been carried out at only one station (Budapest) then. The predicted data for both the subsequent day and the day after subsequent day were verified.

Two main factors affect solar radiation flux reaching the Earth's surface in case of wider energy range radiation: total water vapor content and total aerosol content of the air column. A study was still invented to find out how ALADIN would be able to estimate surface solar radiaton fluxes in cloudless cases or in other words: how it would be able to estimate atmospheric radiation transmission. Implicitly, the data were used for this study that has been produced at cloudless situation. The detailed description of filtering that was made in order to select data meeting with the criteria given by us, see the paper referred. To represent radiation transmission condition of the atmosphere, aerosol optical depth at 500 nm (AOD_{500}) was selected.

The aim of the study was to obtain any information on reliability of ALADIN-made surface solar radiation forecasts concerning different atmospheric radiation transmission conditions. It is very important, since considerable radiation extinction can in many cases occur even when sky is cloudless.

Relationship between AOD_{500} and difference of observed and predicted solar irradiances (DIF_DIR, DIF_DIF, and DIF_GL in the figures) was studied for all three radiation parameters. Results are shown in *Figs. 19, 20,* and *21.* AOD_{500} is represented on horizontal axis and differences between observed and forecasted irradiances are represented on vertical axis in each figure.

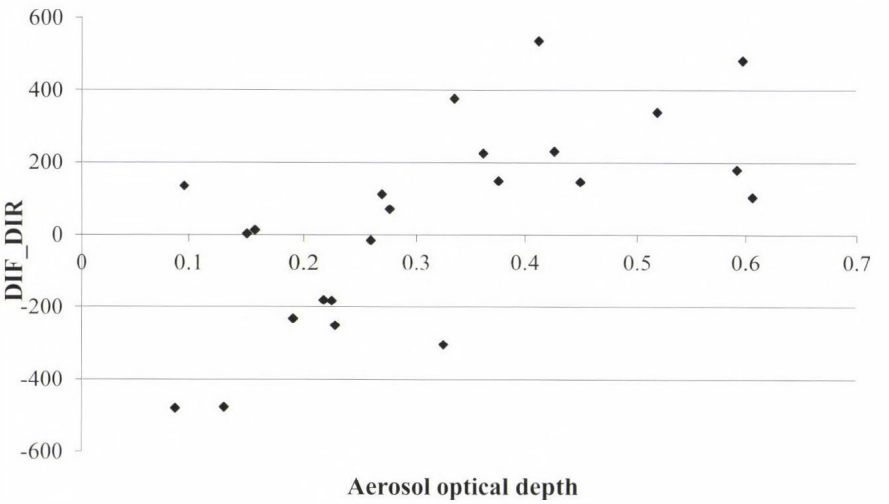

Fig. 19. Dependence of DIF_DIR on AOD_{500}.

Results for direct irradiance is shown in *Fig. 19.* Based on our five-year-long aerosol optical depth data series, it was known that average value for the

Marcell György Main Observatory in Budapest was approximately 0.3 for 500 nm. It is clear from *Fig. 19* that for the most part, overestimations are found for values of AOD_{500} lower than 0.3 and underestimations are found for τ_{500} values higher than 0.3. It means that the model underestimates direct irradiance reaching the surface in cases when atmospheric radiation transmission is high, namely when very small amount of pollutant is present and overestimates it in cases when atmosphere is considerably polluted. Based on it one can conclude, that atmospheric radiation conditions predicted by the model are generally approaching average conditions due to that the model draftly handles parameters influencing radiation transmission, namely its variability is lower than that of the corresponding true parameters. The model predicts more polluted atmosphere compared with reality in very clear cases being close to Rayleigh atmosphere. These findings are confirmed by results of the same study made for diffuse irradiance (*Fig. 20*). Pollutants and water vapor intensively scatter radiation, consequently diffuse (scattered) irradiance observed at Earth's surface increases as larger amount of them is present in the atmosphere. It can be seen in *Fig. 20* that in case of diffuse irradiance, inverse effect was found as compared to that found for direct component: the model overestimates diffuse irradiance in cases of high transmission ($AOD_{500} < 0.3$), namely it forecasts more polluted conditions than the true state of atmosphere and, at the same time, it underestimates in cases of lower transmission, namely it forecasts lower pollution than that appearing in true atmosphere. The same effect lies behind this phenomena like in case of direct fluxes so the explanation is the same: the model tends to produce such physical conditions of atmosphere that result in more average atmospheric transmission than those occurring in reality. Those mentioned above are valid for global radiation also (see *Fig. 21*), but the effect is relatively less evident due to the fact that global irradiance is the sum of the previous two parameters so the effect in queston decreases.

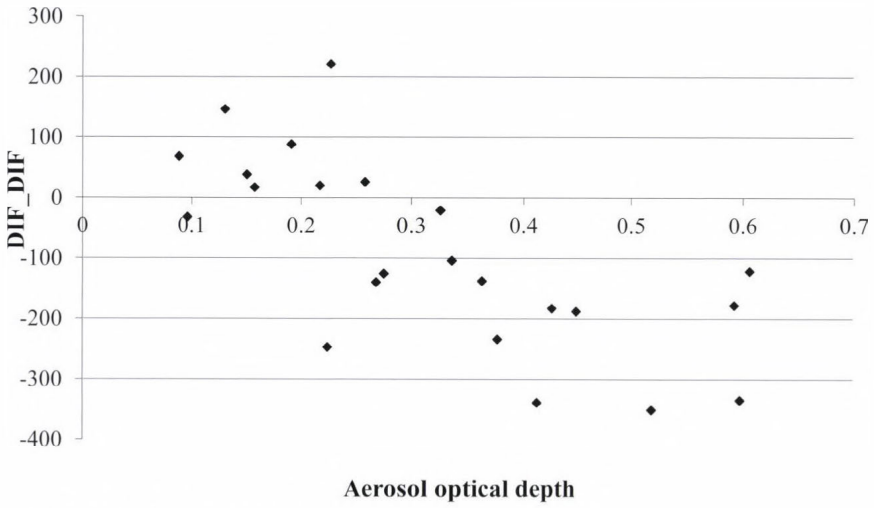

Fig. 20. Dependence of DIF_DIF on AOD_{500}.

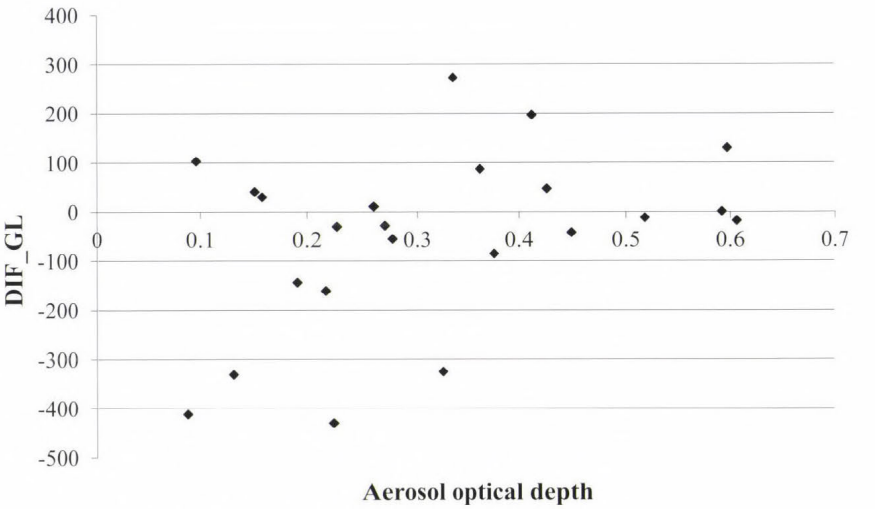

Fig. 21. Dependence of DIF_GL on AOD_{500}.

8. Other special studies

Special individual studies occur with variable frequency in our activities and concern wide area in solar radiation measurements. They concern radiation transmission of given materials, or variation of their radiation transmission due to longer exposure to solar radiation (mainly UV), or spatial distribution of radiation source's emitted radiation, etc. Amongst these studies, results for only one are shown that are very useful and instructive. Several experiments concerning UV radiation transmission change of UV blocking plastic foils used in agriculture and special seed holding materials used in agriculture. The plastic foils have been exposed to UV radiation in the whole vegetation period (from May to October), and the change both in their special mechanical parameters and in their radiation transmission was investigated. The latter was performed by us, but measured data were provided to the former also by the Hungarian Meteorological Service. The experiment were supported by Hungarian Institute for Agrucultural Engineering (for other details, see *Csatár* and *Fenyvesi,* 2008).

Five kinds of foils were examined: 1) a plastic foil that included no UV filtering material was for control, 2) white-colored foil including 5% UV filtering metarial, 3) white-colored foil including 20% UV filtering material, 4) violet-colored foil including 5% UV filtering material, 5) violet-colored foil including 20% UV filtering material. Only a brief summary is discussed here to concern the most important results that are shown in *Figs. 22a, b, c.*

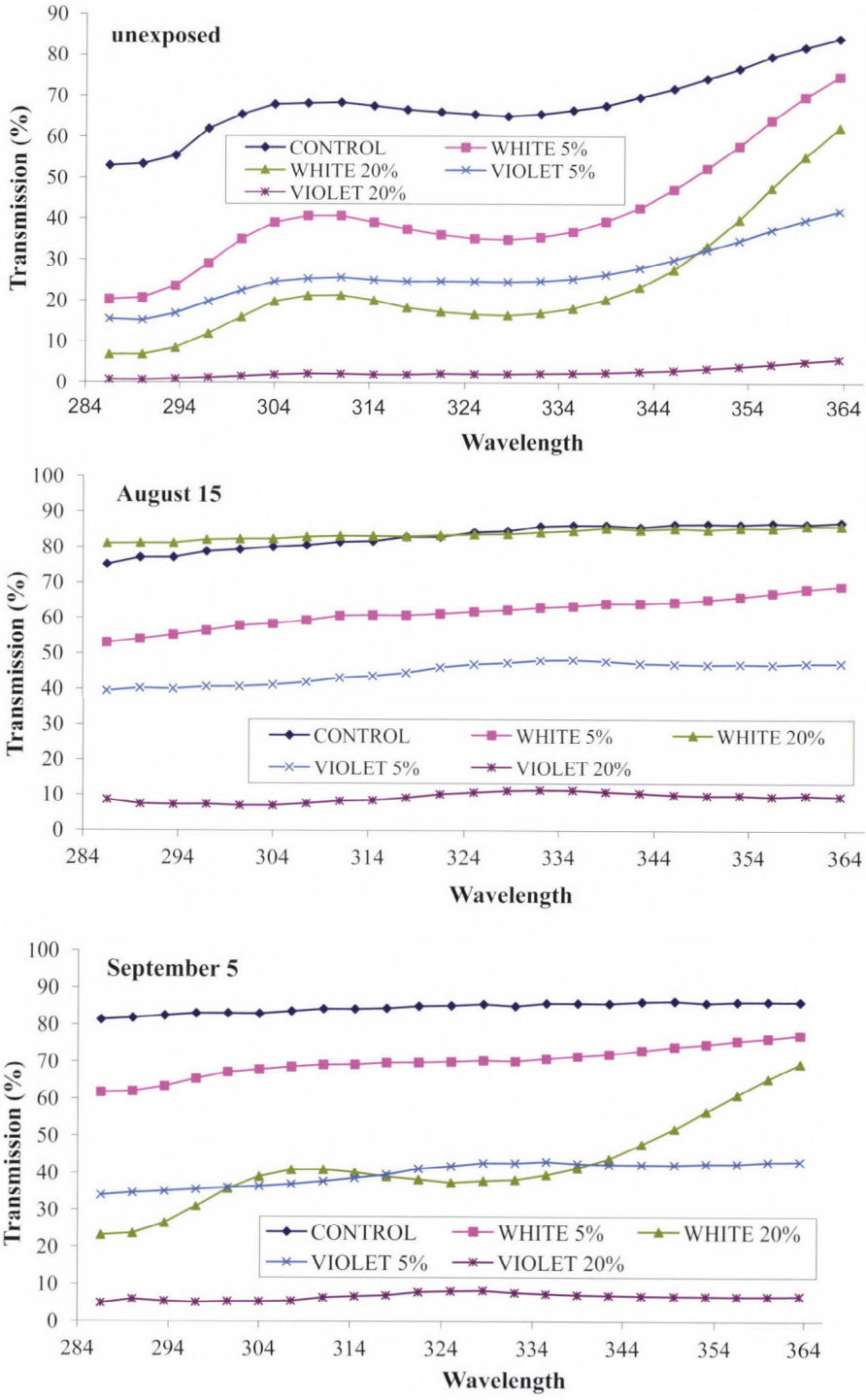

Fig. 22. UV transmission spectra of the examined plastics for three different sampling dates during the experiment (unexposed, Aug 15, Sep 5)

The plastics have been installed at the end of May in the garden of the Marczell György Main Observatory of the HMS and have thus been exposed to solar radiation until the beginning of October covering the entire vegetation period. Samples have been taken out from them by two weeks and their mechanical parameters and UV radiation transmission spectra have been examined to study variations in them. UV transmission spectra for three selected sampling dates for the spectral range from 286.5 nm to 363 nm for five selected sampling dates are shown in the figure. The behavior of the plastics are very similar and difference was found only quantitatively. It is evident that the UV blocking effect starts to loose partly soon after the installation, namely their increasing UV transmission increases and become considerable for the white foils and increases by a low rate for the violet foils for the second half of the examined period. It is also clear that at the end of the period, a chemical recovery starts up because the UV trasmission decreases a bit. Also a smoothing effect can be seen in the fine structure of each of the transmission spectra, but one type (white 20 %) retrieves partly its original shape. One can conclude that the destructive effect of UV radiation on the UV blocking material is not entirely irreversible. These results have stressed importance for the agriculture in application of the foils in UV protection of plants.

9. Conclusions

Due to the nature of this paper, conclusions cannot be made in the usual way. A special measurement technique and its theoretical background, covering, at the same time, a wide scale of measurement types were shown that is operationally run at the Hungarian Meteorological Service. Results coming from studies and investigations concerning very considerably different areas were shown, so their detailed analyzes were not possible, though some conclusions was made straight after showing the given results.

It is, however, still to be noted that use of high resolution spectrophotometry and spectroradiometry in atmospheric physical observations and investigations is very useful for numerous purposes, and it has reason for existence both in operational measurements and special experiments. It should be clear based on the studies and results showed that modern solar radiation measurements require its inclusion to an increasing degree.

Acknowledgements—Since high number of very different studies was shown in this paper, numerous domestic and foreign colleagues have contributed to them, so to list them is on the one hand, unreasonable and on the other, impossible due to the fact that contribution or significance of contribution of given persons cannot be estimated correctly. Still, one person is to be mentioned by name, because he is the author's long term colleague in the solar radiation area and his work on most part of the aforementioned studies is of primary importance. He is *Zoltan Nagy*, who is currently the head of the Atmospheric Physics and Measurement Technics Division of the HMS where all activities on solar radiation belong to. Nevertheless, the author thankfully acknowledges every international and domestic project that has founded or contributes by any way to the tasks shown, as well as also thankfully acknowledges all persons who have contributed to them in any degree.

References

Alföldy B., Osán, J., Tóth, Z., Török, Sz., Harbusch, A., Jahn, C., Emeis, S. and *Schäfer*, K., 2007: Aerosol optical depth, aerosol composition and air pollution during summer and winter conditions in Budapest. *Sci. Total Environ. 383,* 141–163.

Ångström, A., 1929: On the atmospheric transmission of sun radiation and on dust in the air. *Geogr. Anna. 11*, 156–166.

Brewer MKIII Spectrophotometer (Double Spectrometer) Operator's Manual, 1998: SCI-TEC Instruments Inc.

Csatár, A. and *Fenyvesi, L.*, 2008: Effect of UV radiation and temperature on rheological features of multi-layer agricultural packaginig foils. *Prog. Agricult. Engin. Sci. 4,* 27.

Dobson, G.M.B., 1957: Observer's handbook for the ozone spectrophotometer (on behalf of the International Ozone Commission (I.M.A.) in conjunction with Messrs. R. & J. Beck Ltd.). *Pergamon Press*.

Kaskaoutis, D.G., Kambezidis, H.D. and *Tóth, Z.*, 2007: Investigation about the dependence of spectral diffuse-to-direct-beam irradiance ratio on atmospheric turbidity and solar zenith angle. *Theor. Appl. Climatol. 89,* 245–256.

King, M.D., Byrne, D.M., Herman, B.M, and *Reagan, J.A.*, 1978: Aerosol side distributions obtained by inversion of spectral optical depth measurements. *J. Atmos. Sci. 21,* 2153–2167.

LI-1800, Portable Spectroradiometer Instruction Manual, 1989: Publication No. 8210-0030, LI-COR, inc.

Lytinska, Z., Koepke, P., De Backer, H., Groebner, J., Schmalwieser, A. and *Vuilleumier, L.*, 2009: Long term changes and climatology of UV radiation over Europe. *Final Sci. Report, COST Action 726.*

Németh, P., Tóth, Z. and *Nagy, Z.*, 1996: Effect of weather conditions on UV-B radiation reaching the earth's surface. *J. Photochem. Photobiol. B 32*, 177–181.

Tóth, Z, 2002: Verification of surface solar radiation fluxes predicted by ALADIN. *ALADIN Newsl. 21,* 80–92.

Tóth, Z, 2008: Long-term variation of atmospheric shortwave radiation transmission above Budapest, Hungary. *Proceedings of the 4th International Conference on Solar Radiation & Daylighting SOLARIS 2008, Hong Kong, China,* 27–35.

IDŐJÁRÁS

Quarterly Journal of the Hungarian Meteorological Service
Vol. 117, No. 4, October–December, 2013, pp. 435–450

Comparison of two Lagrangian dispersion models: a case study for the chemical accident in Rouen, January 21-22, 2013

Ádám Leelőssy[1], **Erika Lilla Ludányi**[1], **Márk Kohlmann**[1], **István Lagzi**[2], and **Róbert Mészáros**[1,*]

[1]*Department of Meteorology, Eötvös Loránd University, P.O. Box 32, H-1518 Budapest, Hungary*
[2] *Department of Physics, Budapest University of Technology and Economics, Budafoki út 8, H-1111 Budapest, Hungary*

**Corresponding author E-mail: mrobi@nimbus.elte.hu*

(Manuscript received in final form July 10, 2013)

Abstract—Industrial accidents have been a serious environmental and public health issue for the last decades. Although the development of atmospheric dispersion models was largely motivated by the notorious nuclear catastrophes, simulations are now mostly used in cases of chemical accidents that regularly occur in all parts of the world. In an accidental situation, the accuracy of the results is primarily important for risk management and decision making strategies. However, it largely depends on the meteorological conditions and the quality of input data. A chemical accident happened in a factory in Rouen, France on January 21, 2013. The emitted methyl mercaptan gas caused odor and sickness in densely populated areas, including Paris. The meteorological conditions were rapidly changing in both space and time during the release period, thus the case is particularly challenging for dispersion models and provides a good basis for testing them.

Dispersion of the released methyl mercaptan gas was estimated using the PyTREX trajectory model, developed at the Eötvös Loránd University, and NOAA's HYSPLIT model. The simulation results are in a good agreement with media reports of the polluted areas, and lead to a better understanding of the complex synoptic situation at the time of the accident. Comparison of the results of two models also provided information about the uncertainty of the predictions and pointed out the most important directions for further development of the PyTREX model.

Key-words: atmospheric dispersion, accidental release, HYSPLIT, industrial accident, air pollution, Lagrangian model

1. Introduction

In case of an accidental release of toxic material into the atmosphere, dispersion models provide valuable information for risk management and decision support. In most cases, simulation of the dispersion of pollutants released during an accident is a difficult task because of the complex physical processes occurring in the atmosphere, the importance of fast response, and the lack of information about the details of the release. Computer simulations, based on either Eulerian or Lagrangian (trajectory) approaches are now able to provide fast and accurate estimation about the concentration patterns after an accident.

In the past years, PyTREX, a Lagrangian trajectory model has been developed for regional to continental scale simulation of dispersion of passive pollutants. In this work, we present the PyTREX results for the case of the Lubrizol accident in Rouen, compared against HYSPLIT, a state-of-the-art software, to estimate the uncertainty and show the strengths and weaknesses of our model. The Rouen accident happened under complex meteorological conditions where dispersion models are less reliable and depend largely on the accuracy of their host numerical weather prediction model.

This work aims to provide a case study of the Rouen accident, involving its synoptic meteorological conditions and the consequent dispersion patterns. On January 21, 2013, a gas leak caused a significant release of methyl mercaptan from the Lubrizol factory. Although methyl mercaptan had no health risks, its intense odor could cause nausea and headache. As the dispersion plume crossed densely populated areas, many complaints arrived from the public, and numerous media announcements and reports have been published. Despite the fact that methyl mercaptan gas measurements are not available, these media reports provide information about the affected areas and the intensity of the odor in a particular location, thus the dispersion of the plume can be qualitatively verified.

2. Overview of atmospheric dispersion modeling

Atmospheric dispersion involves multiscale air pollution problems that are treated using different mathematical approaches and modeling tools. Computer simulations have to take into account the horizontal advection of the released pollutant by the mean wind, the horizontal and vertical mixing caused by turbulent diffusion, chemical reactions, wet and dry deposition, sedimentation, and radioactive decay. The wide range of scales and physical processes led to the development of several atmospheric dispersion models that are specialized to the simulation of certain types of air pollution situations.

Microscale models, often referred to as street canyon simulations use a computational fluid dynamics (CFD) approach to solve the governing equations as well as the dispersion equation on a very fine grid around a complex

geometry like a city, a tunnel or an industrial site (*Balczó et al.*, 2011; *Di Sabatino et al.*, 2008). Sophisticated CFD models like Ansys or OpenFOAM are able to take into account microscale phenomena, the effect of buildings, and turbulence generation on the walls (*Cheng* and *Liu*, 2011; *Yamada*, 2004). This approach provides valuable information about urban air quality (*Vardoulakis et al.*, 2003), however, it is not applicable on larger scales due to its large computational cost and the unrepresented physical processes like atmospheric stability and mesoscale wind patterns (*Baklanov*, 2000).

On meso- to macroscale, atmospheric dispersion simulations are based on the output data of numerical weather prediction (NWP) models. Besides the three-dimensional wind field, atmospheric stability characteristics, planetary boundary layer height, and surface parameters are also obtained from NWP results (*Stohl et al.*, 2005). Regional and continental scale dispersion models often use the same grid as the host NWP to solve the transport equation. This Eulerian approach has the advantage that meteorological data is obtained without interpolation, complex chemical reactions can be easily taken into account, and the output concentration and deposition fields are directly computed by the model (*Simpson et al.*, 2012).

Lagrangian simulations avoid the costly partial differential equation solvers and compute tracer trajectories using the NWP-provided wind field. As the calculation of a few trajectories is very fast, Lagrangian models are able to provide immediate information about the dispersion's direction without calculating concentrations. However, with thousands of trajectories, cluster analyses can be carried out to obtain the concentration field. Turbulent mixing is taken into account with a stochastic random walk method (*Stohl et al.*, 2005). Although Lagrangian models require costly interpolation of meteorological data, this approach is particularly suitable for near-source simulations, where numerical diffusion introduces a large error in Eulerian models. This error can be largely reduced by using adaptive gridding that refines the resolution if large gradients are present (*Lagzi et al.*, 2009). Coupled modeling systems have also been introduced that use a near-source Lagrangian treatment within a large-scale Eulerian model (*Brandt et al.*, 1996).

Lagrangian approach is used in state-of-the-art atmospheric dispersion software like the NAME, HYSPLIT, and FLEXPART models (*Draxler* and *Hess*, 1998; *Stohl et al.*, 2005). Besides their worldwide application for environmental studies and risk management, these models provided valuable and accurate information during recent air pollution episodes like the Fukushima accident in 2011 or the eruption of Eyjafjallajökull volcano in 2010 (*Dacre et al.*, 2011; *Long et al.*, 2012; *Srinivas et al.*, 2012; *Stohl et al.*, 2011).

The simulation of long-term average air pollution patterns caused by continuous release is a challenge for most atmospheric models. EMEP's Eulerian model provides continental scale forecasts and archive data for most air pollutants' concentration with a special attention on acidic compounds (*Simpson*

et al., 2012). The online coupled dispersion and mesoscale weather prediction model WRF-Chem is a powerful tool for atmospheric dispersion modeling: its Eulerian approach allows the simulation of complex chemical reaction systems, meanwhile, the integrity with an NWP model makes it easy to run detailed simulations in any meteorological situations (*Huh et al.*, 2012).

On regional scale, plume models like AERMOD or ADMS are often used to calculate long-term average concentrations caused by a continuous pollutant source (*Holmes* and *Morawska,* 2006; *Silverman et al.*, 2007). Plume models assume straight downwind dispersion from the source point and a concentration field with Gaussian distribution in crosswind and vertical direction (*Cimorelli et al.*, 2005). Although these models are not reliable in complex weather situations and terrain, their fast runtime makes them optimal for long-term statistical air quality investigations for both normal (*Righi et al.*, 2009) and accidental (*Leelőssy et al.*, 2011) continuous releases.

In Hungary, an integrated atmospheric dispersion modeling system (AERMOD) and a trajectory and particle dispersion model (FLEXTRA-FLEXPART) are used by the Hungarian Meteorological Service for environmental monitoring and risk management (*Kocsis et al.*, 2009; *Steib* and *Labancz*, 2005). The CHIMERE model was also adapted at the Hungarian Meteorological Service for operative mesoscale air quality forecast in Budapest (*Baranka* and *Labancz*, 2009). At the Paks Nuclear Power Plant, the RODOS decision support system provides a Lagrangian trajectory model for regional to continental scale simulations. The SINAC program system was developed to follow the consequences of radioactive releases of a hypothetical nuclear accident (*Földi et al.*, 2010). A multiscale Lagrangian and Eulerian dispersion model, TREX has also been developed at the Eötvös Loránd University for the area within 30–500 km from the power plant (*Mészáros et al.*, 2010). For larger scales, the extended PyTREX trajectory model has been developed. Local scale CFD simulations are carried out at Budapest Technical University and Eötvös Loránd University using Fluent, Miskam, and OpenFOAM models (*Balczó et al.*, 2011; *Goricsán et al.*, 2004).

3. Model description

3.1. The HYSPLIT model

In the present work, we used HYSPLIT and PyTREX models to simulate the consequences of the industrial accident in Rouen. HYSPLIT is a widely used Lagrangian dispersion model developed by the National Oceanic and Atmospheric Administration Air Resources Laboratory (NOAA ARL). Its worldwide applications cover various forward and backward simulations from meso- to continental scale (*Challa et al.*, 2008; *Koracin et al.*, 2011; *Long et al.*, 2012; *McGowan* and *Clark*, 2008; *Shan et al.*, 2009). HYSPLIT calculates

single trajectories based on meteorological fields provided by the Global Data Assimilation System (GDAS) database. Particle motion in each timestep is defined as a sum of an advective and a turbulent component (*Draxler* and *Hess*, 1998). The advective motion is obtained directly from the wind field, however, vertical turbulent wind fluctuations are computed using Hanna's parameterization based on stability characteristics defined by the Monin–Obukhov length (*Draxler* and *Hess*, 1998; *Moreira et al.*, 2011). While large scale turbulence is estimated with a random walk method, small scale turbulent diffusion is calculated with a puff approach: each particle has a horizontal extent with a Gaussian concentration distribution, which broadens according to the local turbulence intensity. Concentration field is given as the superposition of concentration fields of all particles.

3.2. The PyTREX model

PyTREX is a continental scale trajectory model developed at the Eötvös Loránd University. It computes single particle trajectories based on meteorological data provided by short-range forecasts of the Global Forecast System (GFS). GFS is initialized in every 6 hours and provides output fields for every 3 hours, thus the first and second timestep of each model run was used to create a continuous 3-hourly forecast database for archive situations. Forecast outputs were preferred against analyses in order to gain advantage of GFS parameterizations that provide derived quantities such as turbulent surface fluxes or precipitation patterns. GFS grid has 0.5-degree spatial resolution from which data is obtained for any point with linear interpolation in both space and time. For compatibility with the GFS outputs, PyTREX uses spherical coordinate system in horizontal and pressure system in vertical direction. Meteorological and user-defined input data of PyTREX are presented in *Table 1*.

Table 1. Input data requirements of the PyTREX trajectory model

Release data and simulation setup	**Meteorological data (GFS)**
Release location(s)	Geopotential on main pressure levels
Release height(s)	Wind components on main pressure and near-surface levels
Release time(s) and length(s)	Temperature on main pressure and near-surface levels
Simulation duration	Surface pressure, temperature
Total released mass from each location	Surface height above ground level
Number of trajectories from each location	Planetary boundary layer height
Minimum computational timestep	Surface momentum and heat flux
Halftime of radioactive decay	Mixing ratio on main pressure and near-surface levels

PyTREX trajectories are calculated using a linear scheme from the superposition of advective and turbulent motions:

$$\frac{d\underline{r}}{dt} = \underline{v} + \underline{v}_t, \tag{1}$$

where $\underline{v}$ is the vectorial sum of the horizontal wind and the vertical motion, $\underline{v}_t$ is the vector of turbulent fluctuations, and $\underline{r}$ is the position of the particle. While $\underline{v}$ is directly obtained from GFS outputs, $\underline{v}_t$ is calculated using the Langevin equation (*Stohl et al.*, 2005):

$$dv_{t,i} = -v_{t,i}\frac{dt}{T_{Li}} + \sigma_i\sqrt{\frac{2dt}{T_{Li}}}\zeta(0,1), \tag{2}$$

where $v_{t,i}$ is the ith component of the turbulent velocity vector, $T_{L,i}$ is the Lagrangian timescale representative for the ith direction, σ_i is the turbulent fluctuation of the ith component of the wind vector, and $\zeta(0,1)$ is a random number from a standard normal distribution, generated with the Mersenne Twister algorithm of Python's *random* module.

The TLi Lagrangian timescales and σ_i turbulent wind fluctuations are estimated using the Monin–Obukhov theory, thus we need to compute the atmospheric stability parameter z/L (*Draxler* and *Hess*, 1998):

$$\frac{z}{L} = \frac{z_1 \cdot k \cdot g \cdot T^*}{T_1 \cdot u^{*2}}, \tag{3}$$

where z is the height above ground, L is the Monin–Obukhov length, k is the von-Kármán constant, and g is the gravitational acceleration. Besides constants and surface parameters, PyTREX uses the temperature data T_1 of z_1 height, the first level above ground in the meteorological dataset (80 m for GFS data).

Friction temperature T^* and friction velocity u^* are calculated from surface heat and momentum fluxes:

$$u^* = \left(\frac{\sqrt{\overline{\rho u' w'}^2 + \overline{\rho v' w'}^2}}{\rho}\right)^{0,5}, \tag{4}$$

$$T^* = -\frac{H}{\rho_f c_p u^*}, \tag{5}$$

where $\overline{\rho u' w'}$ and $\overline{\rho v' w'}$ are surface momentum fluxes and H is the surface heat flux. Both momentum and heat flux data is directly obtained from GFS outputs. The air density ρ and air density on surface ρ_f are calculated from the temperature field using dry air assumption. Accordingly, c_p is the specific heat of dry air.

Based on the stability characteristics presented in Eqs. (3–5) and the planetary boundary layer height provided by GFS, the velocity fluctuations and Lagrangian timescales are obtained through Taylor's parametrization, which was set up in a way presented by *Moreira et al.* (2011). The computational timestep dt is defined as the tenth of the minimum of Lagrangian timescales (*Stohl et al.*, 2005). However, in order to reduce the computational cost for near-surface trajectories, a minimum timestep can be defined that also gives a lower boundary for Lagrangian timescales.

Besides drawing single trajectories, PyTREX calculates concentration field on a three-dimensional rectangular grid based on the density of trajectories crossing the specified grid cell during a certain time period.

4. Synoptic situation during the Rouen incident

On January 21, 2013, a chemical accident happened in a factory of the Lubrizol company located in Rouen, northwestern France. The firm announced that a significant amount of non-toxic methyl mercaptan gas had been released from approximately 07 UTC (http://www.paris-normandie.fr/article/actualites/en-direct-fuite-de-mercaptan-chez-lubrizol). Although no health risk was identified, an unpleasant smell spread across northwestern France after the accident, reaching Paris at the following night. Media announcements reported serious complaints of odor from several districts of the capital. Odor caused by methyl mercaptan gas was also reported from Normandy and Southeastern England (*Fig. 1*) (http://www.bbc.co.uk/news/world-europe-21147361).

Looking at the map of northwestern France (*Fig. 1*), it might be confusing that odor was reported within 24 hours from largely different directions from Rouen, including Paris, which is located to the southeast from the location of the accident, and also from England, to the northwest of the factory. Furthermore, despite that the accident happened only 120 km away from the capital, it took more than 12 hours for the plume to reach Paris. These unusual dispersion patterns were caused by a complex synoptic situation involving a significant shift in the wind direction within a short time period.

On January 20, 2013, two dominant processes were detectable that would determine the spreading of the emitted material. The first synoptic object was a mature trough above the Mediterranean – North African region, with a corresponding low pressure system above the western basin of the Mediterranean Sea (*Fig. 2* (a)-(d)). This low pressure system was severed off

into a bi-central system by the inertia of the cold air arriving at the rear of the trough, along the western coastlines of France (*Fig. 2* (a)). The primary low remained above the Mediterranean, and was being advected eastward with the rest of the trough, while the secondary low (object A), gaining enhanced circulation by baroclinity was advected towards Northern France.

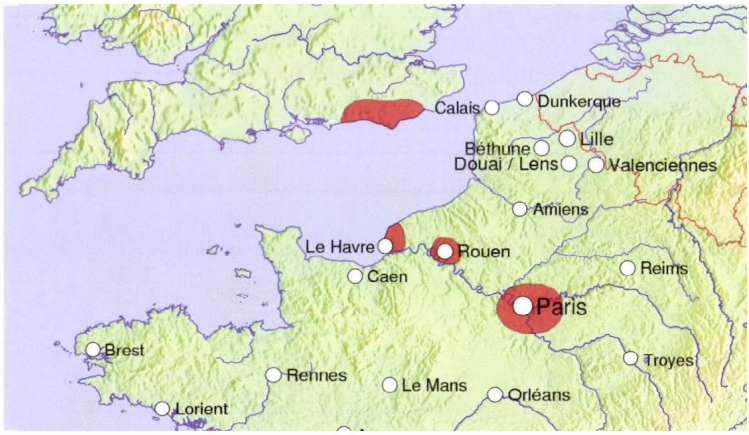

Fig. 1. The most affected areas based on media coverage after the Lubrizol chemical accident in Rouen, January 21-22, 2013.

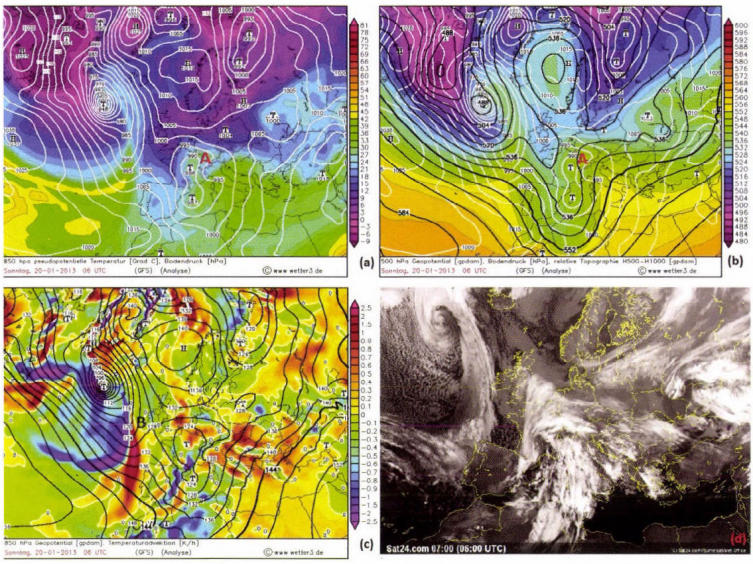

Fig. 2. GFS output (a)-(c) and infrared satellite image (d) at 06 UTC, January 20, 2013. (a) Equivalent potential temperature and MSLP (EPT850) (b) 500 hPa height (gpdam), MSLP and 500/1000 ReTop, (c) Height (gpdam) and TA at 850 hPa. Courtesy of wetter3.de and sat24.com, respectively.

The second main synoptic process was a rapidly deepening trough above the Atlantic, characterized by strong winds and cold advection on lower levels (*Fig. 2* (c)). The leading edge of this trough reached the Rouen region with a cutoff low on the ground level (object B) (*Fig. 3*). Between 18 UTC, January 20, and 12 UTC, January 21, the two low pressure systems started merging in a circular motion (Fig. 3) with the first system (object A) following the streamlines of the second low (object B). At 06 UTC, January 21, the two main lows could be located at Bretagne and Southern England creating the rotating flow that would spread the emitted material southeast and northwest of the facility at the lower levels of the troposphere (*Fig. 4*, *Fig. 5*).

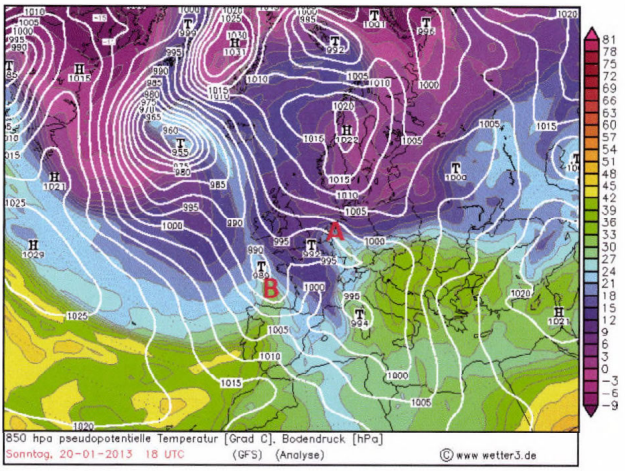

Fig. 3. GFS output on 18 UTC, January 20, 2013, EPT 850. The two stream defining lows begin to merge above the Channel. Courtesy of wetter3.de.

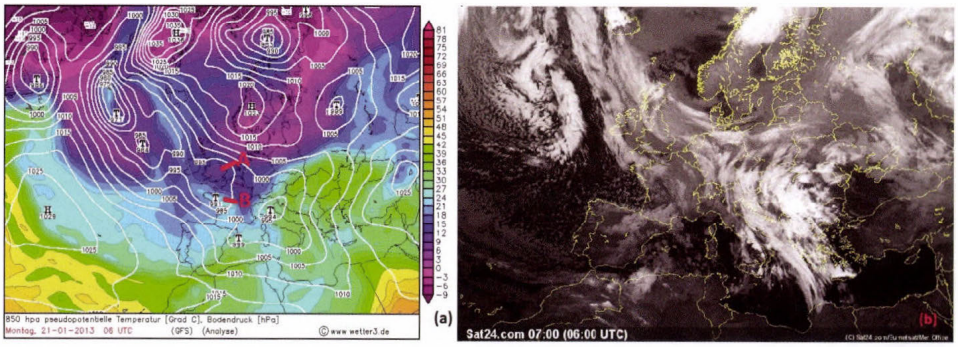

Fig. 4. GFS output (a) EPT850 and infrared satellite image (b) at 06 UTC, January 21, 2013 depicting the synoptic setup shortly before the accident. The two merging lows are clearly visible on (a), above Bretagne and Southern England. On (b), only the rotating field of the southern system is visible. Courtesy of wetter3.de and sat24.com, respectively.

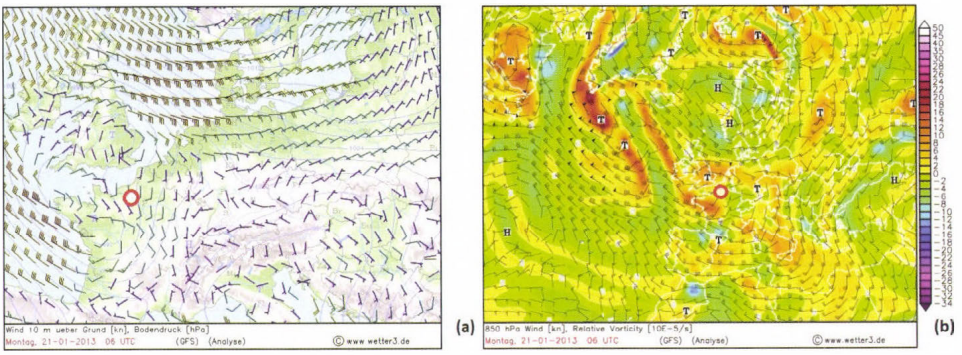

Fig. 5. GFS output at 06 UTC, January 21, 2013. Wind at 10 m (a), wind and vorticity at 850 hPa (b), depicting the bi-central rotating flow at the marked location of the accident. Courtesy of wetter3.de.

Synop reports also show a gradual shifting of the mean wind from northwesterly (18 UTC, January 21) to southeasterly direction indicating the presence of the rotating flow on the ground level. The temperature field did not significantly change due to the overcast nocturnal sky.

5. Dispersion model results

Two trajectory models, HYSPLIT and PyTREX were used to simulate the dispersion of the plume released from the Lubrizol factory during the incident. Besides understanding the pollution patterns reported in the media, our investigation aimed to compare the model results in this complex synoptic situation in order to estimate the uncertainty of trajectories and the concentration field.

The same release data was used for both model runs. Assuming a 24-hour long continuous release from 50 m height, 20400 trajectories were calculated with evenly distributed starting time during the release period. The number of trajectories was given by default in HYSPLIT, and the same value was used in PyTREX for comparable results. As the exact quantity of the released material was not known, unity total released mass was assumed for the simulation. No wet and dry deposition was taken into account, which is a good assumption for mercaptans. In PyTREX, output concentration map was produced with a 0.25 degrees horizontal and 100 m vertical resolution. Both model calculated one-hour average concentrations for each location.

HYSPLIT results clearly show the wind shift during the release period: in the first 7 hours of the accident, the plume is advected by weak southern wind over the La Manche channel (*Fig. 6*). Between the 7th and 15th hour of the incident, the wind became stronger and changed to northwesterly direction,

which forced the plume back to Northwestern France, reaching again the source region and also Paris. The weak dispersion towards England during the first hours explains the delay between the accident and the pollution reports in Paris, as well as the fairly high intensity of the odor that reached the capital. After the 15th hour of the accident, the wind turned to southeasterly again, and the plume spread towards Southern England, reaching the country approximately 24 hours after the beginning of the release.

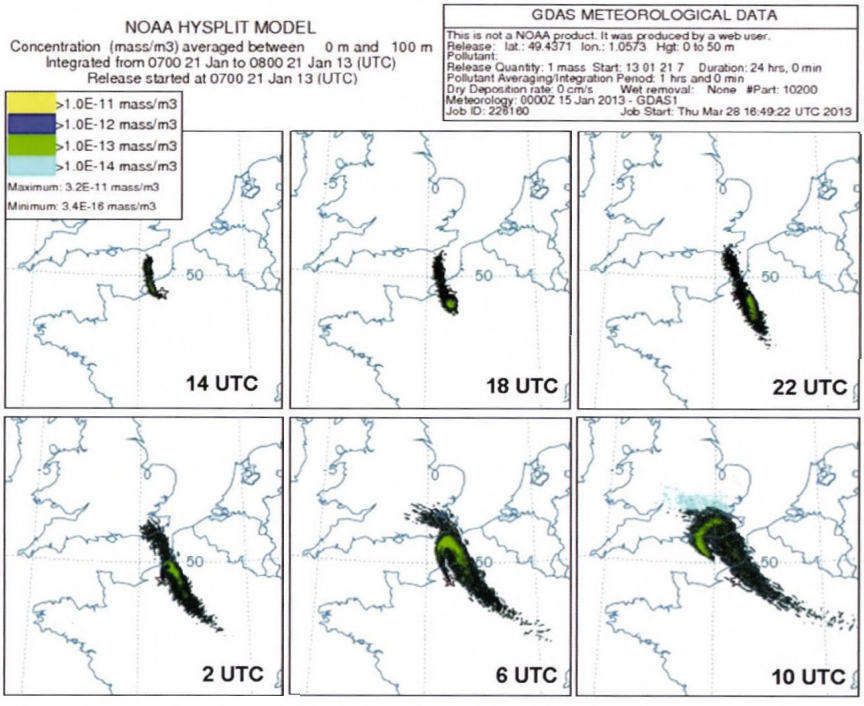

Fig. 6. HYSPLIT surface concentration field between 14 UTC, January 21 and 10 UTC, January 22, 2013. A 24 hours long continuous release was started at 07 UTC, January21. 360° change of wind direction is observable that allowed the plume to reach Central France.

The PyTREX results also well demonstrate the rapid wind shift (*Fig. 7*). The affected areas by the plume are in good qualitative agreement with HYSPLIT's results despite the different meteorological data and physical parameterizations of the models. We note that 27 hours after the beginning of the accident, both models expected that the plume would reach London. In fact, there are a few reports about odor complaints in London, thus the diluted pollutant could reach the city in a fairly high concentration (http://www.dailymail.co.uk/news/article-2266383/Smelly-gas-cloud-factory-Rouen-travels-Channel-France-Kent.html).

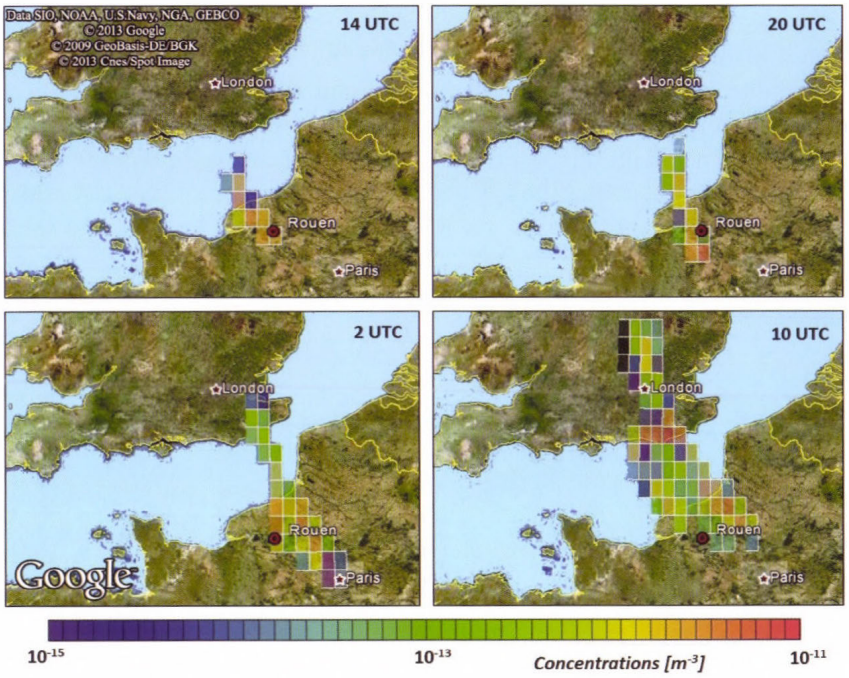

Fig. 7. PyTREX surface concentration field between 14 UTC, January 21 and 10 UTC, January 22, 2013. A 24-hour long continuous release was started at 7 UTC, January 21. Results show a good agreement with HYSPLIT's output.

In *Fig. 8*, three trajectories are presented, started in the 1st, 6th, and 16th hours of the accident. It can be seen that the pollutants spread towards Paris only within a few-hour long time period, before and after which the wind forced the plume to northern, northwestern direction.

Fig. 8. PyTREX trajectories started from Rouen at 07 (red), 13 (yellow), and 22:30 (green) UTC, January 21, 2013. Meteorological conditions allowed the plume to spread towards Paris only within a few-hour long time period.

In order to compare the concentration estimates provided by the two models, the maximum one-hour average concentration was obtained for six locations (*Table 2*). It can be seen that the values are largely different, but remain within the same magnitude for most of the locations, however, close to the source, one magnitude difference is present.

Table 2. Maximum concentration in selected locations based on two models' simulations

Location	Coordinates		Max. concentration [10^{-13}/m^3]	
	Latitude [°]	Longitude [°]	HYSPLIT	PyTREX
Rouen	49.375	1.125	149.50	34.30
Gaillon	49.125	1.375	3.31	24.70
Dieppe	49.875	1.125	8.02	8.88
Paris	48.875	2.375	1.50	6.76
London	51.375	–0.125	1.39	2.93
Bristol	51.376	–2.625	0.82	1.39

It can be concluded that the models are in a good agreement in determining the direction of the dispersion and the affected areas by the plume. The high uncertainty in concentration values might occur from the largely different turbulence treatment of the models: while HYSPLIT uses a mixture of random walk and Gaussian turbulence models, PyTREX performs a 3D random walk turbulence simulation. Based on this knowledge, PyTREX probably underestimates the near-source concentration, because it averages the density of trajectories for a 0.25×0.25 degree cell. Although no measurements are available for methyl mercaptan gas, public complaints of odor can be used to verify the models (http://www.lemonde.fr/planete/article/2013/01/22/fuite-de-gaz-a-lubrizol-mobilisation-maximale-mais-prevention-floue_1820793_3244.html). While Paris was largely affected by the plume, only a few complaints are known from London. HYSPLIT expected a similar concentration value in both cities, which is unlikely.

The uncertainty of the results might also be caused by different meteorological data: while HYSPLIT uses analyses fields, PyTREX is based on short-range forecast files with derived surface parameters.

6. Conclusion

The chemical accident in Rouen on January 21–22, 2013 happened in a complex synoptic situation with rapidly changing wind direction. Two trajectory models were used for the simulation of the dispersion in order to

understand the effect of an interplay of complex meteorological conditions, as well as to compare the model results. The results of PyTREX, a three-dimensional trajectory model developed at the Eötvös Loránd University were compared against the output of HYSPLIT, a widely used atmospheric dispersion model developed by NOAA.

The pollution affected areas in largely different directions because of the rapidly changing wind governed by a multi-centered low pressure system located above Northern France and Southern England. During the release period, a 360° turn of the wind direction was observable, as the dominant southerly wind turned into northwestern direction for a few hours, which allowed the plume to return above Northwestern France and reach Paris. Later, as the wind turned back to southerly direction, the plume crossed the Channel and affected Southern England and London.

Despite the complex synoptic situation, the different meteorological input data, and the fast changing conditions, HYSPLIT and PyTREX results were in a good agreement regarding the dispersion and the polluted areas. Concentration values in selected locations showed large differences, but remained within the same order of magnitude in most cases. PyTREX largely underestimated the near-source concentrations, while HYSPLIT provided unlikely similar results for Paris and London. Uncertainty between models is probably caused by their different turbulence treatment, which requires more sophisticated investigation and verification against measurement data.

The case study of the Rouen incident showed that PyTREX provides reliable results of dispersion patterns even in a complex synoptic situation, however, concentration values have one order of magnitude of uncertainty between the two tested software. Parallel usage of the two models, as well as adjusting parameterizations based on measurement data can largely improve atmospheric dispersion simulations to provide valuable information for risk management in a case like the Lubrizol incident in Rouen.

Acknowledgements–Authors acknowledge the financial support of the Hungarian Research Found (OTKA K81933, K81975, K104666, K109109, and K109361), the *Zoltán Magyary* Postdoctoral Fellowship, the European Union, and the European Social Fund (TÁMOP 4.2.4.A-1).

References

Baklanov, A., 2000: Application of CFD Methods for Modelling in Air Pollution Problems: Possibilities and Gaps. *Environ. Monit. Assess. 65*, 181–189.

Balczó, M., Balogh, M., Goricsán, I., Nagel, T., Suda, J.M., and *Lajos, T.*, 2011: Air quality around motorway tunnels in complex terrain: computational fluid dynamics modeling and comparison to wind tunnel data. *Időjárás 115*, 179–204.

Baranka, G. and *Labancz, K.*, 2009: Urban air quality forecast for the city of Budapest, Hungary. *EMS Annual Meeting Abstracts 6*, EMS2009-403.

Brandt, J., Mikkelsen, T., Thykier-Nielsen, S., and *Zlatev, Z.*, 1996: Using a combination of two models in tracer simulations. *Math. Comput. Model. 23*, 99–115.

Challa, V.S., Indrcanti, J., Baham, J.M., Patrick, C., Rabarison, M.K., Young, J.H., Hughes, R., Swanier, S.J., Hardy, M.G., and *Yerramilli, A.,* 2008: Sensitivity of atmospheric dispersion simulations by HYSPLIT to the meteorological predictions from a meso-scale model. *Environ. Fluid Mech. 8,* 367–387.

Cheng, W.C. and *Liu, C-H.,* 2011: Large-Eddy Simulation of Flow and Pollutant Transports in and Above Two-Dimensional Idealized Street Canyons. *Bound.-Lay. Meteorol. 139,* 411–437.

Cimorelli, A.J., Perry, S.G., Venkatram, A., Weil, J.C., Paine, R.J., Wilson, R.B., Lee, R.F., Peters, W.D,. and *Brode, R.W.,* 2005: AERMOD: A dispersion model for industrial source applications. Part I: General model formulation and boundary layer characterization. *J. Appl. Meteorol. 44,* 682–693.

Dacre, H.F., Grant, A.L.M., Hogan, R.J., Belcher, S.E., Thomson, D.J., Devenish, B.J., Marenco, F., Hort, M.C., Haywood, J.M., Ansmann, A., Mattis, I., and *Clarisse, L.,* 2011: Evaluating the structure and magnitude of the ash plume during the initial phase of the 2010 Eyjafjallajökull eruption using lidar observations and NAME simulations. *J. Geophys. Res. 116,* D00U03.

Di Sabatino, S., Buccolieri, R., Pulvirenti, B., and *Britter, R.E.,* 2008: Flow and Pollutant Dispersion in Street Canyons using FLUENT and ADMS-Urban. *Environ. Model. Assess. 13,* 369–381.

Draxler, R.R. and *Hess, G.D.,* 1998: An Overview of HYSPLIT_4 Modelling System for Trajectories, Dispersion and Deposition. *Australian Meteorol. Mag. 47,* 295–308.

Földi, A., Mészáros, M., Sági, L., Deme, S., Dombovári, P., Szántó, A., Tóth, K., and *Petőfi-Tóth, K.,* 2010: Légköri terjedésszámító szoftverek összehasonlítása. *Sugárvédelem 3(1),* 33–41. (In Hungarian)

Goricsán, I., Balczó, M., Régert, T., and *Suda, J.M.,* 2004: Comparison of Wind Tunnel Measurement and Numerical Simulation of Dispersion of Pollutants in Urban Environment. In Impact of Wind and Storm on City Life and Built Environment. *COST C14 International Conference on Urban Wind Engineering and Buildings Aerodynamics,* D.6.1-D.6.10.

Holmes, N.S. and *Morawska, L.,* 2006: A review of dispersion modelling and its application to the dispersion of particles: An overview of different dispersion models available. *Atmos. Environ. 40,* 5902–5928.

Huh, C-A., Hsu, S-C., and *Lin, C-Y.,* 2012: Fukushima-derived fission nuclides monitored around Taiwan: Free tropospheric versus boundary layer transport. *Earth Planet. Sci. Lett. 319–320,* 9–14.

Kocsis, Zs., Ferenczi, Z., Havasi, Á., and *Faragó, I.,* 2009: Operator splitting in the Lagrangian air pollution transport model FLEXPART. *Időjárás 113,* 189–202.

Koracin, D., Vellore, R., Lowenthal, D.H., Watson, J.G., Koracin, J., McCord, T., DuBois, D.W., Chen, L-W.A., Kumar, N., Knipping, E.M., Wheeler, N.J.M., Craig, K., and *Reid, S.,* 2011: Regional Source Identification Using Lagrangian Stochastic Particle Dispersion and HYSPLIT Backward-Trajectory Models. *J. Air Waste Manage. Assoc. 61,* 660–672.

Lagzi, I., Tomlin, S.A., Turányi, T., and *Haszpra, L.,* 2009: Modelling photochemical air pollutant formation in Hungary using an adaptive grid technique. *Int. J. Environ. Poll. 36,* 44–58.

Leelőssy, Á., Mészáros, R., and *Lagzi, I.,* 2011: Short and long term dispersion patterns of radionuclides in the atmosphere around the Fukushima Nuclear Power Plant. *J. Environ. Radioactiv. 102,* 1117–1121.

Long, N.Q., Truong, Y., Hien, P.D., Binh, N.T., Sieu, L.N., Giap, T.V., and *Phan, N.T.,* 2012: Atmospheric radionuclides from the Fukushima Dai-ichi nuclear reactor accident observed in Vietnam. *J. Environ. Radioactiv. 111,* 53–58.

McGowan, H. and *Clark, A.,* 2008: Identification of dust transport pathways from Lake Eyre, Australia using HYSPLIT. *Atmos. Environ. 42,* 6915–6925.

Mészáros, R., Vincze, Cs., and *Lagzi, I.,* 2010: Simulation of accidental release using a coupled transport (TREX) and numerical weather prediction (ALADIN) model. *Időjárás, 114,* 101–120.

Moreira, V.S., Degrazia, G.A., Roberti, D.R., Timm, A.U., and *Carvalho, J.C.,* 2011: Employing a Lagrangian stochastic dispersion model and classical diffusion experiments to evaluate two turbulence parametrization schemes. *Atmos. Poll. Res. 2,* 384–393.

Righi, S., Lucialli, P., and *Pollini, E.,* 2009: Statistical and diagnostic evaluation of the ADMS-Urban model compared with an urban air quality monitoring network. *Atmos. Environ. 43,* 3850–3857.

Shan, W., Yin, Y., Lu, H., and *Liang, S.,* 2009: A meteorological analysis of ozone episodes using HYSPLIT model and surface data. *Atmos. Res. 93,* 767–776.

Silverman, K.C., Tell, J.G., Sargent, E.V., and *Qiu, Z.,* 2007: Comparison of the Industrial Source Complex and AERMOD Dispersion Models: Case Study for Human Health Risk Assessment. *J. Air Waste Manag. Assoc. 57,* 1439–1446.

Simpson, D., Benedictow, A., Berge, H., Bergström, R., Emberson, L.D., Fagerli, H., Hayman, G.D., Gauss,M., Jonson, J.E., Jenkin, M.E., Nyíri, A., Richter, C., Semeena, V.S., Tsyro, S., Tuovinen, J.-P., Valdebenito, Á., and *Wind, P.,* 2012: The EMEP MSC-W chemical transport model – Part 1: Model description. *Atmos. Chem. Phys. Discuss. 12,* 3781–3874.

Srinivas, C.V., Venkatesan, R., Baskaran, R., Rajagopal, V., and *Venkatraman, B.,* 2012: Regional scale atmospheric dispersion simulation of accidental releases of radionuclides from Fukushima Dai-ichi reactor. *Atmos. Environ. 61,* 66–84.

Steib, R. and *Labancz, K.,* 2005: Regulatory modeling in Hungary – the AERMOD model. PART I. Description and application. *Időjárás 109,* 157–172.

Stohl, A., Forster, C., Frank, A., Seibert, P., and *Wotawa, G.,* 2005: Technical note: The Lagrangian particle dispersion model FLEXPART version 6.2. *Atmos. Chem. Phys. 5,* 4739–4799.

Stohl, A., Seibert, P., Wotawa, G., Arnold, D., Burkhart, J.F., Eckhardt, S., Tapia, C., Vargas, A., and *Yasunari, T.J.,* 2011: Xenon-133 and caesium-137 releases into the atmosphere from the Fukushima Dai-ichi nuclear power plant: determination of source term, atmospheric dispersion, and deposition. *Atmos. Chemis. Phys. 11,* 28319–28394.

Yamada, T., 2004: Merging CFD and atmospheric modeling capabilities to simulate airflows and dispersion in urban areas. *Comput. Fluid Dynam. J. 13(2), 47,* 329–341.

Vardoulakis, S., Fisher, B.E.A., Pericleous, K., and *Gonzalez-Flesca, N.,* 2003: Modelling air quality in street canyons: a review. *Atmos. Environ. 37,* 155–182.

IDŐJÁRÁS

VOLUME 117 * 2013

BUDAPEST, HUNGARY

AUTHOR INDEX

TABLE OF CONTENTS

I. Papers

SUBJECT INDEX

B

C

D

E

F

G

W

Y

INSTRUCTIONS TO AUTHORS OF *IDŐJÁRÁS*

The purpose of the journal is to publish papers in any field of meteorology and atmosphere related scientific areas. These may be

- research papers on new results of scientific investigations,
- critical review articles summarizing the current state of art of a certain topic,
- short contributions dealing with a particular question.

Some issues contain "News" and "Book review", therefore, such contributions are also welcome. The papers must be in American English and should be checked by a native speaker if necessary.

Authors are requested to send their manuscripts to

Editor-in Chief of IDŐJÁRÁS
P.O. Box 38, H-1525 Budapest, Hungary
E-mail: journal.idojaras@met.hu

including all illustrations. MS Word format is preferred in electronic submission. Papers will then be reviewed normally by two independent referees, who remain unidentified for the author(s). The Editor-in-Chief will inform the author(s) whether or not the paper is acceptable for publication, and what modifications, if any, are necessary.

Please, follow the order given below when typing manuscripts.

Title page: should consist of the title, the name(s) of the author(s), their affiliation(s) including full postal and e-mail address(es). In case of more than one author, the corresponding author must be identified.

Abstract: should contain the purpose, the applied data and methods as well as the basic conclusion(s) of the paper.

Key-words: must be included (from 5 to 10) to help to classify the topic.

Text: has to be typed in single spacing on an A4 size paper using 14 pt Times New Roman font if possible. Use of S.I. units are expected, and the use of negative exponent is preferred to fractional sign. Mathematical formulae are expected to be as simple as possible and numbered in parentheses at the right margin.

All publications cited in the text should be presented in the *list of references*, arranged in alphabetical order. For an article: name(s) of author(s) in Italics, year, title of article, name of journal, volume, number (the latter two in Italics) and pages. E.g., *Nathan, K.K.,* 1986: A note on the relationship between photo-synthetically active radiation and cloud amount. *Időjárás 90,* 10-13. For a book: name(s) of author(s), year, title of the book (all in Italics except the year), publisher and place of publication. E.g., *Junge, C.E.,* 1963: *Air Chemistry and Radioactivity.* Academic Press, New York and London. Reference in the text should contain the name(s) of the author(s) in Italics and year of publication. E.g., in the case of one author: *Miller* (1989); in the case of two authors: *Gamov* and *Cleveland* (1973); and if there are more than two authors: *Smith et al.* (1990). If the name of the author cannot be fitted into the text: *(Miller,* 1989); etc. When referring papers published in the same year by the same author, letters a, b, c, etc. should follow the year of publication.

Tables should be marked by Arabic numbers and printed in separate sheets with their numbers and legends given below them. Avoid too lengthy or complicated tables, or tables duplicating results given in other form in the manuscript (e.g., graphs).

Figures should also be marked with Arabic numbers and printed in black and white or color (under special arrangement) in separate sheets with their numbers and captions given below them. JPG, TIF, GIF, BMP or PNG formats should be used for electronic artwork submission.

Reprints: authors receive 30 reprints free of charge. Additional reprints may be ordered at the authors' expense when sending back the proofs to the Editorial Office.

More information for authors is available: journal.idojaras@met.hu

Published by the Hungarian Meteorological Service

Budapest, Hungary

INDEX 26 361

HU ISSN 0324-6329